The Pennsylvania State University

The Graduate School

EXPERIMENTAL INVESTIGATION OF DYNAMIC ROUGHNESS AS AN AERODYNAMIC FLOW CONTROL METHOD

A Thesis in

Aerospace Engineering

by

Tenzin Choephel

Submitted in Partial Fulfillment

of the Requirements

for the Degree of

Master of Science

December 2010

The thesis of Tenzin Choephel was reviewed and approved* by the following:

Jose Palacios
Post Doctoral Research Associate
Special Signatory

Edward C. Smith
Professor of Aerospace Engineering
Thesis Advisor

Mark D. Maughmer
Professor of Aerospace Engineering

George A. Lesieutre
Professor of Aerospace Engineering
Head of the Department of Aerospace Engineering

*Signatures are on file in the Graduate School

ABSTRACT

An experimental investigation was undertaken to determine the ability of dynamic roughness in preventing flow separation and hence delaying stall in airfoils. Dynamic roughness involves small periodic perturbations to the airfoil surface in the form of discrete bumps along the span of the airfoil that have the ability to expand and contract at a specific frequency.

As part of this work, a mechanism for measuring the aerodynamic loads on airfoils was designed and validated for the low-speed wind tunnel at the Pennsylvania State University.

A reciprocating mechanism for dynamic roughness actuation involving mechanical springs was proposed. Kinematic and dynamic analyses of the mechanism meeting the frequency requirement at higher Reynolds numbers were performed. It was observed that the mechanism would not function properly at the required frequencies. A rotating cam was proposed and designed as an alternative actuator mechanism to support fundamental research.

Application of dynamic roughness at ~74% chord, which corresponds to the separation point at stall, on a NACA 23012 airfoil failed to cause flow control. Part of the reason for this ineffectiveness was attributed to the stall characteristic specific to the NACA 23012.

Later, the HTR1555 airfoil was chosen as an ideal airfoil for testing of dynamic roughness flow control due to its stalling behavior. Dynamic roughness with amplitude

on the order of the local boundary layer thickness was applied at 55% chord from the leading edge. Three different cam shapes were tested. Tests at R_C= 1,000,000 showed that the best cam shape resulted in maximum lift increment of 3.5%, without any delay in stall angle. Dynamic roughness cams with half this amplitude provided a lower increase in maximum lift. Tests with the same cam shape and amplitude at R_C= 250,000 resulted in 4.5% increase in maximum lift.

Replication of the experiments on SM701 airfoil by the original investigator on which this work was largely based revealed that the reported effect on the behavior of the tufts due to the actuation of dynamic roughness was not due to the flow control caused by the physical dynamic roughness interacting with the boundary layer. Careful observations from the tests performed on the same airfoil and actuator used by the researcher who reported the original results pointed to acoustic excitation and/or vibration as the most probable cause of the observed flow attachment.

Static vortex generators installed at 10% and 55% chord from the leading edge increased maximum lift by 35% and 14% respectively, much higher gains compared to dynamic roughness with comparable device heights. Deployable vortex generators are proposed. Deployable vortex generators can, for example, be deployed 1/rev on helicopter rotor to prevent retreating blade stall and hence improve forward flight performance.

TABLE OF CONTENTS

LIST OF FIGURES

LIST OF TABLES

LIST OF SYMBOLS

α Angle of attack with respect to the chord of the airfoil

α_o Angle of attack at zero lift

U_∞ Free stream velocity

c_l Lift coefficient of the airfoil

c_d Drag coefficient the airfoil

c_m Pitching moment coefficient about the quarter chord point on the airfoil

c_μ Steady momentum coefficient

$\langle c_\mu \rangle$ Oscillatory momentum coefficient

F^+ Non-dimensional frequency of actuation

C_μ Total momentum coefficient, including steady and oscillatory

$c_{l,max}$ Maximum lift coefficient of the airfoil

α_{max} Angle of attack at the maximum lift coefficient

$c_{l,o}$ Lift coefficient at zero geometric angle of attack

f_e Actual frequency of excitation

X_{te} Distance from the location of the actuator to the trailing edge of the airfoil

ρ Density of air

μ Dynamic viscosity of air

C_p Pressure coefficient

ACKNOWLEDGEMENTS

First of all, I would like to thank my advisor Dr. Edward C. Smith for his guidance and assistance during the course of this research. His remarkable sense of understanding and friendliness are how he is personally known to his students.

I would also like to thank Dr. Jose Palacios for all of his help during the course of this work. His mentorship, resourcefulness and limitless energy have taught me much and left a lasting impression on me.

Sincere thanks also go to Dr. Mark D. Maughmer for his thoughtful technical advice and many hours of assistance during the wind tunnel testing. Amandeep and Bernado are also deeply thanked for their help with the wind tunnel instrumentation at the Penn State Low-Speed, Low-Turbulence wind tunnel.

Many thanks also go to Rick Auhl, who was always willing to assist me through insightful comments and assistance with the experimental facilities.

Bryan at the engineering service at Penn State is acknowledged for the fabrication of the components and airfoil models for this work.

Above all, I thank my mother, Dorjee Bhuti and my late loving father Pema Dorjee, for all of their love and support. My academic success would not have been possible without their support and the support of my brother, Ngawang Norbu and sister, Ngodup Wangmo.

Chapter 1

INTRODUCTION

1.1 Literature Review

1.1.1 The Problem of Flow Separation

Fluid particles in a boundary layer are slowed down by friction at the wall. If the external potential flow is sufficiently retarded, for instance due to the presence of an adverse pressure gradient, the momentum of the fluid will be dissipated by both the wall shear and the pressure gradient. At some point the viscous layer breaks away from the boundary. The surface streamline at the wall leaves the body at this point and the boundary layer is said to separate [1]. At separation, the rotational flow region near the wall thickens, the normal velocity component increases and the boundary layer equations, which are derived based on attached flow, are rendered invalid.

Flow separation is ubiquitous in many engineering systems. The attached flow on an airplane wing leaves the surface at some point at increased angles of attack. The flow over a truck or a car separates off its back, leaving a region of re-circulating air behind it. The fluid that is attached over the front part of a submarine or a torpedo separates off the rear. The boundary layer on the blades of turbo-machinery separates if not operated at

design conditions. The flow in the diverging part of a nozzle may separate from the wall due to the adverse pressure gradient.

Flow separation on these engineering systems is almost always associated with losses of some kind, including loss of lift, increase in drag, loss in pressure recovery etc. These losses translate into performance degradation and loss of efficiency of the system such as increase in power, and hence fuel, consumption in fixed wing as well as rotary wing aircraft, automobiles, submarines etc. As a result, engineers have been concerned, for a long time, with minimizing the adverse effects of separation. In fact, the aerodynamic or hydrodynamic vehicles or devices that are taken for granted today are results of tremendous advances made in the development of ways to avoid or modify separation characteristics.

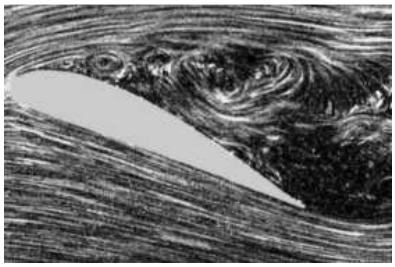

Airfoil flow separation

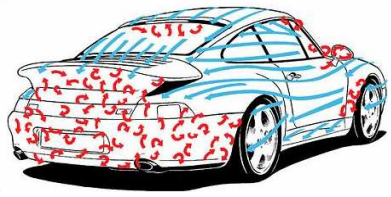

Separated flow over a typical car geometry

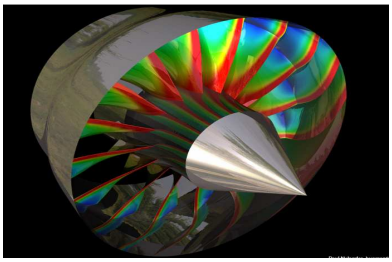

Flow separation in turbo-machinery

Flow around submarine

Figure 1-1 Examples of flow separation in different engineering systems

The mechanism that leads to steady, two-dimensional flow separation is well-established and was first explained by Ludwig Prandtl in 1904. He provided a criterion of separation for a steady, two-dimensional boundary layer developing over a wall. When the flow is retarded, the near wall fluid may not have sufficient momentum to continue the motion and will be brought to a stand still at a point, called separation point. After this point, the fluid moves in a direction opposite to the direction of the external stream, the original boundary layer now flowing over a re-circulating zone of fluid. Since the velocity of fluid at the wall is zero, due to no slip condition, the velocity gradient at the wall, $\left(\partial u / \partial y\right)_0$ before separation must be positive. At the point of separation it is zero. After separation, the velocity gradient at the wall wil be negative. The velocity profile must have positive curvature at the wall at separation. But, since the curvature $\left(\partial^2 u / \partial y^2\right)_0$ is negative at large distance from the wall, the separated profile must have a point of inflection between the wall and the edge of the boundary layer. Hence, positive curvature of the velocity profile at the wall i.e. $\left(\partial^2 u / \partial y^2\right)_0 > 0$ is a necessary condition for a steady, two-dimensional boundary layer to be separated. Conversely, negative curvature of the velocity profile at the wall is a sufficient condition for a boundary layer to be attached [2].

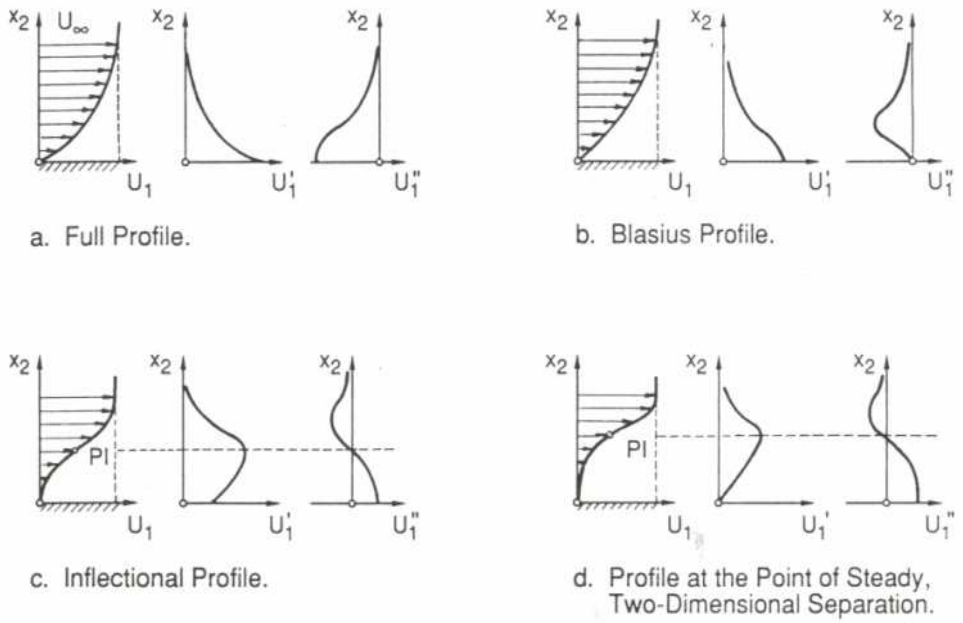

Figure 1-2 Velocity profile in a boundary layer [2]

1.1.2 Control of Separation: Traditional Perspective

By traditional, it is meant that any analysis or technique of control that is based on the assumption of steady flow, incompressible boundary layer approximations is employed. The arguments in the previous section led to several possible methods of boundary layer separation control. The idea is to keep the curvature term $\left(\partial^2 u / \partial y^2\right)_0$ in the boundary layer equation as negative as possible, for this is a sufficient condition for a steady boundary layer to remain attached. This is equivalent to making the velocity profile as full as possible at the wall, which makes sense from the physical point of view.

When the boundary-layer equations for a fixed wall are rearranged into Eqn. 1 where the curvature term is isolated on the right hand side of the equation, the idea is to physically manipulate the terms on the left hand side, which include y-component of velocity, stream-wise pressure gradient, gradient of viscosity with temperature and temperature gradient normal to the wall. The separation control methods include use of wall suction, favorable pressure gradient, surface cooling in gases or surface heating in liquids. These are explained briefly in the next few paragraphs.

$$\left[\rho\frac{\partial u}{\partial t}\right]_o+\left[\rho u\frac{\partial u}{\partial x}\right]_o+\left[\rho v\frac{\partial u}{\partial y}\right]_o+\frac{dP}{dx}-\frac{d\mu}{dT}\left[\frac{\partial T}{\partial y}\frac{\partial u}{\partial y}\right]_o=\left[\mu\frac{\partial^2 u}{\partial y^2}\right]_o \qquad \textbf{Eqn. 1}$$

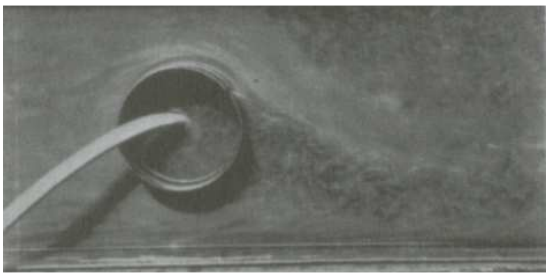

Figure 1-3 Prandtl's photograph of the use of suction to attach the flow around a cylinder [Betz, 1961]

Adverse pressure gradient past the minimum pressure point of the body along with the skin friction depletes the momentum of the near wall boundary layer fluid. Separation is delayed if the near wall fluid is removed through slots or porous surfaces. Prandtl [3] used suction through a slit on one side of a circular cylinder to remove the decelerated fluid particles in the near wall region. By doing so, the velocity gradient at the wall is increased, the curvature of the profile at the wall becomes more negative and

separation is avoided. Flow visualization photographs from his experiments, shown in Figure 1-3, show convincingly that the boundary layer sticks to the suction side of the cylinder over a considerably greater portion of the surface. Similar boundary layer suction technique was also applied to the diverging part of a nozzle as seen in Figure 1-4.

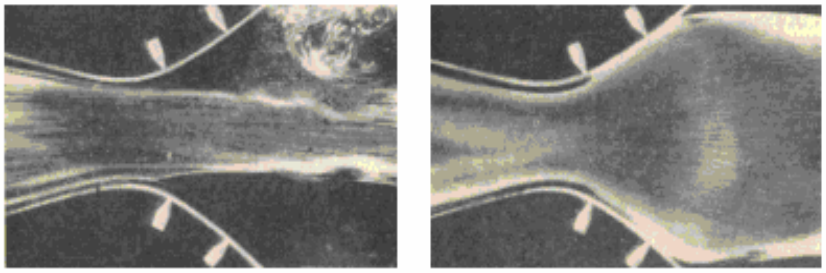

Figure 1-4 a) Use of suction to attach the flow around a cylinder [Betz, 1961], b) Flow with suction on the walls of a highly diverging section of a nozzle [3]

The first experiments using boundary-layer suction on a full scale airplane was conducted at the Aerodynamic Research Institute of Gottingen, Germany [4]. The effect of suction on boundary layer reattachment over the flap is clearly seen in Figure 1-5 and demonstrates the ability of suction to control the flow in actual flight conditions.

Boundary-layer blowing has also been employed to delay separation. Blowing energizes the near wall fluid, which has been depleted of momentum due to shear stress and adverse pressure gradient. Following World War II, the need for high-speed aircraft necessitated wings with higher wing loading, thinner profiles, and smaller platform areas. But, small wings required higher approach and landing speeds to avoid stall, which are not desirable. Steady-blowing technique for lift enhancement at low flight speeds was used as a solution to the small wing problem. The internally blown flap, for example, was

developed over the period from mid-1950s to the mid-1960s.The Blackburn B-103 Buccaneer used full wing and tail boundary layer control [5]. The Lockheed F-104 Starfighter and BAC TSR-2 used blown flaps to reduce landing speeds and take-off distances. A layout of an internal plumbing system used on Grumman F9F-4 is shown in Figure 1-6.

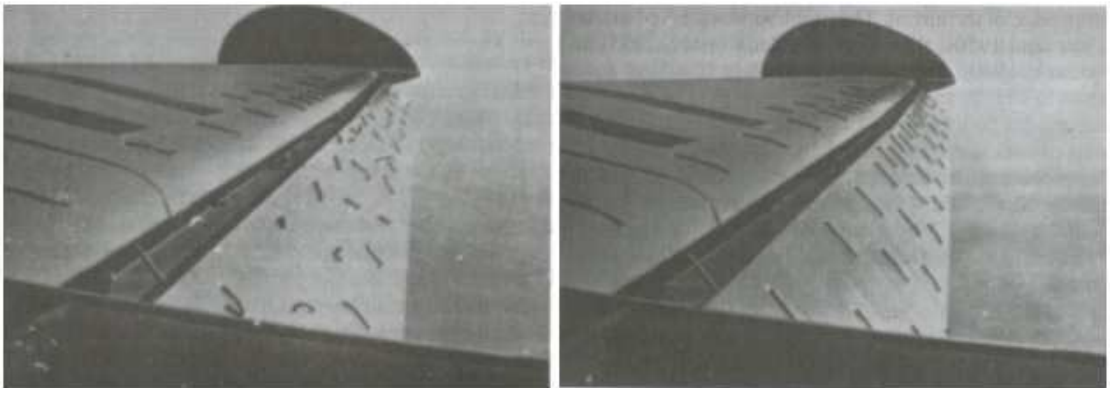

Figure 1-5 Separated flow over a flap, shown by the tufts in a flight test, being reattached by suction applied at the shoulder of the flap [17]

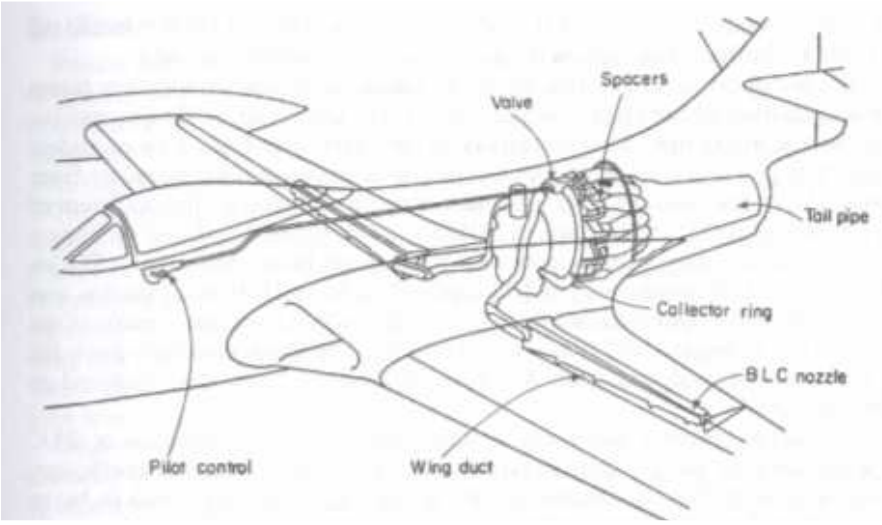

Figure 1-6 Plumbing system to control the blown flap on Grumman F9F-4 [Attinello, 1961]

The second method to control separation that follows from the Eqn.1 is to manipulate the pressure gradient over the body. Streamlining is an old art and an effective method to reduce the steepness of pressure gradient over the pressure recovery region. A clear physical idea of the usefulness of streamlining is obtained if the flows over a cylinder and an airfoil with the same maximum thickness as the cylinder are compared as in Figure 1-7. The separated region or re-circulating wake is larger in the case of the cylinder than that on the airfoil. This translates to comparatively higher pressure drag on the cylinder.

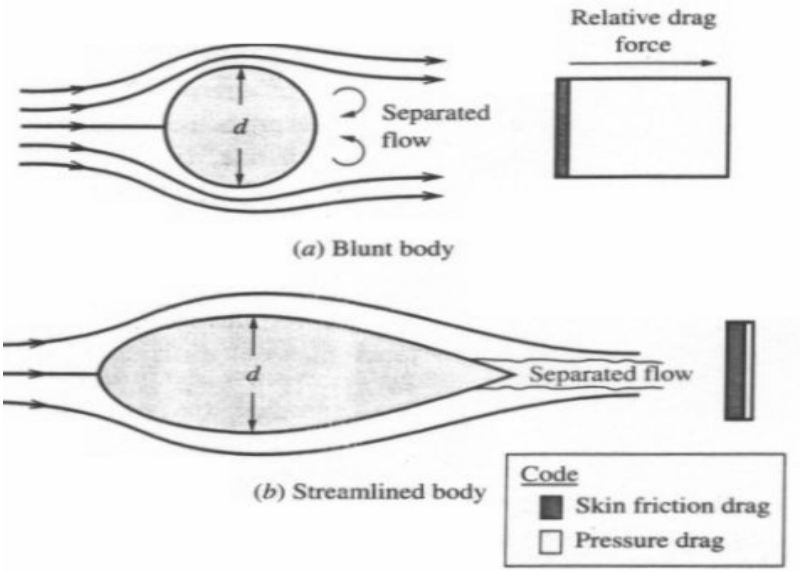

Figure 1-7 Comparison of separated flow between a cylinder and an airfoil of same frontal areas [www.aerospaceweb.org]

Yet another method to delay separation that follows from the equation is by heat transfer. By transferring heat from the wall to the fluid in liquids or from the fluid to the

wall in gases, this term adds a negative contribution to the curvature of the velocity profile at the wall and, hence, causes the separation to move farther downstream.

1.1.3 Passive versus Active Flow Control

By definition, flow separation control techniques that do not require constant input of energy are called passive control. Common passive techniques for separation control are aerodynamic shaping and static vortex generators.

Figure 1-8 Row of vortex generators on the wing of Cardinal II C-177B [www.axoplasmic.com]

Streamlining and special contouring of airfoils can be considered as a passive technique. Liebeck [6] designed many airfoils that produce high lift coefficients using a Stratford pressure recovery such that the turbulent boundary layer would remain attached with the maximum possible adverse pressure gradient. The contour also included a transition ramp in the pressure distribution, first employed by F. X. Wortmann, that

would cause the laminar boundary layer to transition into turbulent boundary layer before reaching the Stratford recovery. The airfoil shape was created with boundary layer behavior in mind.

Vortex generators act by enhancing mixing or entrainment in the boundary layer by causing the higher momentum air from the outer edge of the boundary layer to be drawn to the wall, decreasing the susceptibility to separation. A row of vortex generators on the wing of a Cardinal II C-177B is shown in Figure 1-8. There is a drag penalty associated with vortex generators, since they introduce resistance to the flow during cruise conditions, even if the flow is attached.

Active control implies techniques that involve input of energy to activate the actuator that controls the flow. Boundary layer blowing, suction and heat transfer discussed above are active methods. The main advantage of active control over passive control is that the actuation can be turned off when it is not needed, and it may be adaptable to changing flight conditions. Active separation control techniques may result in less drag penalty in comparison to passive methods, but they are usually more complicated to implement because of the simple reason that an actuator is required.

1.1.4 Modern Flow Control: Exploiting Flow Instabilities

The methods of separation control discussed so far are based on the assumption of steady flow analysis. These techniques deal with modifying only the mean flow characteristics. It is well accepted that steady two-dimensional flow separation is well

understood, with a satisfactory analytical foundation [7]. However, experimental data reveals that separation is steady only in time-averaged sense. The rich time dependent coherence in the boundary layers, discovered around the middle of the twentieth century, had not been taken advantage of in controlling separation.

A major development in boundary-layer theory after Prandtl's groundbreaking discovery was in shear flow instability, with the objective of investigating the origin of turbulence. The foundations of the stability analysis of viscous shear layers were laid with Teitjen's dissertation [8] and Tollmein's paper [9] on the stability analysis of laminar boundary layers. Tollmien's linear stability analyses predicted the growth and decay of disturbances in a Blasius boundary layer.

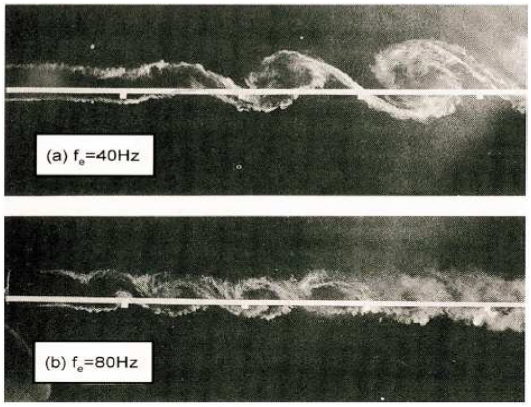

Figure 1-9 Flow visualization of a two-dimensional mixing layer excited at two frequencies, showing large span wise vortical structures responsible for large scale momentum transfer. Ratio of upper to lower stream velocity: U_1/U_2=0.4[Oster,D, Wygnansky, I.J, Dziomba, B].

Tollmien's theory was validated in 1948 by Schubauer and Skramstad [10] at the National Bureau of Standards. They introduced unsteady perturbations in the laminar boundary layer to trigger what are known as Tollmien-Schlicting (TS) waves. This

ground breaking technique was not only used for studying stability of flows, but it also came to be considered as a tool for controlling laminar separation and transition [11]. Periodic excitation of the laminar boundary layer triggers premature transition to turbulence and since turbulent boundary layer is less susceptible to separation, flow separation could be delayed by triggering transition.

Although laminar-turbulent transition could be caused by periodic excitation of the boundary layer, the manipulation of the turbulent shear flows was considered to be not possible due to the belief that turbulence is inherently a random process. The idea that un-steady actuation might be effective also for the control of fully turbulent flows came with the discovery of coherent structures in turbulent boundary layers by Kim et al. [12] and in turbulent jets by Crow and Champagne [12]. Investigations by Brown and Roshko [13] and Winant and Browand [14] in the mixing layer demonstrated the existence of large coherent structures (LCSs), which were found to be the primary agents for momentum transport across the flow domain. It was also found that periodic mechanical excitation at the flow origin effectively enhanced the control of mixing across the shear layer [15]. Excitation was observed to accelerate and regulate the generation of these large coherent structures, especially when the mean flow is unstable, and transfer momentum across the mixing layer. Observe, for example, the smoke flow visualization patterns in a mixing layer that is excited at two different frequencies in Figure 1-9. These experiments demonstrated that very low levels of actuation energy are sufficient to control the instability and hence the large scale features of a shear flow. The control of turbulent shear flows by exploiting the instabilities within the turbulent flow was

demonstrated. By mid 1980s, the basic strategies of flow control changed from controlling the steady, time-averaged state to controlling the flow instabilities.

Since the research work that is reported in this thesis is related to airfoils, only those past work conducted by various investigators that deal with airfoil applications will be discussed here. Historical backgrounds that set the ball rolling for flow control research, governing parameters in flow control by excitation, airfoil performance enhancement by delaying or preventing flow separation using different actuators, drag reductions, and attempts to apply them to flight vehicles are described in the following paragraphs.

1.1.4.1 Acoustic Excitation: Setting the Stage for Flow Control Research

Much of the early research in flow control on airfoil used acoustic waves as the actuator. Sound at certain frequencies was found to promote boundary layer transition. In 1961, Chang [16] demonstrated that the use of acoustic excitation resulted in a drag reduction of about 20 % on a low Reynolds number, R_C=80,000, airfoil. Collins and Zelenevitz [16] used an external acoustic source to reattach the separated flow on an airfoil at high angles of attack. The technique involves introducing sound into a wind tunnel from the walls of the test section [17] by the use of speakers or acoustic drivers. Zamam et al [17] explained that the excitation was effective when acoustic standing waves in the tunnel induced a transverse velocity component close to the surface of the airfoil. Huang et al [16] and Hsiao [16] found that internal acoustic actuators acting

through the slots on the airfoil surfaces could be effective actuators. Williams et al [16] showed that it was not the acoustic waves alone that caused the control but that the unsteady momentum addition to the flow through the mass-displacement effect of the actuator was the primary physical mechanism for the effect. A summary of representative research on acoustic excitation is presented in Table 1.

Investigator (s)	Airfoil	Re ($\times 10^6$)	Optimum St range	Disturbance or input level	α range (deg)	Max. ΔC_L (%)
Collins and Zelenevitz [20]	NACA 2412	0.53	24–90	100–134 dB on airfoil	20, 24	56
Ahuja et al. [71]	GA(W)-1	0.6	4	156 dB on wall	~ 18	40
Ahuja and Burrin [72]	NACA 65_1-213	0.25	2.7	147 on airfoil	16	50
Marchmann et al. [73]	Wortmann	0.2	27	—	15	—
Zaman et al. [70]	LRN(1)-1007	0.04–0.14	1–5 4–25	104 dB on wall	$\leqslant 8$ $\geqslant 18$	50
Nishioka et al. [74]	Flat Plate	0.04	3.8–27	Below airfoil	8–14	—
Zaman [75]	LRN(1)-1007	0.075	2–5	$u'/U_\infty \leqslant 3\%$ near LE	18	50

Table 1: Summary of representative research on airfoils using acoustic excitation [17]

Observe from Table 1 that the increase in lift coefficient at a given angle of attack is as much as 56 % in these experiments. This does not mean that the $C_{l,max}$ has been increased by that amount. Also note that the investigations were performed at relatively high angle of attack, where the wing may be already stalled. Moreover, these investigations were performed at low Reynolds number.

There are, however, drawbacks to acoustic excitation as a tool for flow control. For one thing, excitation was found to be facility dependent in the investigations of Ahuja et al. [18] and Zaman et al. [19] etc. The acoustic drivers used by them excited the wind tunnel's resonant modes, which in turn excited the separating shear layers. This raises serious doubts concerning its application to aircraft. No wonder, there were significant

lift increase at some incidences, while decreases at others. Moreover, high levels of excitation were required to obtain significant lift enhancement, calling into question the practical application. Also, a problem arises when comparing different investigations as there is no uniform measurement location, with sound levels being measured at the wall or on the surface of the airfoil. Above all, these investigations were performed at low Reynolds number, i.e. $R_C \leq 600{,}000$. The effect on separation is likely coupled with actuation effect on transition.

As far as acoustic excitation is concerned, a large range of effective reduced frequencies, $St = f_p c / U_\infty$, was observed to exist. It can span over two orders of magnitude, from O(1) [20] to O(100) [21]. However, Zaman [22] showed that optimum Strouhal number can be orders of magnitude lower than that corresponding to the linear inviscid stability of the shear layer when excitation amplitude is increased. Ahuja et al. [18] observed that with large disturbance levels of ~156dB, the effective Strouhal number was St ≈4. In a nutshell, acoustic excitation is effective for separation control at low frequencies when excitation amplitudes are high. Acoustic excitation set the stage for a host of subsequent demonstrations of flow separation control on airfoil by using hydrodynamic excitation.

The nature of the actuation method was found to be not important as long as there is an oscillatory addition of momentum into the boundary layer. Different researchers have come up with different methods of actuation, each with their own advantages and disadvantages. In the following few paragraphs, a number of different techniques of actuation that has been used to date will be discussed. Wherever necessary, sufficient

details will be furnished. However, before these specific techniques are discussed, it may be worthwhile to look at the fundamental mechanism of separation control and identify some basic governing parameters, considering a deflected flat plate as the model for discussion. Topics discussed in the next section include the definition of reduced frequency, momentum coefficient, optimum reduced frequency, and location of excitation.

1.1.4.2 Governing Parameters

Wygnansky et al [17] used oscillatory blowing imposed on the flow over a deflected flat plate as the model for identifying the basic governing parameters for the control of flow separation. The choice of flat plate for this purpose is motivated by the following two reasons.

Firstly, the authors contend that the deflected flat plate is a well-known high lift device and it makes practical sense to use that as a simple model with which to start.

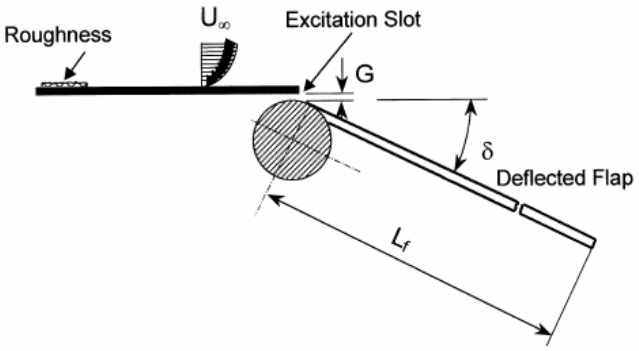

Figure 1-10 Generic flap configuration [23]

Secondly, since the general problem of flow separation is complex, with many independent variables coming into the play, and with no established theoretical model available to date, the choice of flat plate eliminates the effects of curvature, upstream condition and moving separation location, such as observed on airfoils. With the simplicity of geometry of the problem being investigated, one can isolate the important governing parameters.

The authors considered a generic flap configuration [24] shown in Figure 1-10. The upstream boundary layer is fully turbulent and disturbances are imposed either by a two dimensional jet or by a fliperon.

Since the actuation involves unsteady periodic motion, frequency is naturally one of the leading parameters that govern the effectiveness of the actuator to change the flow characteristics. Just like lift and drag coefficients, a non-dimensional measure of the actual frequency of actuation is needed to compare between the various experiments conducted on different sizes of the model being studied and in different places. This led to the definition of what is known as F^+, defined as:

$$F^+ = \frac{f_e X_{te}}{U_\infty} \qquad \textbf{Eqn. 2}$$

On the generic flap model, X_{te} is the distance between the excitation location and the flap trailing edge. On most of the airfoil studies carried out till date, $X_{te,}$ has been taken to be the distance between the actuation location and the trailing edge. The work discussed in this thesis also follows this tradition. In some literature, instead of $X_{te,}$, length or height of separation bubble is used to define F^+. Further investigation is definitely

needed to standardize this definition. Another important parameter that needs to be understood before moving ahead in the current discussion is momentum coefficient.

For a two dimensional configuration the total, including the mean and the oscillatory, momentum coefficient is defined as a ratio of the momentum added by the actuator and the momentum in the free stream:

$$C_\mu = \frac{\rho_j U_j{}^2 G}{1/2 \rho_\infty U_\infty{}^2 L} \qquad \textbf{Eqn. 3}$$

where the subscript j refers to a two dimensional jet, G is either the slot width h or step height g, and L is usually taken to be the length of the body under consideration, e.g. chord c, or in the present example, flap length L_f. In case of oscillatory momentum super imposed on steady momentum addition, $U_j = \overline{U_j} + u_j$, which includes both the mean and the oscillatory components of velocity. Substituting this into Eqn. 3 and time averaging gives:

$$\overline{C_\mu} = \frac{2G}{L}\left(\frac{\overline{U_j}}{U_\infty}\right)^2 + \frac{2G}{L}\overline{\left(\frac{\overline{u_j}}{U_\infty}\right)^2} \qquad \textbf{Eqn. 4}$$

where the first term is steady blowing contribution and the second term is the contribution of the super-imposed oscillatory blowing. This may be conveniently denoted by $C_\mu = (c_\mu, \langle c_\mu \rangle)$ [17].

When excitation is achieved my pure mechanical means, Wygnansky et al. [17] defines the oscillatory momentum coefficient as:

$$\langle c_\mu \rangle = \frac{1}{1/2\rho_\infty U_\infty^{\,2} L} \int_0^\infty u^2 dy \qquad \textbf{Eqn. 5}$$

where u is the fluctuating component of velocity next to, and downstream of, the actuator. Oscillatory blowing and mechanical actuation via a fliperon are different in their designs and mechanism, but their effect on the flow at a given frequency is observed to be virtually identical. Nishri [23] compared the delay in flow separation angle between an oscillatory blowing and suction device using speaker and a mechanical fliperon shown in Figure 1-11.

Figure 1-11 Oscillatory blowing/suction device and fliperon [17]

Results for excitation for two different momentum coefficients, viz. $\langle c_\mu \rangle = 0.02\%$ and $\langle c_\mu \rangle = 0.01\%$, at R_C=450,000 and G/L_f=0.5% are shown in Figure 1-12. Observation of the trends in separation delay angles at varying frequency shows that the definition of momentum coefficient in Eqn. 1.4 is valid in quantifying momentum addition in different actuation methods.

Having introduced the definition of non-dimensional frequency and momentum coefficient, the next crucial point is that of the identification of optimum frequency for the control of separation. Again Wygnansky et al [24] investigated the flow over a deflected flap using oscillatory blowing at the flap shoulder of Figure 1-10. The

introduction of two-dimensional oscillatory blowing enhanced entrainment and reattached the initially detached shear layer to the flap surface. Minimum momentum coefficient required to attach the flow on the flap as a function of imposed reduced frequency is shown in Figure 1-13. It can be observed that the optimum reduced frequency of excitation is centered somewhere around $F^{+}\approx 1$. Moreover, this is independent of Reynolds number. Therefore, optimum reduced frequency is defined to be that frequency for which minimum amount of momentum addition is required to achieve the same result, which in the current example is the attachment of the flow that is initially separated from the flap shoulder.

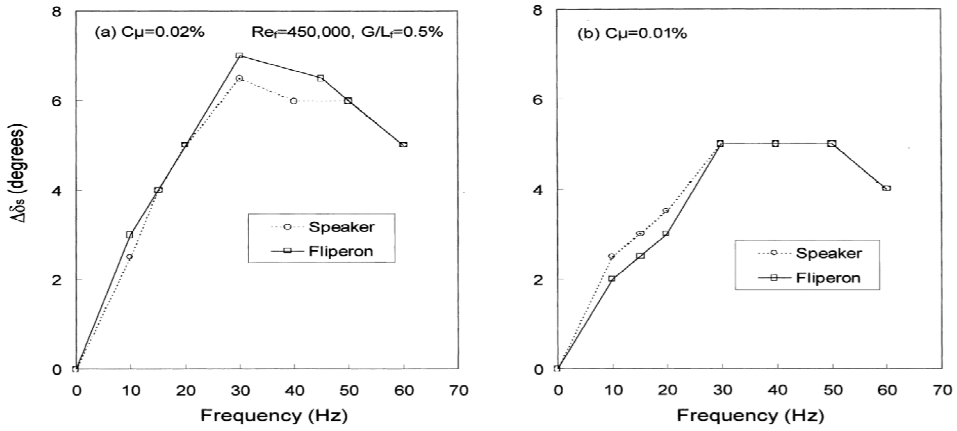

Figure 1-12 Comparison of two different methods of excitation (oscillatory blowing and mechanical fliperon) on the maximum angle that a flap can be deflected without separation [17]

A note on the difference in approach towards attaching an initially detached flow and preventing separation is now in order. Wygnansky et al [17] reports that the determination of minimum C_μ for the prevention or delay of separation can be

determined in a similar manner as that for causing attachment and is centered around reduced frequency range, $2 \sim F^{+} \leq 4$.

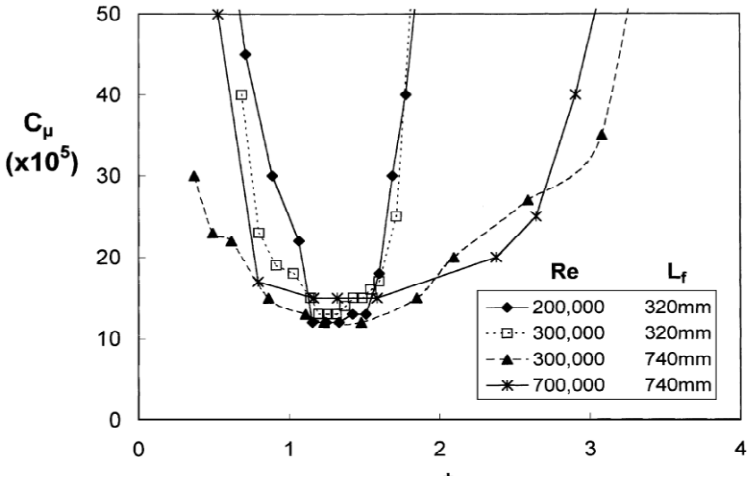

Figure 1-13 Minimum C_μ required to attach an initially detached flow over a flap as a function of F^{+} for different Reynolds number [23]

1.1.4.3 Location of Excitation

In general, periodic excitation must be applied close to the separation point. Examples are excitation applied at the shoulder of a deflected flap [28] or leading edge of a thin airfoil [43]. According to Wygnansky et al. [17], the exact location with respect to the separation point, i.e. slightly upstream or slightly downstream is not clear and may be different for different airfoils. Based on the various past works, excitation close to the leading edge, i.e. $x/c \leq 10\%$ can be effective for a wide variety of airfoils. It must however be noted that separation point on an airfoil moves upstream with angle of attack. Since the actuator cannot be moved once it is installed in the airfoil, the location of

excitation must be found by extensive numerical or experimental optimization with objective functions that meet the practical requirements in the desired situations.

1.1.4.4 Periodic Excitation Applied to Airfoils

The number of disadvantages associated with acoustic excitation, discussed in section 1.1.4.1, necessitated a different approach to excitation that can be practically used on airfoils. In the following paragraphs, work done in the past by numerous researchers using alternative techniques for flow separation control will be discussed, in proper chronological order as much as possible.

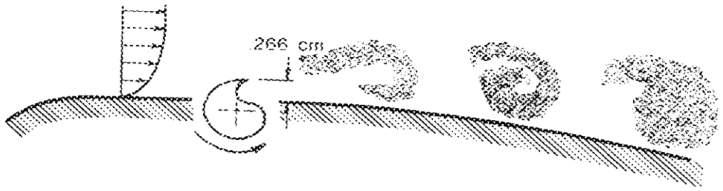

Figure 1-14 Embedded vortex generating mechanical rotor [25]

Viets et al [25] used a cam shaped rotor, shown in Figure 1-14, close to the leading edge on the surface of an airfoil shape, which when rotated generated span-wise vortices. When these span-wise vortices are swept over the surface of the airfoil at high angles of attack, they reduced the size of the separated region and also reduced the pressure on the upper surface. The vortices appeared to bring the high momentum fluid from the outer edge of the boundary layer to the surface, energizing the near wall fluid.

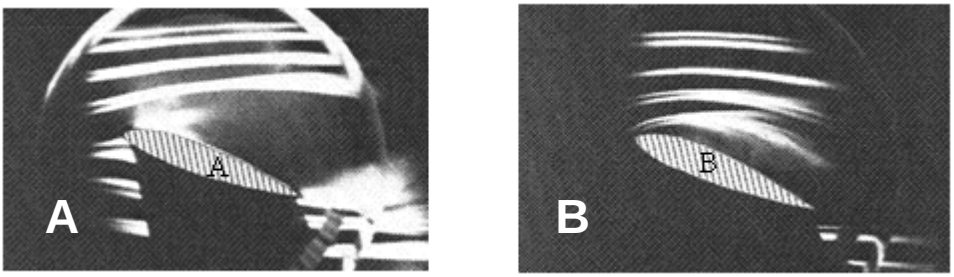

Figure 1-15 Flow visualization of at α=20^o for: A) Ω=0 and B) Ω=2400 rpm [25]

Flow visualization of the flow structure at α=20^o is shown in Figure 1-15. It is seen that the separated streamline is effectively drawn closer to the airfoil surface, reducing the extent of separated region. This reduces the pressure drag on the airfoil, although no quantitative measurement was taken. No detailed pressure measurement over the chord-wise location of the airfoil was taken, due to the preliminary nature of the work. Also, no attempt was made in optimizing the frequency of actuation except that increasing the rotational speed of the rotor decreased the extent of separated region. Furthermore, no attempt was made to optimize the rotor chord-wise location and size of protrusion relative to the local boundary layer thickness.

Wygnansky [26] used a vibrating ribbon on Wortmann airfoil at Reynolds number of Re=200,000. The ribbon was located between 10%-60% from the leading edge and excited at F^+ between 0.3 and 1.8. $\Delta c_{l,max}$ as much as 9.4% was achieved and post stall lift as much as 70 % was achieved.

Bar Sever [27] used an oscillating wire placed 1% ahead of the leading edge of an LRN(1)-1010 airfoil, tested at Re=150,000. The wire was excited between F^+ of 0.7 to

2.7. $\Delta c_{l,max}$ of 12% and post stall Δc_l of 39% were achieved. The amplitude of excitation in this experiment was found to be dependent on frequency. The lift curves with and without excitation are shown in Figure 1-16.

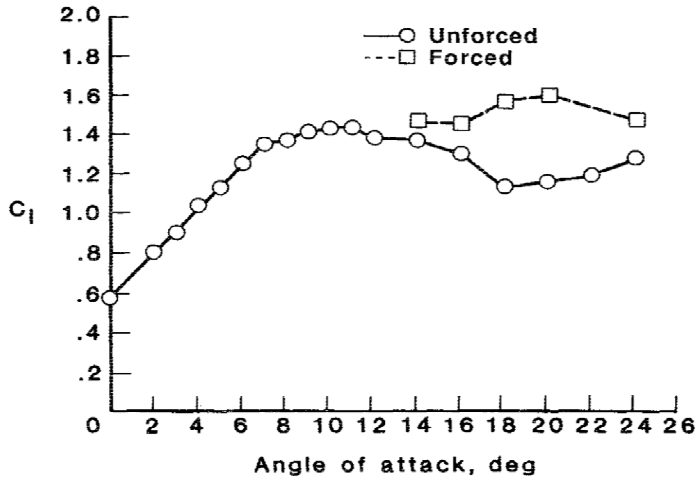

Figure 1-16 Lift coefficient versus angle of attack for unforced and best forced case at R_C=150,000 [27]

Siefert et al [28] used a flaperon at 8 % chord from leading edge of an IAI P255 airfoil tested at Re=200,000 and actuated at F^+=2, based on the distance from actuator location and the trailing edge. This increased $c_{l,max}$ by 8% and post stall lift coefficient by as much as 140%. Significant reduction in form drag was also observed. The airfoil, actuator location and the lift curves of excited and unexcited flow are shown in Figure 1-17.

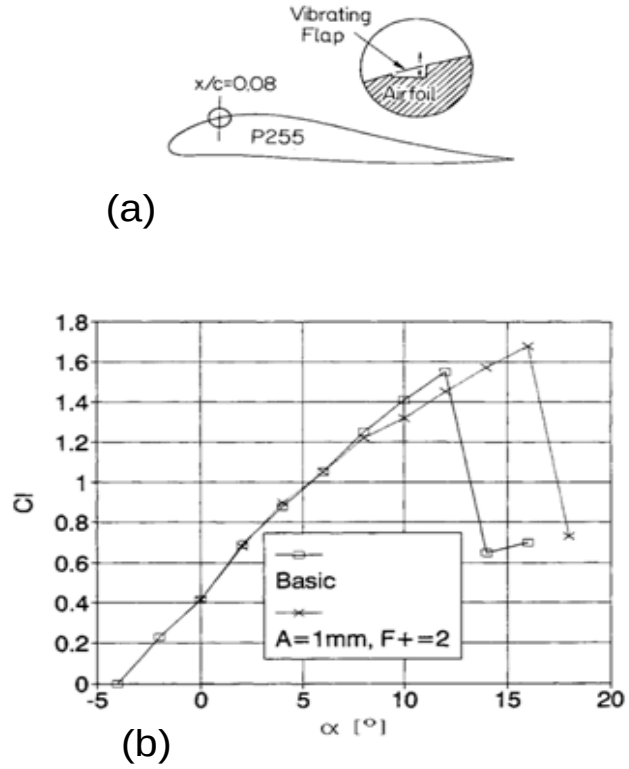

Figure 1-17(a) Vibrating flaperon on an IAI P255 airfoil and (b) comparison of lift between baseline case and excited case [28]

Seifert et al [29] also applied oscillatory blowing superimposed on steady blowing at various points on four different airfoils shown in Figure 1-18.

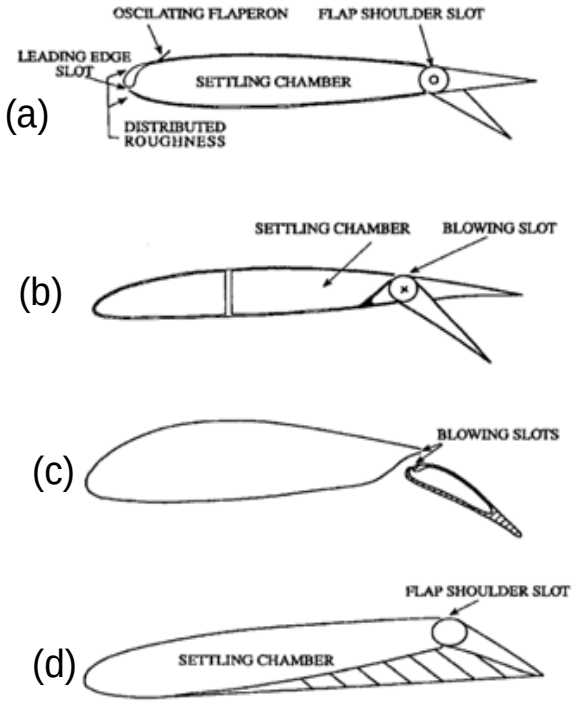

Figure 1-18 a) NACA 0015, b) E214F, c) PR8-40, and d) SPCA-1 [29]

Oscillatory blowing superimposed on steady blowing emanating from the flap shoulder of a flapped-NACA 0015 airfoil was compared with the baseline, i.e. without any blowing, and only steady blowing case as shown in Figure 1-19. The flap was deflected at 20 degrees with respect to the chord. The basic airfoil characteristics at this specified flap deflection angle are improved. Steady blowing at c_μ=0.8% superimposed by oscillatory blowing with c_μ=0.8% at F^+=2 moved the entire lift curve up by Δc_l=0.65 before stall and Δc_l=0.90 at α_{max} of the baseline configuration, translating to an increase of 64% in $c_{l,max}$. The introduction of pure oscillations at F^+=2 reduced the total drag by a

factor of 3.6 at c_l=1. Comparable drag reductions were observed at all lift coefficients less than $c_{l,max}$.

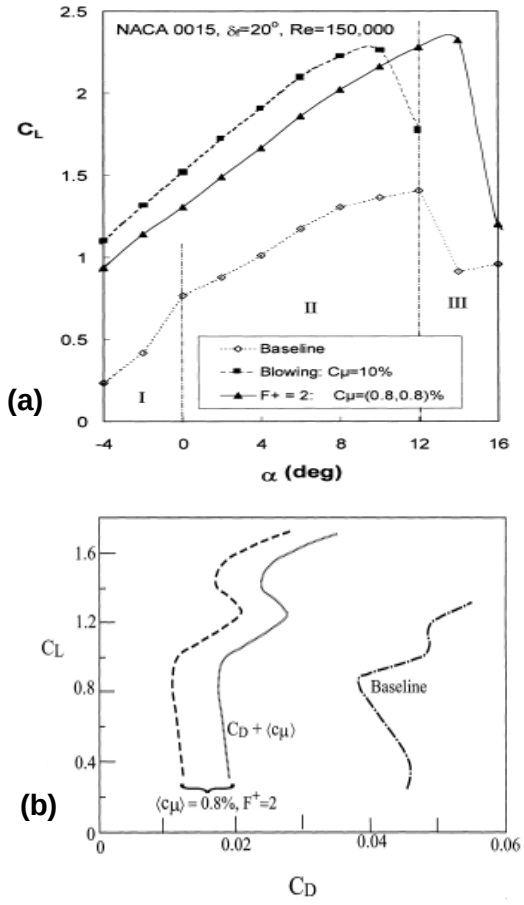

Figure 1-19 Effect of steady and/or oscillatory blowing on the a) CL of NACA 0015 airfoil and b) the drag polar [29]

The E-214 airfoil is 11 % thick airfoil that has a long stretch of laminar flow on the suction surface. It is used as a lifting airfoil for wings. In this experiment, the airfoil is equipped with a 30% flap and has a blowing slot at the trailing edge of the main wing element. A flap deflection of $\delta_f=20^o$ increased c_l three times at $\alpha=0^o$ at R_c=200,000. A

pure oscillatory blowing with $\langle c_\mu \rangle = 0.3\%$ resulted in an additional Δc_l=0.44 at α=0°. Superimposing an equal amount of steady blowing did not result in appreciable improvement. However, only a steady blowing with $c_\mu = 3\%$ was able to outperform the oscillatory blowing at $\langle c_\mu \rangle = 0.3\%$. The comparison of lift curves for these cases are shown in Figure 1-20.

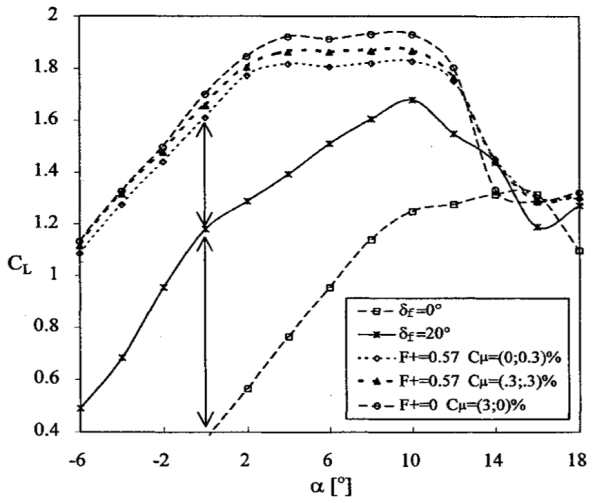

Figure 1-20 Comparison of lift curves due to active control over a 20 degrees deflected flap of Eppler 214 airfoil, R_C=200,000 [29]

The third experiment discussed in [29] involved the PR8-40 airfoil, shown in Figure 1-18(c), designed by the Israel Aircraft Industries to operate at R_C>600,000. The PR8-40 is a 19 % thick airfoil. The goal was to recover the lift lost due to separation over the flap as a result of decreasing Re below its designed value and explore the optimum location for excitation. Oscillations could emanate either form a slot at the trailing edge of the main element or from a slot at the leading edge of the flap. It was found that it is

much more effective to introduce excitation from the top surface of the flap than from the trailing edge of the main element. The oscillations from the trailing edge of the main element enhanced the mixing between the wake of the main element and the potential flow above it, while the excitation from the flap leading edge interacted directly with the new boundary layer over the flap surface. Pressure distributions on the airfoil, with and without oscillations at $\langle c_\mu \rangle = 0.02\%$ for excitation from the tailing edge of the main element and the leading edge of the flap, are shown in Figure 1-21. The flow over the flap is completely separated without excitation. It is mostly separated when oscillation was introduced at the trailing edge of the main element. But the flow is fully attached when same amount of excitation is applied at the leading edge of the flap. The performance of the airfoil was enhanced due to the increased suction as a result of excitation at the trailing edge region of the airfoil-flap assembly.

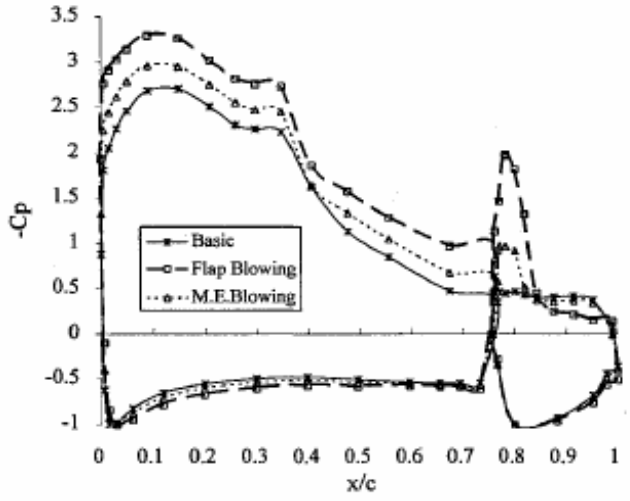

Figure 1-21 Effect of excitation on pressure distribution of IAI PR8-40; R_C=200,000, F^+=2, α=8 deg, δ_f=30 deg, and c_μ=0.02% [29]

The fourth experiment discussed in [29] involved a modified NACA0015 airfoil. The modified airfoil was created by deflecting the flap of the NACA0015 airfoil to 40 degrees and attaching a plate to the lower surface closing the gap between the trailing edge of the flap and the lower surface of the airfoil at x/c=23% as shown in Figure 1-18(d). This was done because sometimes thicker airfoils are desired. The effectiveness of this airfoil, however, relies on oscillatory blowing emanating from the original flap-knee. The baseline airfoil has $c_{l,max}$ of 1.3 at α=16 degrees and R_C=150,000. Steady blowing at c_μ=0.8% did not change the lift coefficient between $0< \alpha< 12$ degrees; it only increased $c_{l,max}$ and α_{max}. On the other hand, oscillatory blowing at F^+=0.75 and $\langle c_\mu \rangle = 0.8\%$ increased $c_{L,\ \alpha=0}$ by 0.6, resulting in a $c_{l,max}$=1.8 at α_{max}=20 degrees. Oscillatory blowing at F^+=2 did not increase $C_{L,0}$ but increased $c_{l,max}$ to 2.

Another example of purely mechanical excitation of the boundary layer over airfoil is discussed by Siefert, Elaihu and Greenblatt [30]. The actuators used are small flaps vibrated by uni-morph type piezoelectric elements. The resonance frequency of each actuator was approximately 170 Hz and its tips vibrated to a maximum of 13 mm peak to peak. The actuators are installed at 41% chord from the leading edge on a (IAI) Pr8-40-SE airfoil with a chord of 360mm and span of 609mm, width of the test section. This is shown in Figure 1-22. A transition strip (grit no. 100) was located at the leading edge region of the airfoil from x/c=0.03 on the lower surface to x/c=0.05 on the upper surface. The test was conducted in a closed circuit, low turbulence and low-speed wind tunnel with a 2-ft-wide, 3-ft-high and 20-ft-long test section.

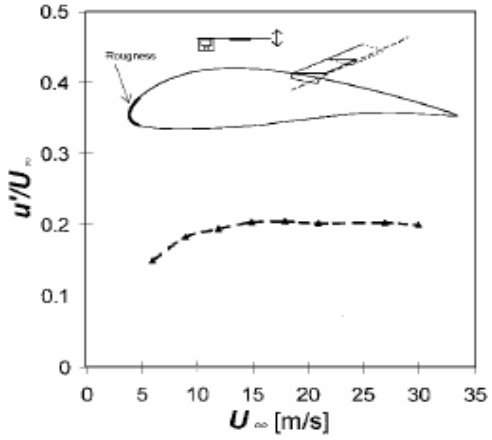

Figure 1-22 (IAI) Pr8-40-SE airfoil with the actuator [30]

The actuators were excited in two different modes. The first mode, called two-dimensional mode, involved the actuators operating at identical amplitude and phase. The second mode, called three-dimensional mode, involved the actuators operating at same amplitudes nut with the phase of the alternate actuators reversed. The lift vs. angle of attack plot is shown in Figure 1-23 and the lift vs. drag is shown in Figure 1-24.

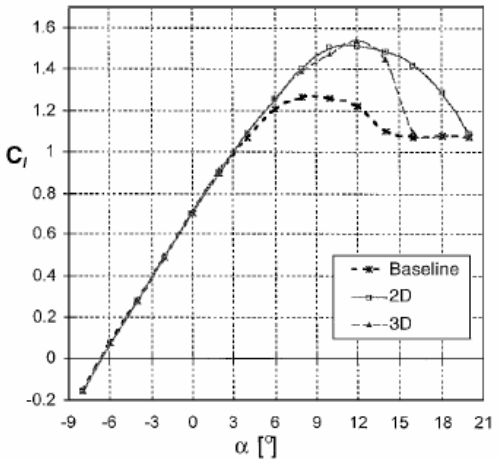

Figure 1-23 Lift vs. angle of attack at F^{+}=1.2 and R_C=550,000 [30]

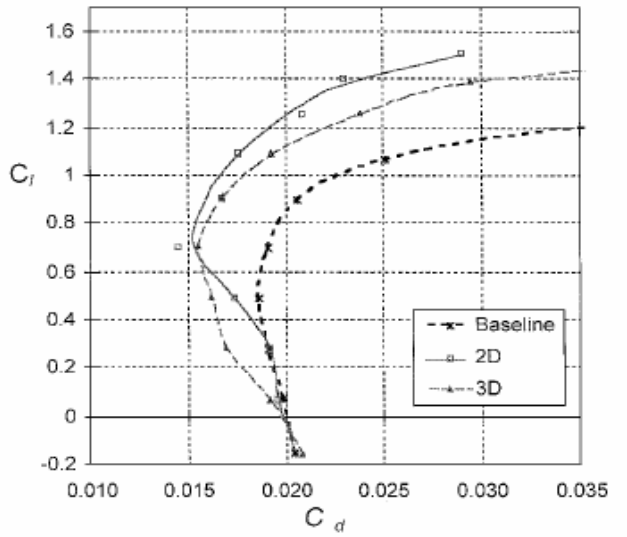

Figure 1-24 Lift vs. drag at F^+=1.2 and R_C=550,000 [30]

Observe that $c_{l,max}$ was increased by 20-22%, regardless of excitation mode. The two-dimensional mode results in milder post-stall behavior than the tree-dimensional mode. The drag without actuation diverges quickly for c_l>0.7; the drag divergence of the two and three-dimensional modes is comparatively milder. Two-dimensional mode generates the highest L/D at the highest c_l. Three-dimensional mode consumed less power compared to the two-dimensional mode of excitation. From the point of view of power consumption, it is expedient to operate in the three-dimensional mode at c_l>0.7 and in the two-dimensional mode at c_l>1.2.

A more recent investigation, similar but not necessarily involving the same flow control mechanism as the preliminary work by Viets et al. [25], was carried out by Younwhe Park, Soogab Lee and Dongho Lee [32]. The experimental investigation in this work used a NACA 0012 airfoil. The actuator is called a surface buzzing rod that

involves a rod and spans the entire airfoil and is vibrated by an eccentric cam inside the airfoil, which itself is rotated by a motor outside the test section as shown in Figure 1-25.

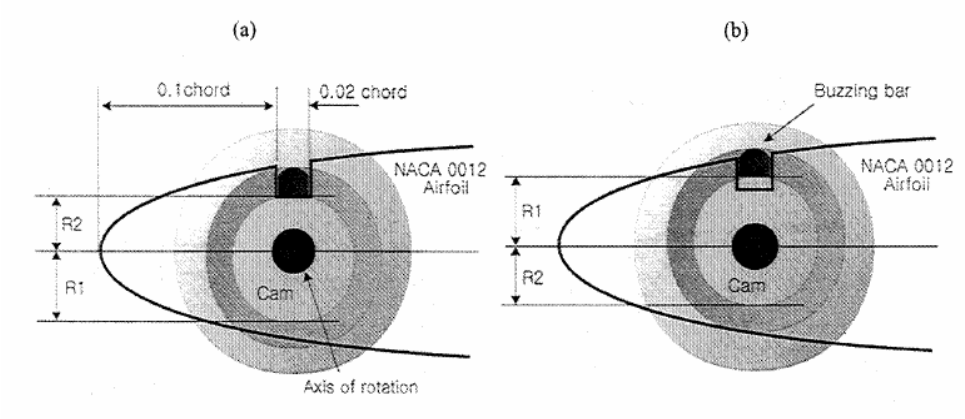

Figure 1-25 Local surface buzzing; amplitude=R1-R2=2.6 mm a) when the buzzer is at lowest position, b) when the buzzer is at highest position [32]

The buzzing rod was located at x/c=0.1~0.12. The tests were conducted at R_C=200,000 without a transition trip. The investigators consider the method to be based on the idea that local surface buzzing perpendicular to the flow direction near the leading edge can energize the retarded flow in the separated region and produce large coherent vortex structures. At R_C=200,000, excitation provided improvement at post stall angles. Excitation improved neither the pre-stall lift nor lift at stall by a significant amount as shown in Figure 1-26. It provided a stall delay angle of about 1 degree. It also appears that increasing the frequency of excitation increased the gain in lift at a given angle of attack for the frequencies tested in that experiment.

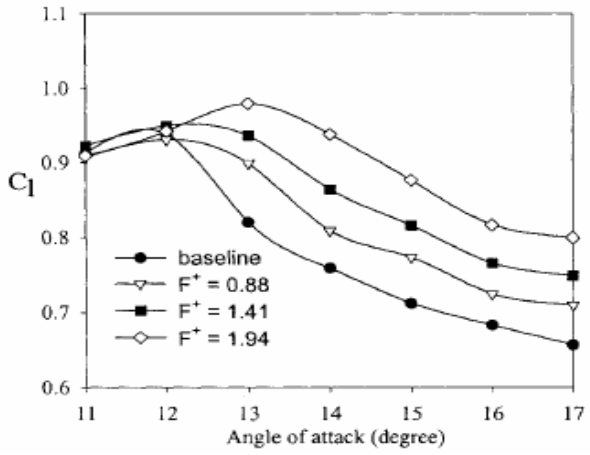

Figure 1-26 Comparison of the lift coefficient curves for various buzzing frequencies; R_C=200,000 [32]

Recently synthetic jet actuators have gained popularity in the research community especially with respect to airfoil performance improvement. The synthetic jet actuator was invented by Smith and Glezer [33] in the mid 1990s. Also called zero net mass flux actuator, these actuators generate vortices that interact directly with the boundary layer. This is achieved in such a way that no net mass is added to the flow. In construction, it consists of a cavity and an orifice. One of the walls of the cavity has a diaphragm that is vibrated by a piezoelectric driver, as shown in the Figure 1-27. The intermittent deflection of the diaphragm causes periodic suction and blowing through the orifice, generating vortices.

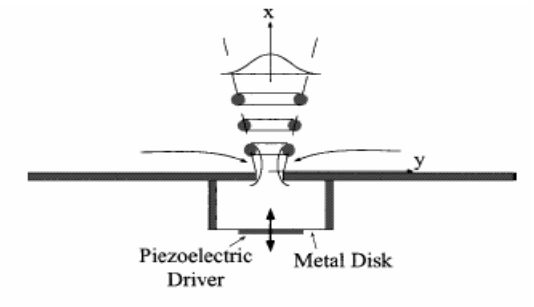

Figure 1-27 Schematic of a synthetic jet actuator

A.C. Miller [34] applied synthetic jet actuation at the leading edge of a NACA0015 airfoil. In the smoke flow visualization picture shown in Figure 1-28, observe that with the actuation at the leading edge, the separated streamline is effectively drawn closer to the surface of the airfoil so that the extent of separated flow is reduced. The leading edge synthetic jet delayed the onset of stall up to 25 degrees angle of attack.

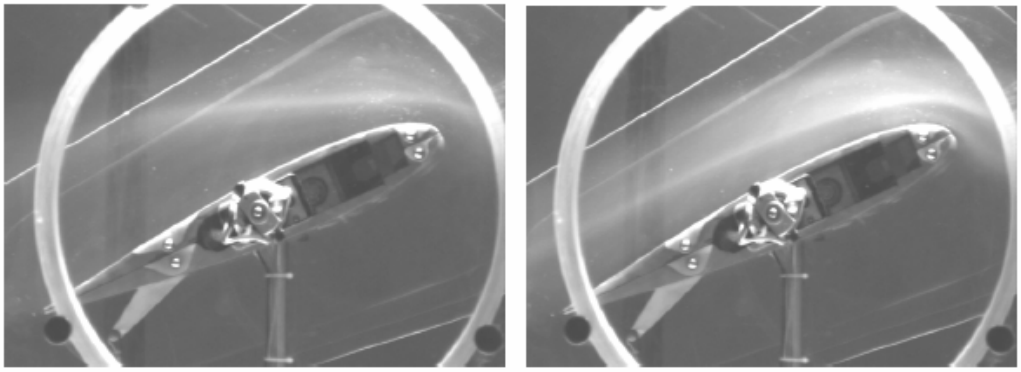

Figure 1-28 NACA0015 with (right) and without (left) synthetic jet actuation [34]

Kim et al [31] conducted a CFD study of the effect of synthetic jet actuation on an NACA 23012 at Reynolds number of 2,190,000. Two of the notable cases investigated in this work are: case one, a single synthetic jet was located at 12-percent chord of the airfoil; case two, a synthetic jet was located at the shoulder of a 30 degree deflected flap at the trailing edge. The major control parameters in the study were: jet peak velocity from 1 to 3 times the free stream velocity, non dimensional frequency ranging from 0.5 to 5. The characteristic length used to normalize the frequency of actuation was the distance from the actuation location to the trailing edge. The results of the simulation are shown in Figure 1-29.

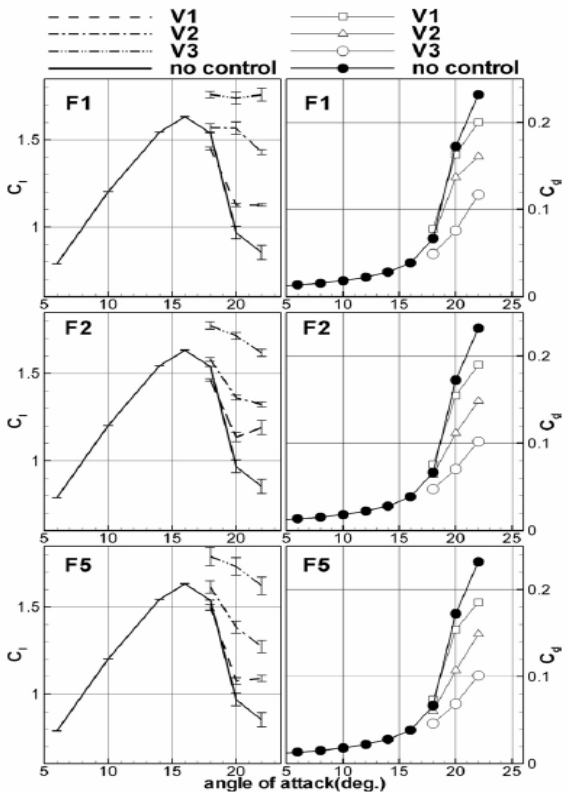

Figure 1-29 Aerodynamic coefficients with non-deflected flap (single synthetic jet at 12% chord) [31]

In case one, the synthetic jet was located at 12-percent chord, which corresponds to the separation location on the baseline airfoil at angle of attack of 20 degrees. The inclined angle of the synthetic jet was 23 degrees with respect to the local tangential airfoil surface and it was fixed for all the cases. It was observed that the enhancement of lift and drag is proportional to the amplitude of synthetic jet velocity, meaning higher the amplitude, the better. V1, V2 and V3 simply corresponds to the amplitude of synthetic jet actuation, with V1 the lowest and V3 the highest. F1, F2, F5 corresponds to non dimensional frequencies. The following conclusions were drawn by the authors with respect to the maximum lift enhancement: the approximate non-dimensional frequency is 1, the location of synthetic jet slot is close to the baseline separation point; and the jet velocity is large enough to excite the surrounding separated flow.

In case two, synthetic jet is located at 80-percent chord, shoulder of the flap. The lift coefficient before stall is greatly improved when the non dimensional frequency is 1. As the amplitude is increased, the lift coefficient becomes higher at the same non dimensional frequency. After 16 degrees, at which leading edge stall occurs, similar improvement was not observed. This is because the synthetic jet is now within the separated region, as opposed to being close to the separation point. Refer to Figure 1-30.

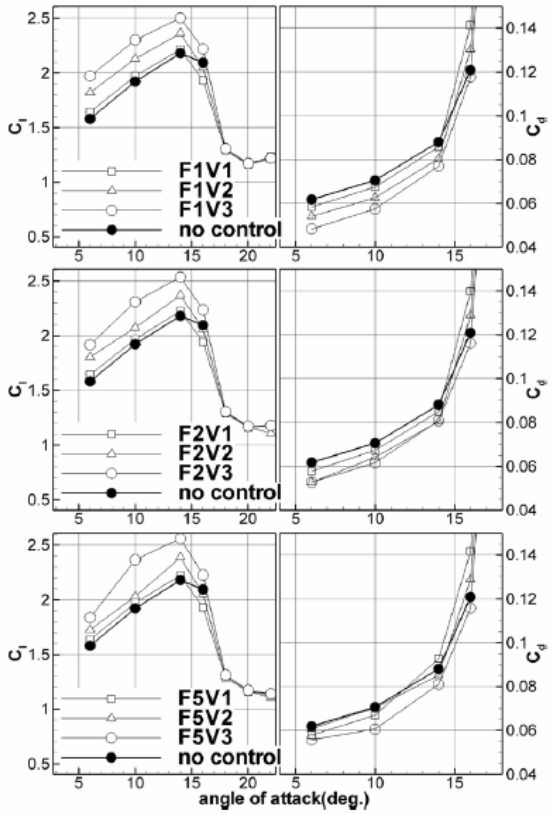

Figure 1-30 Coefficients with a 30 deg deflected flap (single synthetic jet at 80% chord) [31]

Combustion based fluidic actuators were designed and tested for airfoil flow control by Barta and Glezer [35]. These actuators are net-mass-flux actuators, as opposed to zero-mass-flux actuators which synthetic jets are. By construction, a combustion based fluidic actuators consists of a chamber, orifice and inlets for air and fuel as shown in Figure 1-31. Air and fuel injected into the chamber are periodically burned by a spark igniter, generating high speed jets through the orifice which interacts with the boundary layer.

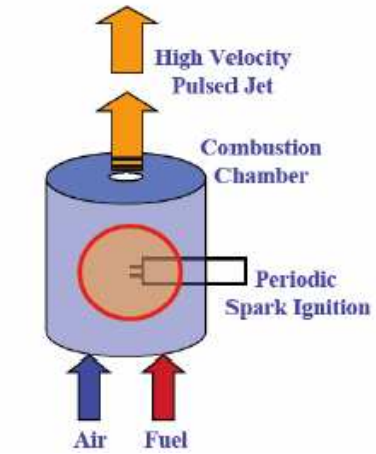

Figure 1-31 Combustion based fluidic actuator

Single Dielectric Barrier Discharge (SDBD) or plasma actuators, shown in Figure 1-32, are in development and their application in aerodynamic flow control is being investigated. The plasma is formed by applying a high frequency, high voltage AC signal across an asymmetric pair of electrodes separated by a dielectric barrier. The electric field ionizes the air molecules in the space above the insulated electrode, forming plasma which extends from the exposed electrode through the length of the insulated electrode. The plasma induces a velocity in the surrounding fluid that can serve as a mechanism for flow control. One of the important downsides of this actuator is that since the force generated is proportional to the ambient pressure, its utility at cruising altitude is limited.

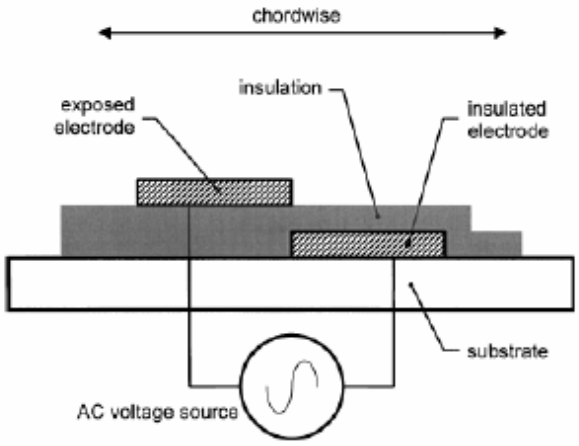

Figure 1-32 Schematic of a plasma actuator [36]

1.1.4.5 Implementation on Actual Flight Vehicle

A major obstacle in the way of achieving realistic flow control on actual flight vehicles is the actuators. A robust and energy efficient actuator can greatly increase the possibility of successful implementation of active flow control on full scale systems. A joint program of the University of Arizona, the Illinois Institute of Technology, Tel Aviv University, Bell Helicopters, and Boeing, under the sponsorship of the Micro Adaptive Flow Control (MAFC) of DARPA [37], to reduce the download during hover of a XV-15 tiltrotor aircraft is the first full scale application of active flow control. The flaps and ailerons were fitted with zero mass flux or synthetic jet actuators. The flight tests documented a reduction of a download in hover by 9-14% over the baseline. The test aircraft and the actuator placements are shown in Figure 1-33.

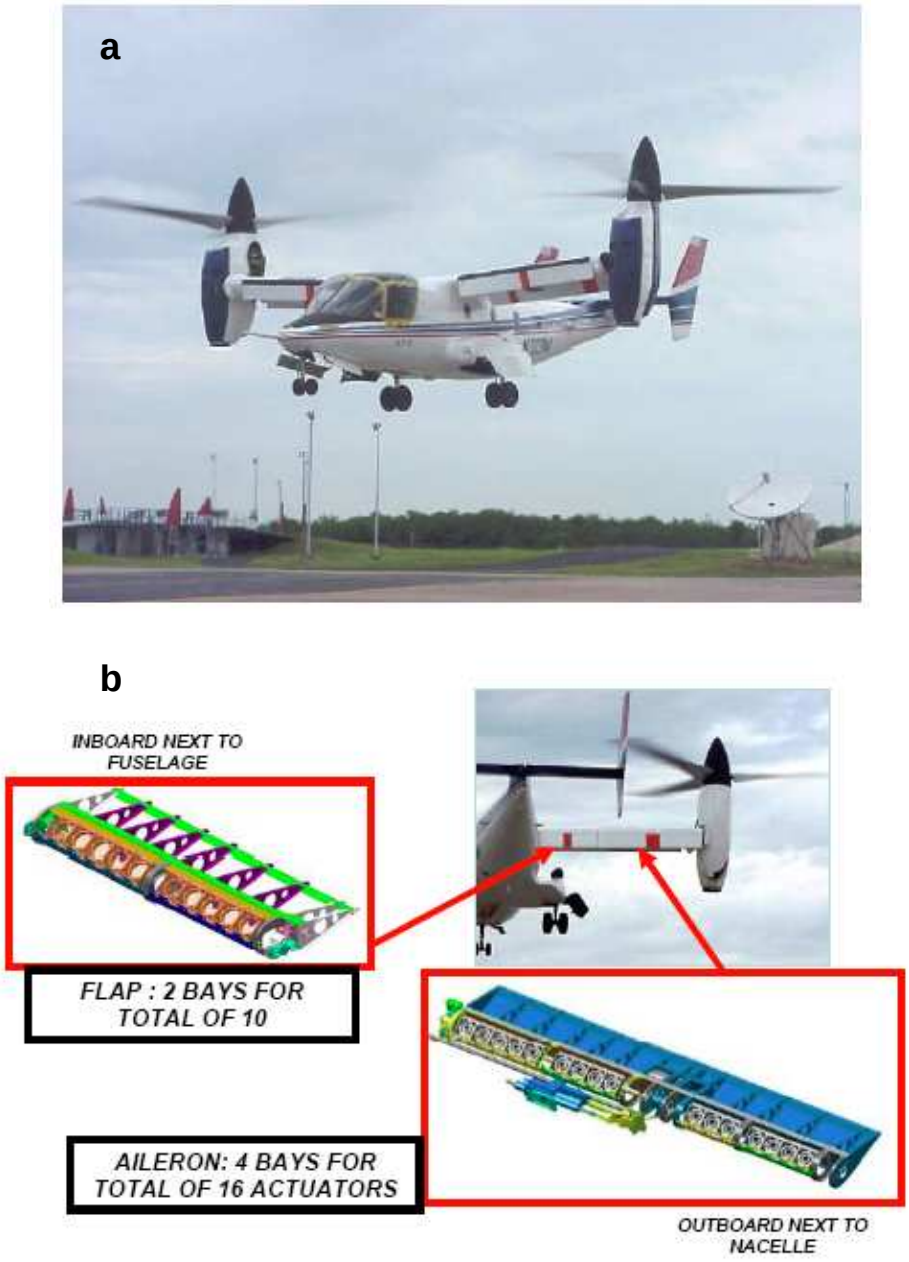

Figure 1-33 a) Bell XV-15 tiltrotor, b) XV-15 AFC flap design [37]

1.2 Background and Motivation of the Current Investigation

Various methods discussed earlier have proven effective in mitigating the effects of separation and enhancing aerodynamic performance. However, they possess drawbacks that are inherent to their respective designs. For example, suction and blowing devices, whether oscillatory or steady, involve complex plumbing. As discussed in section 1.1.2, complex plumbing of a suction/blowing system leads to excessive weight increase of the whole system. Moreover, their power consumption is perhaps too high for them to be feasible for practical application to real systems like aircraft. On the other hand, synthetic jet actuators require low power and involve far lower weight. However, the orifices involved present an inherent drawback. They are susceptible to clogging due to, for example, operation in dusty environment, which limits their operational time and effectiveness.

Against this background, the development of a new flow control method that is free from the aforementioned drawbacks is certainly warranted. A novel flow control method called dynamic roughness was suggested by W.W. Huebsch [39], shown in Figure 1-34, and followed up with a preliminary CFD investigation by Honsaker and Huebsch [40]. Dynamic roughness involves physical bumps on the aerodynamic surface that protrude into the flow when extended and remains flush with the surface when contracted. The fact that this is done periodically gives it the name “dynamic.” The numerical simulations in [40] involved two dimensional roughness geometries in the leading-edge region of an airfoil. A parametric study was conducted to study the

effectiveness of dynamic roughness in delaying flow separation and the following observations were made:

1. Dynamic roughness showed little sensitivity to the Reynolds number range tested.
2. As the frequency of dynamic roughness is decreased, the flow eventually experiences an effective static roughness.
3. When the roughness height is decreased to a very small percentage of the boundary-layer, it ceases to be effective and the flow separates as if the airfoil is clean.
4. Dynamic roughness was still quite effective in dynamic stall at higher Reynolds number.

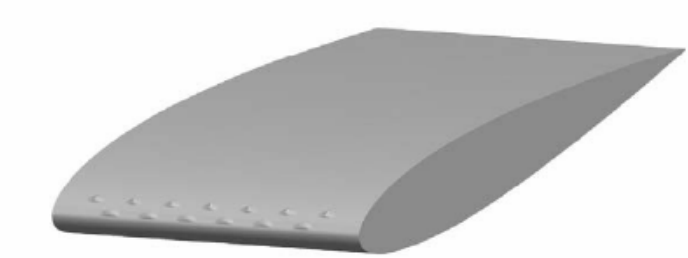

Figure 1-34 The concept of dynamic roughness

It must however be mentioned that the CFD study considered the flow property only around the leading edge region of the airfoil shape and did not look at the flow characteristics downstream.

Since the dynamic roughness studied was applied to the leading edge, the effect is to modify the laminar boundary-layer characteristics. However, performance improvement of airfoils often involves delaying stall and modifying turbulent separation characteristics close to the trailing edge. With this in mind, a preliminary proof-of-concept experiment was conducted by Yang et al. [38] at the Pennsylvania State University subsonic-closed-return wind tunnel. The study used SM701 airfoil, which stalls from the trailing edge, with dynamic roughness located at 70-percent chord from the leading edge, which corresponds to turbulent separation at stall, based on XFOIL. **Figure 1-35** shows dynamic roughness prototype with tufts mounted in the wind tunnel. The roughness elements are vibrated with piezo-bender actuation system. The span of the airfoil model is smaller than the width of the wind tunnel and hence it must be considered a three-dimensional test.

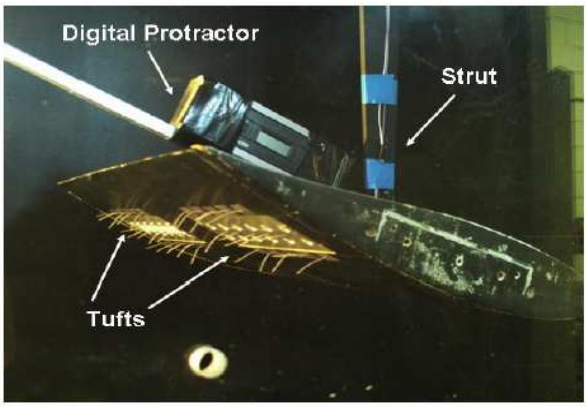

Figure 1-35 Dynamic roughness prototype with tufts mounted in the wind tunnel

Wind-tunnel testing of dynamic roughness actuated at a frequency of 30 Hz applied to this airfoil at R_C=117,000 provided promising results based on observations of the behavior of tufts attached to the upper surface of the airfoil. Although no measurement of the aerodynamic forces were made due to the inoperability of the existing force balance system, tuft flow visualization provided clear indication of the effect of dynamic roughness on the flow.

It was observed that dynamic roughness was effective in keeping the flow attached only when it was turned on and the angle of attack was increased from a low value to higher values towards stall. It however failed to reattach the already separated flow. Never-the-less, it is observed in Figure 1-36 that, when the airfoil is at 17 degrees with the actuator already turned on, the tufts are behaved which indicates the flow is attached. When dynamic roughness is turned off at the same angle of attack the tufts immediately indicate separated flow. This was observed to be a dramatic indication of the effect of dynamic roughness on the flow over the airfoil.

Figure 1-36 Tufts indicating attached flow due to dynamic roughness turned on at 17 degrees angle of attack. [38]

Figure 1-37 Tufts indicating separated flow due to dynamic roughness turned off at 17 degrees angle of attack. [38]

It should be noted that the digital protractor is fixed to the sting at an angle of 6 degrees with respect to the airfoil chord, hence the discrepancies in readings on the protractor and the actual geometric angle of attack.

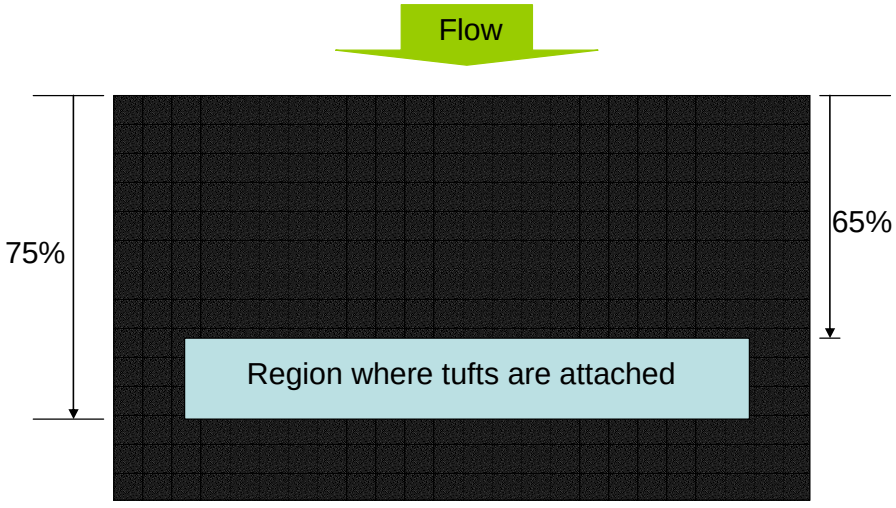

Figure 1-38: Region on the airfoil where the tufts are attached

Since only tufts were used to observe the effect of dynamic roughness and force balance was not used to measure the exact delay of stall due to dynamic roughness, a term “virtual stall” was defined such that the airfoil is considered virtually stalled unless all the tufts shown in Figure 1-39 are behaved and vice versa. One of the noteworthy results from the experiment is shown in Figure 1-39, in which the virtual stall angle of attack is plotted against free stream velocities for the cases with and without dynamic roughness actuation. Two important conclusions could be drawn from this result. One, dynamic roughness is effective in delaying virtual stall. Two, stall delay at the constant actuation frequency of 30 Hz decreases with an increase in free stream velocity. The second conclusion points to a possible dependence of the dynamic roughness actuation on a non dimensional frequency in improving performance.

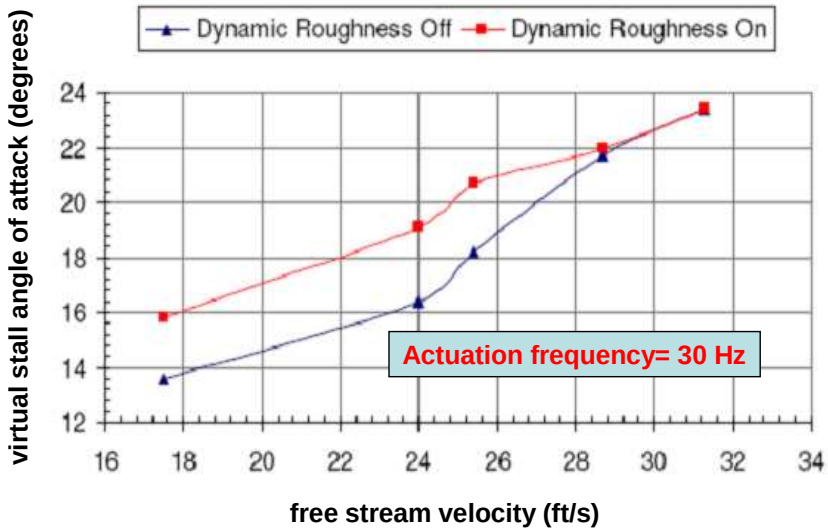

Figure 1-39 Effect of velocity on the effectiveness of dynamic roughness at low R_C range around 120,000 [38]

With the preliminary CFD results of Honsaker and Heubsch [40], the experimental observations by Yang et al. [38] coupled with potential advantages of dynamic roughness over the other popular flow control methods discussed earlier, a further investigation of the concept was warranted. An experimental investigation of dynamic roughness was hence conducted.

1.3 Research Objectives

Wind tunnel tests indicated the potential for significant advantages in virtual stall delay due to dynamic roughness actuation. The ideal configuration to promote boundary layer control would be an actuation device that avoids exposing holes that could possibly clog. The system should also present a smooth surface in nominal flight conditions where no flow control is required. A suitable actuator should also allow for variable excitation frequencies matching flow condition. To achieve this ideal system, and to better understand the fundamental physics behind the observed phenomenon, the following research objectives are proposed:

1. To design, fabricate and test a dynamic roughness actuator that is not only able to provide excitation ranging from 100Hz to 400Hz but also able to change the frequency continuously.
2. To identify the optimum dynamic roughness shapes.
3. To experimentally study the effects of excitation frequency on boundary-layer control

4. To perform an experimental investigation of the effect of dynamic roughness height
5. To identify the ideal chord-wise location of excitation for maximum performance improvement.

This thesis describes the work conducted to achieve these objectives.

1.4 Outline of the Thesis

Chapter 2 discusses the design and development of a facility for airfoil testing. Chapter 3 discusses the design and development of a dynamic roughness actuator to support fundamental research. The first part of chapter 4 discusses the work on dynamic roughness applied to a two-dimensional NACA 23012 airfoil, the second part covers experiments performed on HTR1555 airfoil with a dynamic roughness actuator. The third part of chapter 4 discusses the results of the experiment on SM701 airfoil with dynamic roughness. Chapter 5 summarizes the work discussed in this thesis. Chapter 6 discusses recommendations for future work.

Chapter 2

DESIGN AND DEVELOPMENT OF A MECHANISM FOR TWO-DIMENSIONAL AIFOIL TESTING

Aerodynamic forces were not measured on SM701 airfoil discussed in section 1.2 to which dynamic roughness was applied for preliminary proof of concept tests. The resulting lack of aerodynamic data prevented one from drawing any definite conclusion from the experiment with regard to the effectiveness of dynamic roughness in improving airfoil performance. The reason the forces were not measured was that the existing force balance system at the Penn State subsonic wind tunnel was not functioning properly and hence was unreliable in obtaining accurate data. It was hence proposed to design a facility that could not only measure the aerodynamic forces on an airfoil, but would also allow for automatic adjustment of the angle of attack. This facility would not only be useful for the research project that is discussed in this thesis, but would also be a new addition to the wind tunnel that is also used for academic purposes, including aerospace laboratory classes. In this chapter design and development of this facility will be discussed.

2.1 Requirements of the System

The design of a system that can measure the aerodynamic forces on a model in the Penn State low-speed wind tunnel, shown in Figure 2-1, was proposed. The model could be either an airfoil or any other shape whose aerodynamic characteristics are to be determined through force measurements. This system should also be able to change the angle of incidence of the model without having to exert manual effort which could cause inaccuracy in measurements. Most importantly, the force balance used in this system should be able to withstand a maximum amount of force or moment encountered that is limited by the size of the airfoil and the capability of the wind tunnel

Figure 2-1 Schematic of the Hammond low-speed wind tunnel

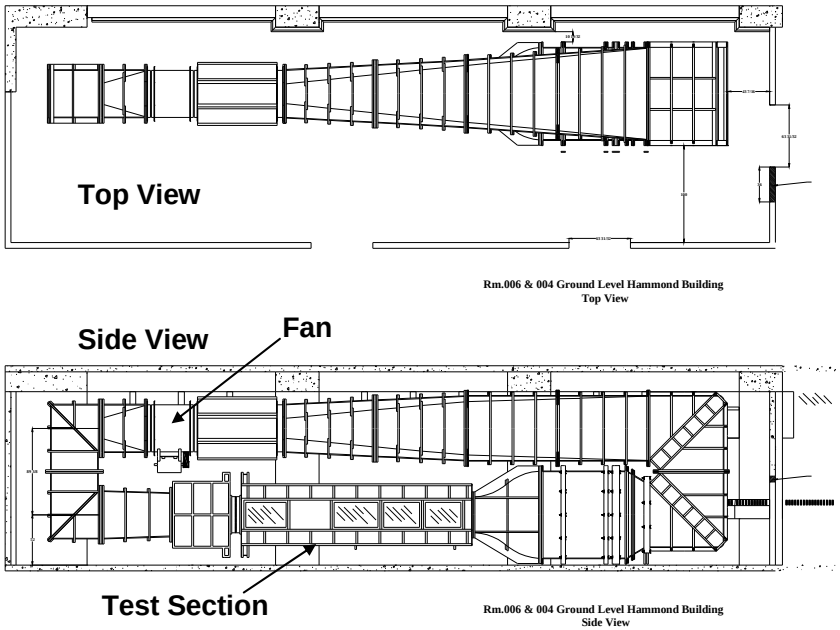

2.2 Conceptual Design of a Prototype

With the above requirements in mind, a rotating window mechanism was proposed. The system consists of a circular window, rotating within an outer fixed ring, and rotated by a system of gears mounted on a shaft under the test section floor that is, in turn, driven by a motor on the far side of the test section. A strain gage force balance was proposed to be used for this system which would be fixed to the reference frame of the window. The conceptual design of the system is shown in Figure 2-2.

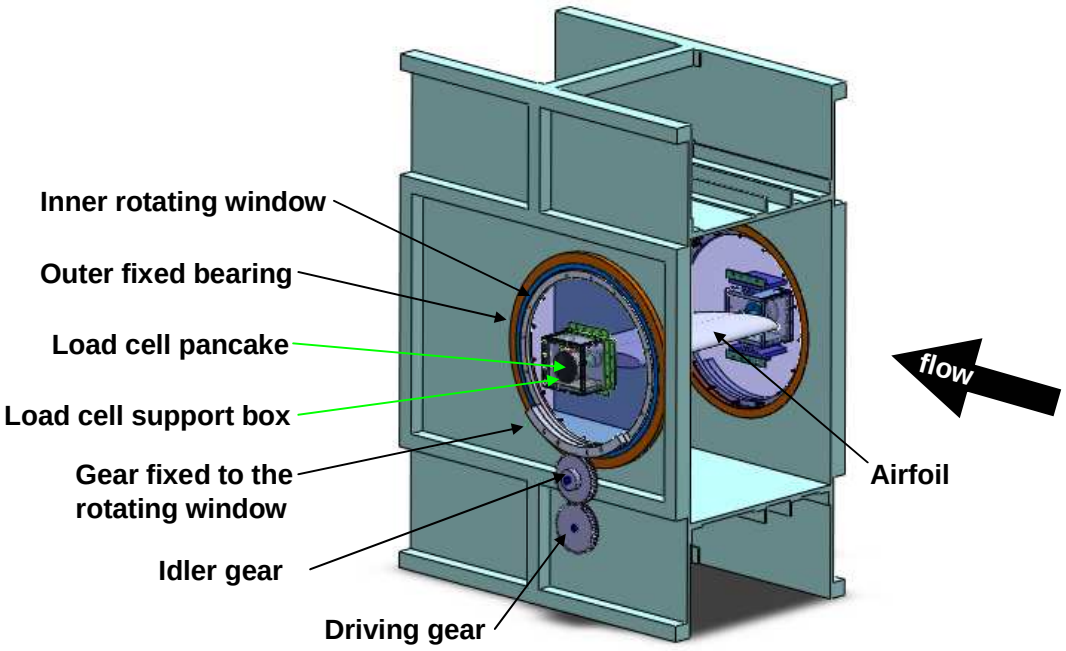

Figure 2-2 Three-dimensional view of a conceptual design of a system for aerodynamic force measurement

2.2.1 Estimation of the Maximum Forces and Moments

In order to select a suitable force sensor and the driving motor that can operate in the proposed system, an estimate of the applied loads, including aerodynamic and dead loads, involved in a typical airfoil test is required. Estimations were based on the aerodynamic characteristics of an NACA 23012 airfoil that spanned the width of test section. The upper limit of the allowable speed range for the wind tunnel is 140ft/s. The specification of the airfoil model is given in Table 2 and the constants for the air properties used in the calculations are shown in Table 3.

Chord, c	0.3556 m
Span, s	0.7112 m
Plan-form area, A	0.2529 m^2

Table 2: Specification of NACA 23012 airfoil model used for estimation of maximum forces

Standard density, ρ	1.225 kg/m^2
Standard kinematic viscosity, ν	1.43 x 10^{-5} m^2/s

Table 3: Properties of air used for estimation of maximum forces

Based on the above information maximum chord Reynolds number was calculated to be:

$$R_{c,\max} = \frac{U_{\infty,\max} c}{\nu} = 1,025,733$$

For this Reynolds number the aerodynamic coefficients are chosen based on documented experimental data for NACA 23012 as shown in Table 4.

$c_{l,max}$	1.5870	$\alpha = 16^0$
$(c_d)_{max}$	0.2000	$\alpha = 23^0$
$(c_m)_{max}$	-0.064	$\alpha = 23^0$

Table 4: Maximum aerodynamic coefficients for maximum load calculation

With a flow control actuator turned on, a 30 % increase in the lift and pitching moment coefficients were assumed. Although a particular flow control method may decrease drag, there could be instances where drag increase may be caused by irregularities in profile due to either deliberate addition of roughness or by structural deformation of the model during testing. A 30 % increase in drag was also assumed for this reason. With these assumptions the updated maximum coefficients are shown in Table 5.

$c_{l,max}$	2.0631	$\alpha = 16^0$
$(c_d)_{max}$	0.26	$\alpha = 23^0$
$(c_m)_{max}$	-0.0832	$\alpha = 23^0$

Table 5: Updated maximum force coefficients for maximum load calculation

Using the aerodynamic coefficients given in Table 5, the dimensional forces were calculated using the following equations:

$$L_{\max} = C_{l,\max} \frac{1}{2} \rho V^2 A \qquad \textbf{Eqn. 6}$$

$$D_{\max} = (C_d)_{\max} \frac{1}{2} \rho V^2 A \qquad \textbf{Eqn. 7}$$

$$M_{\max} = (C_m)_{\max} \frac{1}{2} \rho V^2 Ac \qquad \textbf{Eqn. 8}$$

The estimated maximum aerodynamic forces are tabulated in Table 6. When the model is mounted in the force balance, its own dead weight will contribute to the total force that the force sensor will have to withstand. However, the effect of weight which acts vertically downward in the reference frame of the laboratory will be to counteract the aerodynamic lift generated when the airfoil is being tested. While not being tested, the weight of the airfoil, estimated to be 295, is still less than L_{max} calculated here.

L_{max}	580.997 N
D_{max}	73.219 N
M_{max}	-8.3318 N-m

Table 6: Maximum aerodynamic forces

2.2.2 Selection of Force Sensor

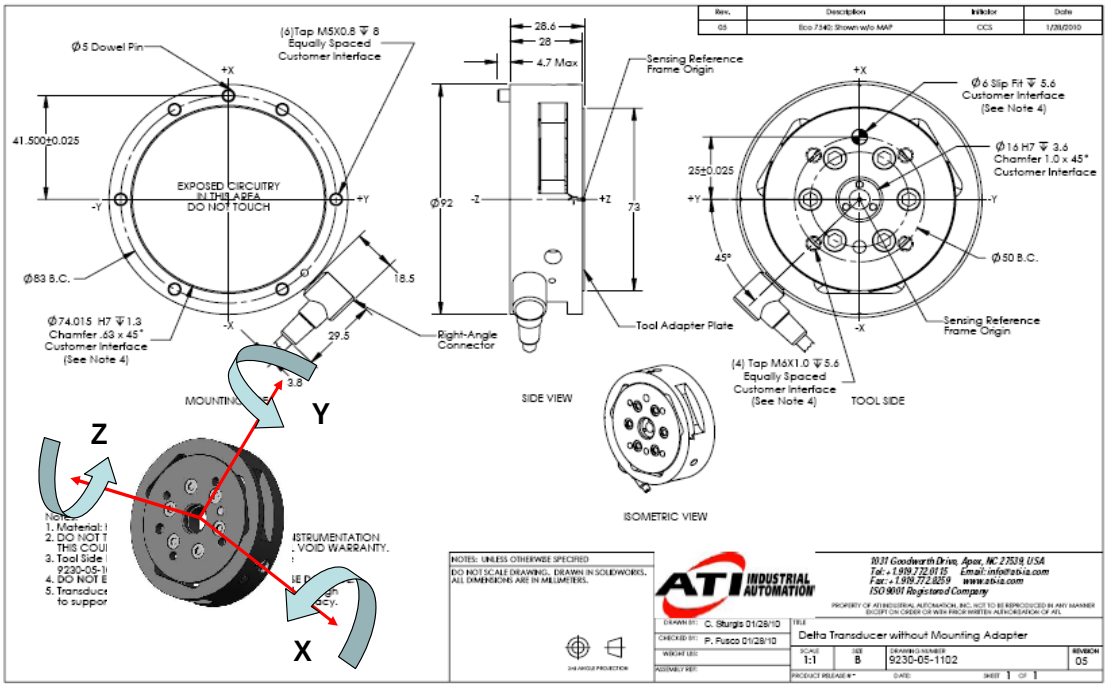

Figure 2-3 Schematic of the six axis strain gage-type load cell chosen for the proposed wind tunnel force balance system with the sensing directions specified [www.ati-ia.com]

Based on the estimates of the maximum forces that might be involved in a typical wind tunnel testing of an airfoil, a Delta six axis strain gage type load cell manufactured by ATI Industrial Automation was found to be suitable for the desired application. The schematic of the load cell is shown in Figure 2-3 and the specifications are shown in Table 7. The six axes load cell can measure three moments and three forces in their respective directions as shown in Figure 2-3. Two load cell pancakes were proposed to be used, one on each side of the test section. However, the load cell on the far side would be a dummy, meaning it would contain no sensor but it would still have exactly the same

construction. Hence the total loads given in Table 6 would be divided equally between the two load cells.

Calibration	F_x,F_y	F_z	T_x,T_y	T_z	F_x,F_y	F_y	T_x,T_y	T_z
SI330-30	330 N	990 N	30 Nm	30 Nm	1/16 N	1/8 N	5/1333 Nm	5/1333 Nm
	SENSING RANGES				SENSING RESOLUTIONS			

Table 7: Sensing ranges and resolution of Delta load cell

Single-Axis Overload	
Fxy	±2600 N
Fz	±8600 N
Txy	±290 Nm
Tz	±400 Nm
Stiffness (Calculated)	
X-axis & Y-axis forces (Kx, Ky)	$3.6x10^7$ N/m
Z-axis force (Kz)	$5.9x10^7$ N/m
X-axis & Y-axis torque (Ktx, Kty)	$5.2x10^4$ Nm/rad
Z-axis torque (Ktz)	$9.1x10^4$ Nm/rad
Resonant Frequency (Measured, non-IP version)	
Fx, Fy, Tz	1500 Hz
Fz, Tx, Ty	1700 Hz
Physical Specifications	
Weight*	0.913 kg
Diameter*	95 mm
Height*	33 mm

Table 8: Specifications of the load cell

The range and resolution of the load cell are shown in Table 7. In comparison with the maximum aerodynamic forces calculated in Table 6, it should be able to not only withstand the estimated forces but also carry a comparable additional model weight. The resolution levels of the forces and moments were found to be appropriate for the desired application.

2.2.3 Estimation of Mechanism Torque and Selection of Driving Motor

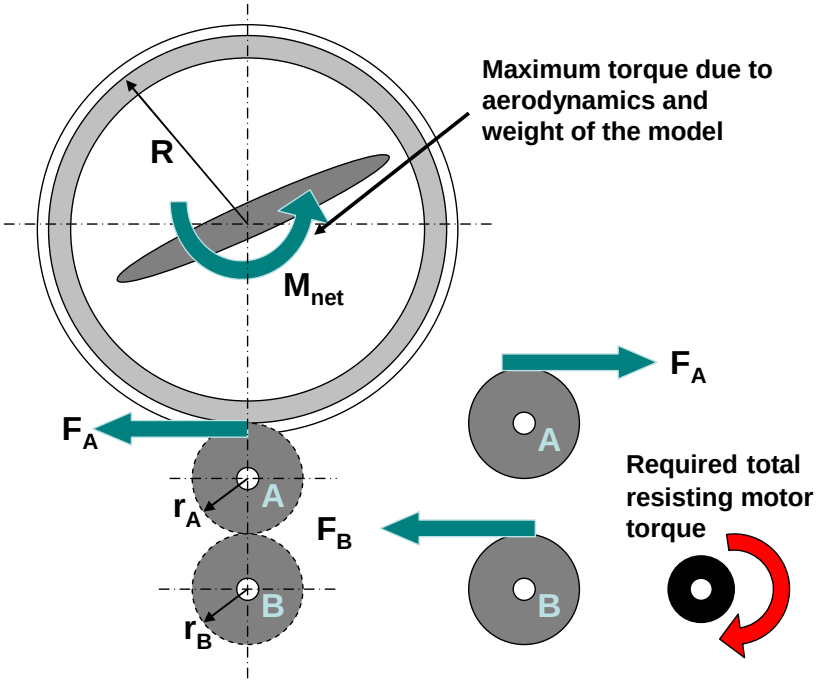

Figure 2-4 Schematic of the forces and moments involved in the mechanism

Since the rotating window mechanism is driven by a motor through a series of gears at the sides of the wind tunnel test section, proper selection of a suitable driving

motor required estimation of the maximum torque involved. The forces and moments involved in the mechanism are shown in Figure 2-4.

The net force and moment due to aerodynamics and weight of the model is shared equally between the gears at both sides of the test section. But for simplicity, the pairs of gears on either side could be joined together so that in two-dimensional space it effectively looks as it is shown in Figure 2-4.

A simple static analysis was performed to estimate the total torque required by the driving motor to resist. In Figure 2-4, M_{NET} is the net moment due to aerodynamic forces and moments on the airfoil as well as the moment due to the weight of the model acting down. F_A is the force exerted by the idle gear on the window to maintain equilibrium. F_B is the force exerted by the idle gear A on the driving gear B. The driving gear has to exert that amount of force to maintain equilibrium. Based on the equilibrium of the idle gear, F_B and F_A should be of equal magnitude. Therefore, torque that has to be provided by the driving motor to maintain equilibrium is:

$$T_{REQUIRED} = F_B \times r_B = F_A \times r_B \qquad \textbf{Eqn. 9}$$

But F_A can be calculated from M_{NET} as shown below:

$$F_A = \frac{M_{NET}}{R} \qquad \textbf{Eqn. 10}$$

M_{NET} can in turn be calculated from the forces and moments exerted on the model due to the aerodynamic effects and weight distribution of the model. Three cases can be

considered for the determination of the moment that has to be resisted by the driving motor at any time of its operation.

CASE 1: Wind off condition with only dead load

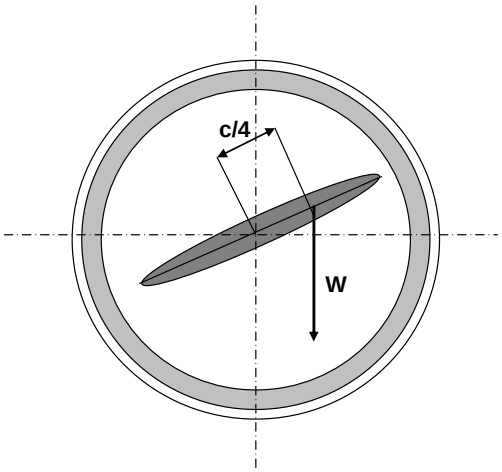

Figure 2-5 Loads on the model in wind off condition

`

This is the case when there is no flow over the model and hence no aerodynamic force or moment is generated. Only a force due to the gravitational weight of the model is exerted on to the rotating window frame. A moment will be created depending on the location of the center of mass of the wing model with respect to the geometric center of the window. An estimate of the weight of a model of a wing that can be tested in the wind tunnel was made based on:

1. The size of the wing model which is limited by consideration of aerodynamic blockage effects;
2. Material that might be used to fabricate the model.

The chord of the airfoil should not be larger than 0.4h, where h is the height of the test section, so that error in $c_{l,max}$ measurement is avoided [44] . The height of the test section is 0.921 m. Hence, the maximum chord of the airfoil is 0.3683 m. Assuming 19 % thick airfoil, the maximum thickness of the model is calculated to be 0.070 m. And for two-dimensional testing the span of the airfoil is 0.5969 m, slightly less than the width of the test section. Taking $2/3^{rd}$ of the thickness of the airfoil, the volume of the resulting rectangular prism is 681.5 square inches. Assuming that aluminum, which has a density of 2700 kg/m^3, is used to fabricate the model, the weight of the equivalent rectangular prism turns out to be 295 N.

The location of the center of mass is assumed to lie between the mid chord and the quarter chord point of the airfoil. The model is assumed to be held by the load cell at the mid chord of the airfoil. Maximum moment is exerted on the window when the center of gravity is at the quarter chord based on this assumption. Hence, the maximum moment when no aerodynamic forces act on the model is:

$$M_{NET} = -295N \times 0.0921m = -25.32N - m$$

CASE 2: Wind on condition with only aerodynamic loads

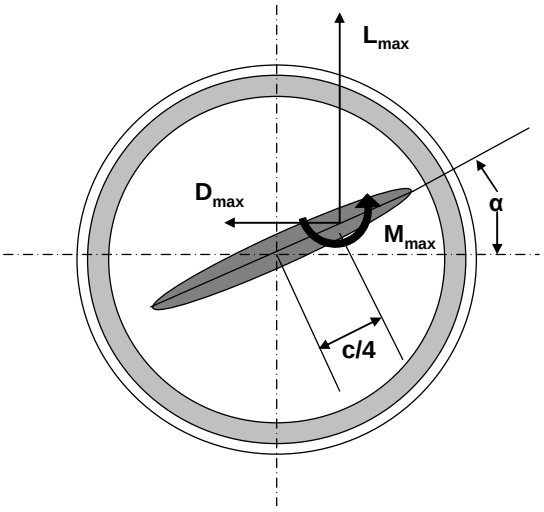

Figure 2-6 Aerodynamic loads acting on the airfoil

In this case the model is assumed to be mass-less and the flow over the model generates aerodynamic force and moments. The model is assumed to be connected to the center of the circular window frame at the mid chord. Due to the flow over the airfoil at the maximum velocity of the wind tunnel, the aerodynamic lift, drag and moment at the quarter chord point, as shown in Figure 2-6, are considered for the calculation of the moment exerted on to the circular rotating window. The total moment on the model, and hence the window is calculated from the equation:

$$M_{NET} = L_{\max}\left(\frac{c}{4}\right)\cos\alpha + D_{\max}\left(\frac{c}{4}\right)\sin\alpha + M_{\max} \qquad \textbf{Eqn. 11}$$

Using the maximum forces shown in Table 6 and assuming that the maximum angle of attack is 23 degree, the net moment turns out to be:

M_{NET} =60.166 *N-m*

CASE 3: Wind on condition with aerodynamic and dead loads

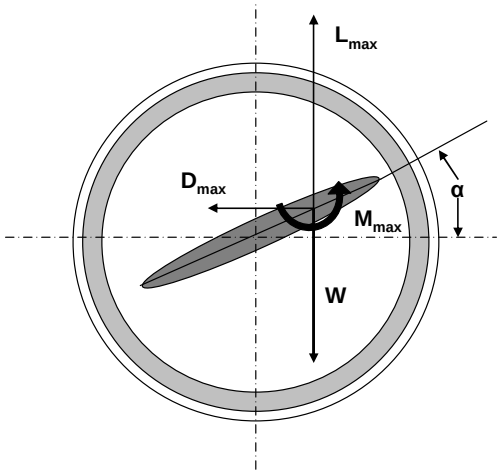

Figure 2-7 Aerodynamic and dead loads

In this case both the aerodynamic loads and the dead load of the model are considered simultaneously. The resultant moment is calculated using the equation:

$$M_{NET} = (L_{\max} - W)\left(\frac{c}{4}\right)\cos\alpha + D_{\max}\left(\frac{c}{4}\right)\sin\alpha + M \qquad \text{Eqn. 12}$$

M_{NET} = 35.1838 *N-m*

The three cases discussed above were assumed to be three extreme cases that could be encountered during any time of the entire wind tunnel testing routine. M_{NET} for the three cases are summarized in Table 9.

CASE 1	-25.32 *N-m*
CASE 2	60.166 *N-m*
CASE 3	35.1838 *N-m*

Table 9: Summary of the net moments in the three cases

It makes logical sense to use CASE 2 to calculate the torque required by the driving motor to resist. F_A is therefore calculated as:

$$F_A = \frac{M_{NET}}{R} = \frac{60.166N - m}{0.5588m} = 107.67N$$

Hence, the torque required by the driving motor can be calculated as:

$$T_{REQUIRED} = F_A \text{ x } r_B = 107.67\ N \text{ x } 0.3048\ m = 0.5202\ N\text{-}m$$

where r_B is the diameter of the driving gear B. Allowing 30 % extra torque due to the assumptions made in the analysis, the total torque becomes:

$$T_{REQUIRED} = 0.676\ N\text{-}m$$

Based on the torque estimated with the above calculations, KSL091T1Y stepper motor shown in Figure 2-8, manufactured by Slo-Syn AC synchronous motors, was selected to drive the mechanism. The specification of the motor is shown in Figure 2-9.

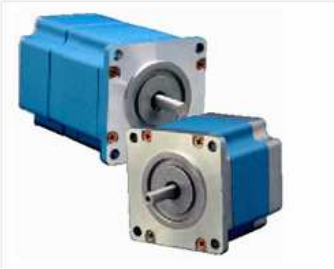

Figure 2-8 Stepper motor selected for the force balance mechanism

KSL091T1Y

PERFORMANCE	
Speed RPM:	72
Frequency Hz:	60
Input Voltage VAC:	120
Minimum Torque N-m (oz-in.):	1.69 (240)
Max Rigidly Attached Load Inertia kg-m^2 (oz-in.-s^2):	0.0012 (0.17)

WINDING	
Number of Phases:	1
Line Current A RMS/Ø:	0.5
Wiring Diagram:	R/C

DIMENSIONS

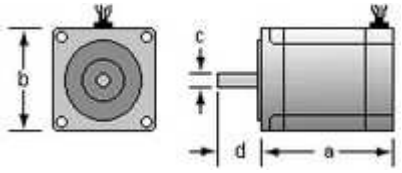

Motor Diameter (b) mm (in.):	85.5 (3.37)
Motor Length (a) mm (in.):	65.1 (2.57)
Shaft Diameter (c) mm (in.):	9.53 (0.375)
Shaft Length (d) mm (in.):	30.2 (1.19)

R-C PHASE SHIFT	
Resistor Part Number:	201052-037
Resistor Value ohms:	300
Resistor Power Rating watts:	50
Capacitor Part Number:	201053-076
Capacitor Value µf:	5
Capacitor Voltage Rating VAC:	240

Figure 2-9 Specifications of the driving stepper motor

2.3 Fabrication and Integration

In this section, the design and fabrication of the components supporting the load cell are discussed. Also discussed is the integration of the various components into a working system.

2.3.1 Load Cell

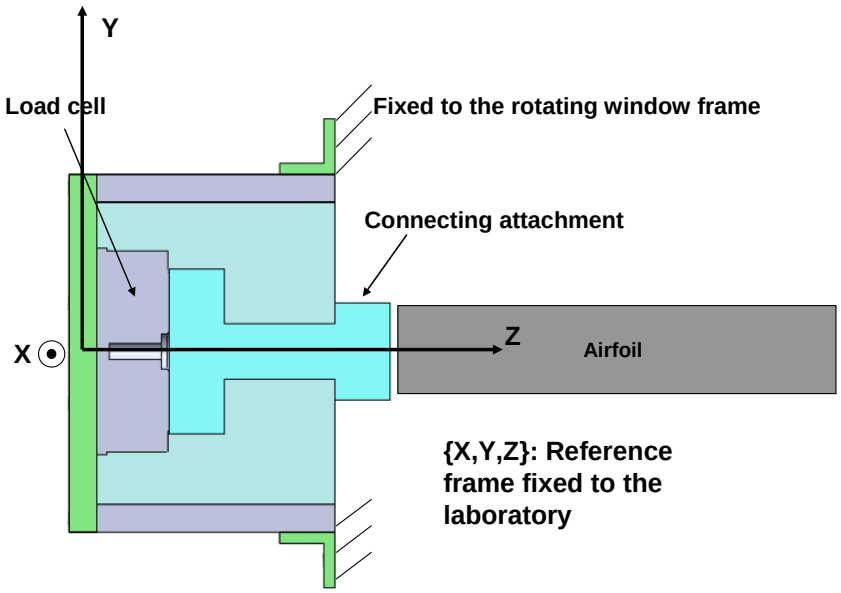

Figure 2-10 Schematic the load cell as it supports the airfoil model

The load cell is attached to a housing which is screwed to the rotating window which can be considered to have fixed to it a reference frame that is fixed with respect to the laboratory. The load cell is connected to the side of the airfoil via a connecting

attachment. The attachment and the window are isolated from each other so that all the loads on the airfoil are transmitted via it to the load cell. The load cell that is attached to the near side of the test section is shown in Figure 2-10.

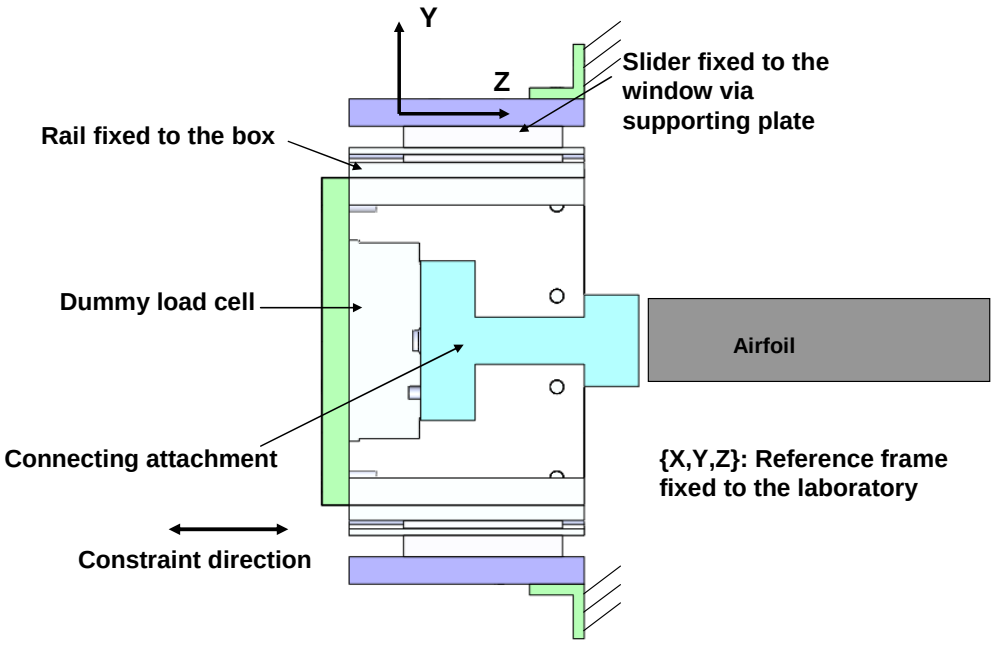

Figure 2-11 Load cell attachment on the far side of the test section

The load cell on the far side of the test section is shown in Figure 2-11. One consideration that dictated the design of far side load cell attachment was that the airfoil may expand due to the rise in temperature owing to viscous dissipation in the wind tunnel. For this reason, the load cell on the far side was provided with a pair of sliders that are constrained to move along the direction that is parallel to the span of the airfoil or width of the test section.

2.3.2 Integration of the Mechanism

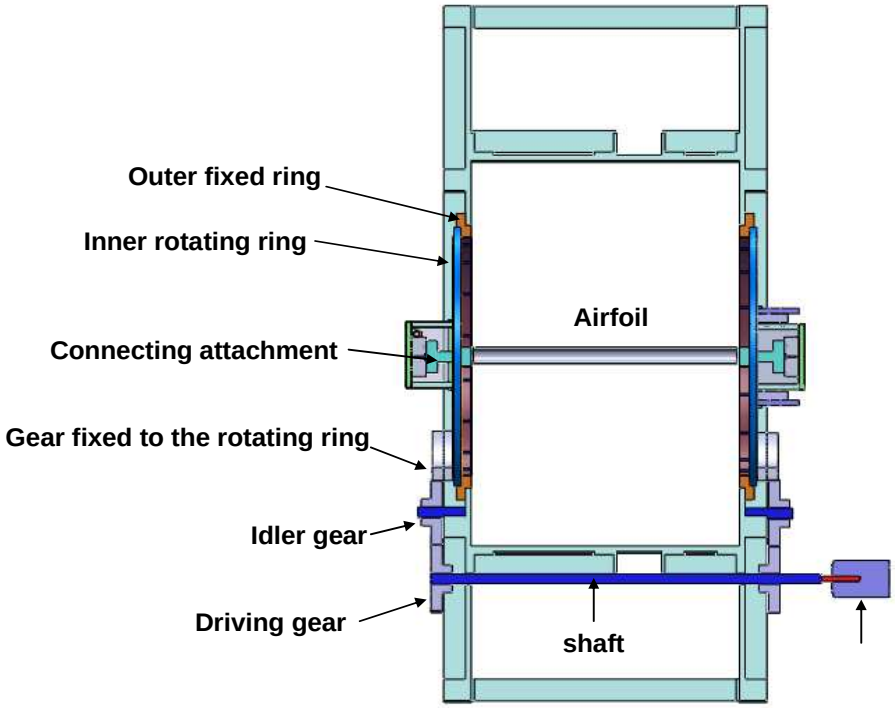

Figure 2-12 Cross section of the mechanism for airfoil testing

As discussed at the beginning of section 2.2, the mechanism consists of an outer ring which is fixed to the wall of the wind tunnel as shown in Figure 2-12. An inner rotating ring has a plexi-glass attached to it in such a way that once mounted in place at the side of the test section, the inner surface of this assembly is flush with the inner wall of the test section. The box that supports the load cell at the near side of the test section is fixed to the plexi-glass with a hole at the center of the plexi-glass for the end of the

connecting attachment to access the side of the airfoil where it is held. The inner rotating ring has a gear segment attached to it which mates with the idler gear. The two driving gears at the sides, which mate with the idlers, are connected by a common shaft that runs underneath the test section. The same shaft is coupled to the stepper motor that is fixed via an attachment to the side of the wind tunnel. The photographs of the completed mechanism are shown in Figure 2-13 and Figure 2-14.

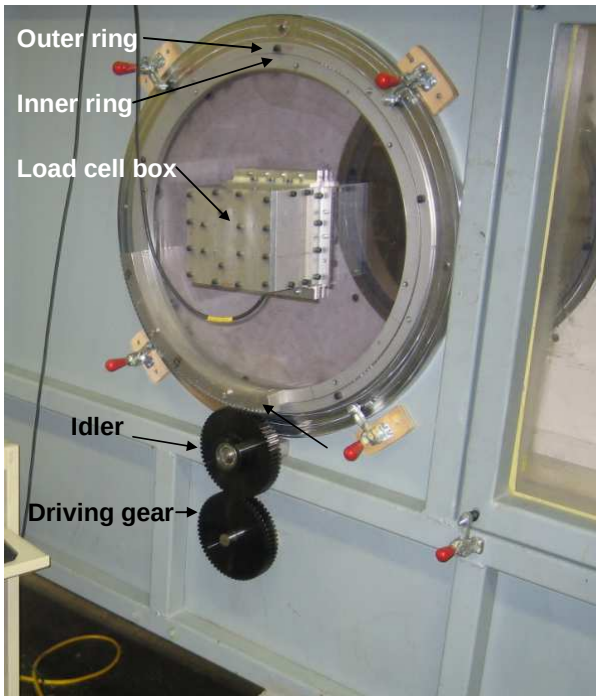

Figure 2-13 View of the mechanism at the near side of the test section

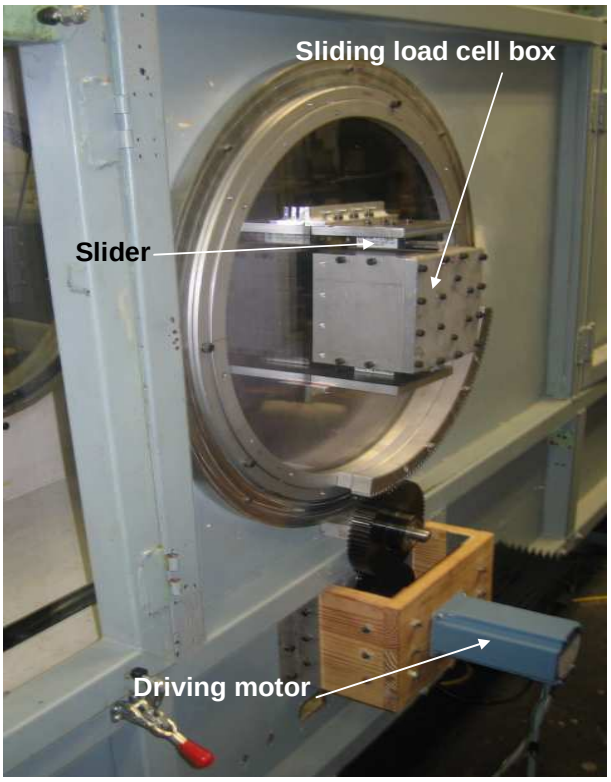

Figure 2-14 View of the mechanism at the far side of the test section

2.4 Validation of the Force Balance

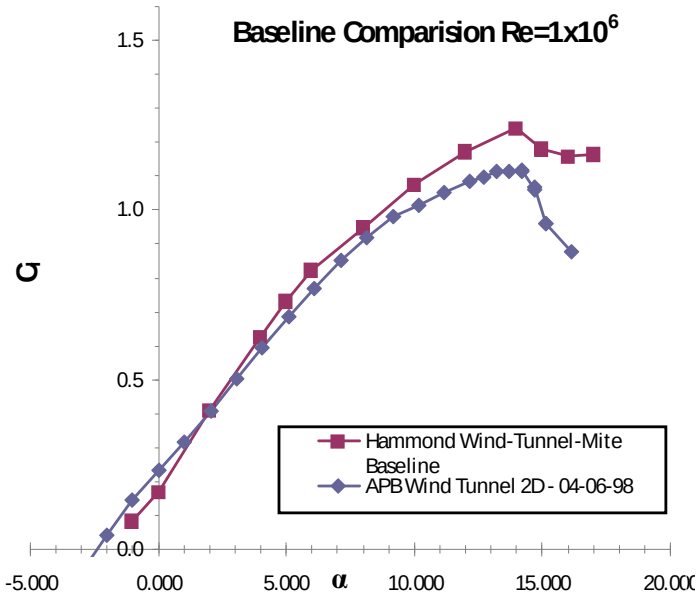

Figure 2-15 Comparison of lift coefficients of S903 airfoil obtained at the two wind tunnels

Once the physical integration of the mechanism was completed the force balance was used to measure the aerodynamic characteristics of S903 airfoil for validation of the load cell. Comparison of the measured forces on this airfoil was made against the data collected at the Penn State Low-Speed, Low-Turbulence wind tunnel which is known to have excellent flow quality and can be compared to what are regarded as the world's best two-dimensional airfoil wind tunnels. Comparison of lift coefficients of the S903 airfoil tested at the two wind tunnels is shown in Figure 2-15.

In the figures, Hammond Wind Tunnel is the one for which the force balance mechanism that is being discussed in this chapter was designed. APB Wind Tunnel is the one to which it is being compared for validation of the force balance and is the same as the Penn State Low-Speed, Low-Turbulence wind tunnel. It should be observed in Figure 2-15 that lift coefficients obtained with the designed force balance agree well with those obtained using surface pressure taps at the Penn State Low-Speed Low-Turbulence wind tunnel, except around the stall region. This discrepancy at the region of maximum lift is due to the chord of S903 airfoil model, which is large compared to the test section of the Hammond wind tunnel. At high angles of attack, the effective free stream velocities can be higher due to solid blockage.

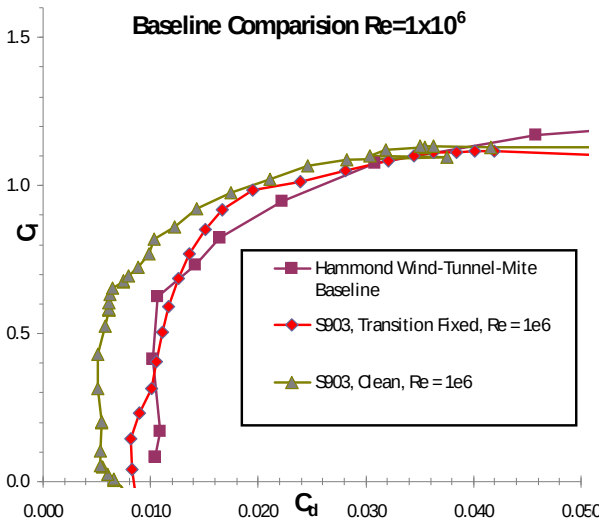

Figure 2-16 Comparison of drag coefficients of S903 airfoil obtained at the two wind tunnels

Comparison of drag coefficients is shown in Figure 2-16. Drag coefficients measured at the two wind tunnels differ in a way that needs an explanation. When transition is not fixed on the model that is tested at the Penn State Low-Speed Low-Turbulence wind tunnel (APB in the figures), drag measured at the Hammond wind tunnel is much larger. The two sets of data agree with each other when transition is fixed on the model tested at the APB. Part of the reason for the discrepancy may be resolved if the flow qualities in the two wind tunnels are compared. The turbulence intensity for the Hammond wind tunnel is 0.3% at 140 ft/s, which is seven times greater than that for APB tunnel. Hence, due to the higher free stream turbulence level in the Hammond wind tunnel, the transition free drag coefficient is higher than the transition fixed drag measured at the APB tunnel.

The designed force balance is considered to provide fairly satisfactory measurement of the aerodynamic forces. The discrepancies observed in the validation are related to flow quality and due to the limitation imposed by the size of the test section with respect to the model. In experiments where one is interested in the change in the aerodynamic coefficients and not as much on the absolute values of those coefficients, the designed force balance mechanism is suitable. One of the drawbacks of this mechanism is that it cannot strictly measure two-dimensional characteristics. This is due to the fact that a force balance is involved. A small gap must be allowed between either sides of the airfoil and the wind tunnel walls so that the entire load is transferred through the connecting attachment to the load cell.

Chapter 3

DESIGN OF DYNAMIC ROUGHNESS ACTUATOR TO SUPPORT FUNDAMENTAL RESEARCH

An important pre-requisite for a successful investigation of the effect of dynamic roughness actuation on airfoil performance is the design of an actuator that meets the following basic requirements:

1. The actuator should fulfill the desired function of dynamically moving a part of the physical surface of the airfoil;
2. It should be able to function properly at frequencies that are dictated by the relevant non dimensional frequency requirements;
3. The actuator should be such that the frequency of actuation can be varied continuously;
4. There should also be a quick and easy way to change the amplitude of excitation;
5. The actuator should be robust.

3.1 Proposed Design

In order to achieve the aforementioned basic requirements a purely mechanical actuator with a spring and cam arrangement shown in Figure 3-1 was proposed. The three dimensional view of the system is shown in

Figure 3-2. The system consists of a block with the dynamic roughness pins attached to it. The block is constrained to the cover plate

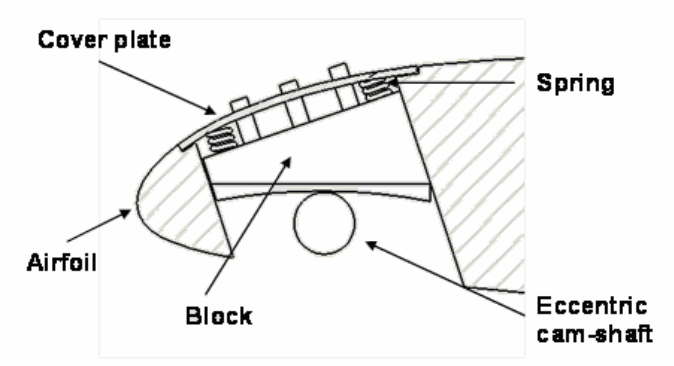

Figure 3-1 Proposed dynamic roughness actuator design

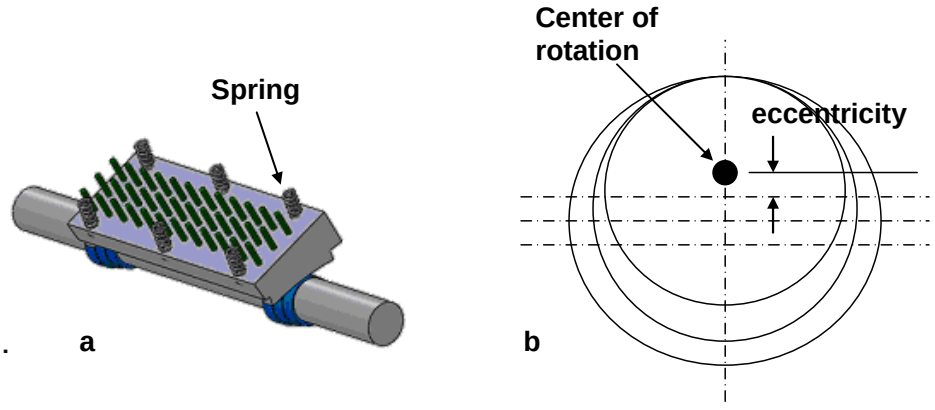

Figure 3-2 a) 3D view of the proposed actuator design, b) Eccentric cams for control of amplitude

via mechanical springs. The bottom surface of the block has legs that rest on the eccentric cams on the drive shaft, which is rotated by an electric motor. Cams with several eccentricities would be designed on the shaft side by side that would allow for variable amplitude of excitation. Changing the speed of the motor would change the frequency of excitation. Sliding the shaft along its axis would engage the cams with different eccentricities with the mating legs of the block, hence changing the amplitude of excitation. If the mechanical parts are integrated and constrained properly the system was to be quite robust at least to support fundamental research at this early phase of investigation. The only requirement to satisfy then was that it should be able to function properly at the frequencies of excitation that are dictated by the F+ requirements at both the leading and trailing edges of the airfoil. The next few sections will discuss the dynamic analysis of the proposed actuator design subject to this condition.

3.2 Dynamic Analysis of the Proposed Actuator Design

The principal concern in the analysis was to make sure that the spring force is sufficient to keep the joint between the block and the cams closed at all times for the range of cam shaft rotation rates, i.e. about 400 Hz, besides making sure that the natural frequency of the system is kept as high as possible. The mechanism can be represented by the simplified model shown in Figure 3-3(a). The free body diagram of the simplified model is shown in Figure 3-3(b).

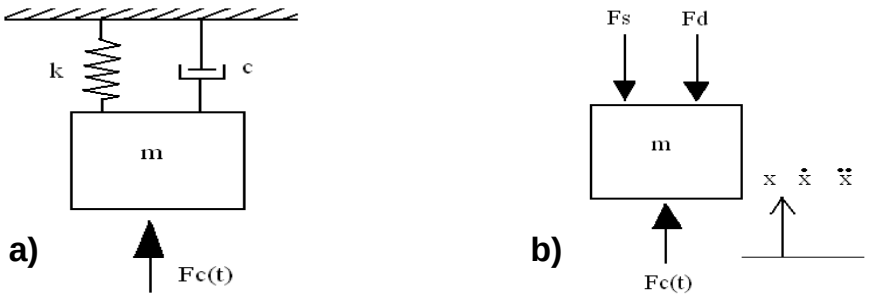

Figure 3-3 a) Analytical model of the actuator, b) Free body diagram

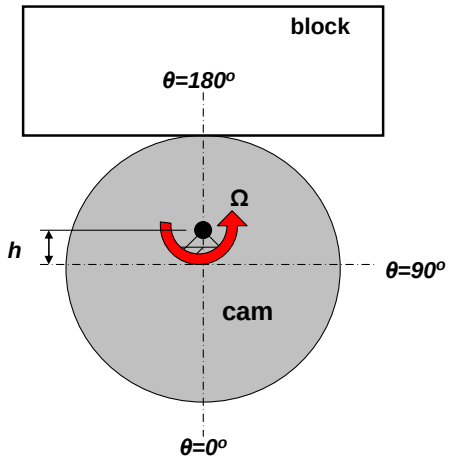

Figure 3-4 Schematic showing the orientation angle of the cam

The governing equation of motion of the system is:

$$F_C(t) = m\ddot{x} + c\dot{x} + k(x + x_o) \qquad \textbf{Eqn. 13}$$

The direction of the cam force as shown in Figure 3-3(b) is assumed to be positive.

The goal of the analysis is to make sure that the cam force is always greater than zero. Negative cam force practically means that the cam is no longer in contact with the block. The problem then for a given cam with a given angular velocity of the shaft is to choose the constants m, c and k so that the force $F_C(t)$ is always greater than zero.

The examination of the governing equation of motion shows that the spring force term is always positive. The damping and inertia terms can be positive as well as negative. Since acceleration is numerically greater than velocity, the inertia term is much greater than the damping term. Hence, negative acceleration is the main cause for the $F_C(t)$ to be negative. The most negative acceleration in the cam shaft rotation cycle is of primary interest in the analysis. Figure 3-5 describes the procedures of the analysis used.

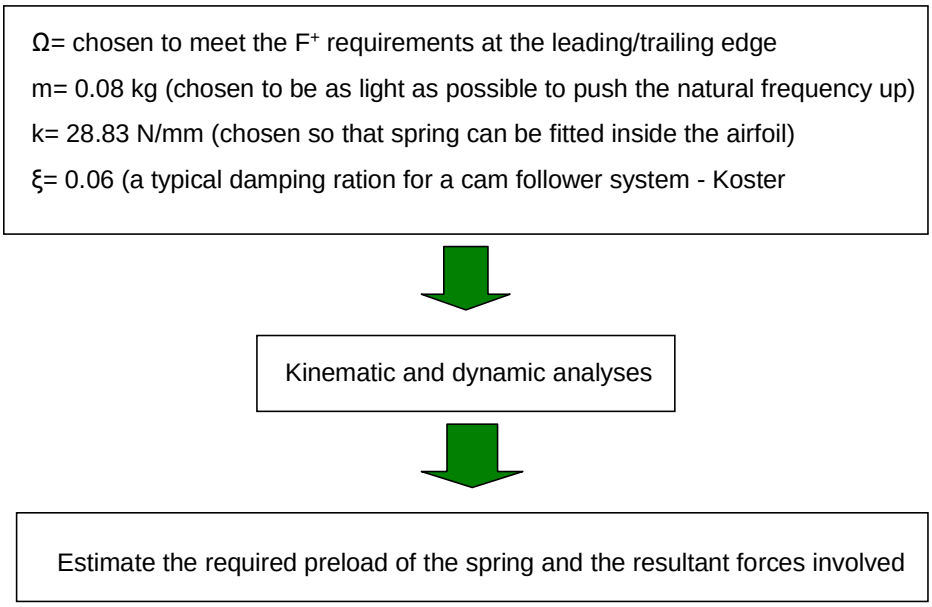

Figure 3-5 Analytical procedure

To offset the large negative value of the acceleration term, the spring force term should be sufficiently large. To do that, either the spring constant should be large or preload distance should be large. Larger the value of the spring constant, larger will be its physical dimension. The size of the spring is however constrained by the availability of space in the airfoil in which it is to be implemented. With the prescribed spring constant preload can be adjusted so that the spring force term as a whole can still be increased. In order to solve the governing equation of motion displacement, velocity and acceleration are required for the entire cycle of rotation. The cam profile chosen for this analysis is modeled by simple harmonic motion whose displacement, velocity and acceleration function are:

$$x = \left(\frac{h}{2}\right)\left[1 - \cos\left(\pi\frac{\theta}{\beta}\right)\right] \qquad \textbf{Eqn. 14}$$

$$\dot{x} = \frac{\pi}{\beta}\frac{h}{2}\sin\left(\pi\frac{\theta}{\beta}\right).\Omega \qquad \textbf{Eqn. 15}$$

$$\ddot{x} = \left(\frac{\pi}{\beta}\right)^2\frac{h}{2}\cos\left(\pi\frac{\theta}{\beta}\right).\Omega^2 \qquad \textbf{Eqn. 16}$$

h = Total rise of the block (m)

θ = Cam shaft rotational angle

Ω = Angular velocity of cam shaft (rad/s)

β = Angle of rise

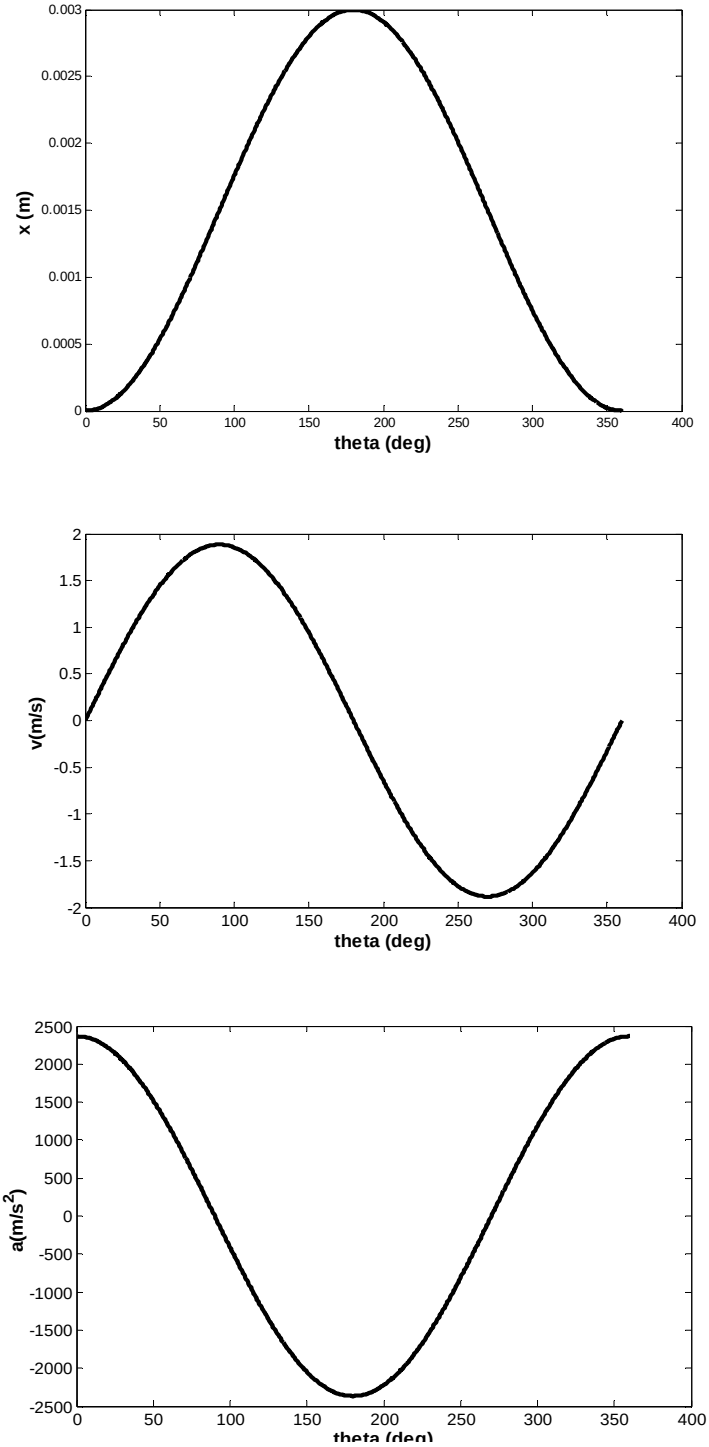

Figure 3-6 SVA plots for the cam SHM at Ω = 1256 rad/s, h=3mm (Leading edge actuator)

The SVA diagram of the model is shown in Figure 3-6 where $\theta = 0^o$ corresponds to the lowest position of the block and $\theta = 180^o$ corresponds to the highest position of the block. The values of displacement, velocity and acceleration at the most-negative-acceleration location are:

s	0.003 *m*
v	0 *m/s*
a	-2366.3 m/s^2

After the corresponding values of displacement, velocity and acceleration at the most negative acceleration point are found, cam forcing function F_C is calculated for various values of preload distances and plotted in Figure 3-7. Observe that for a given *m, k, c, s, v* and *a*, the preload should be larger than about 5 mm so that the cam does not lose contact with the block.

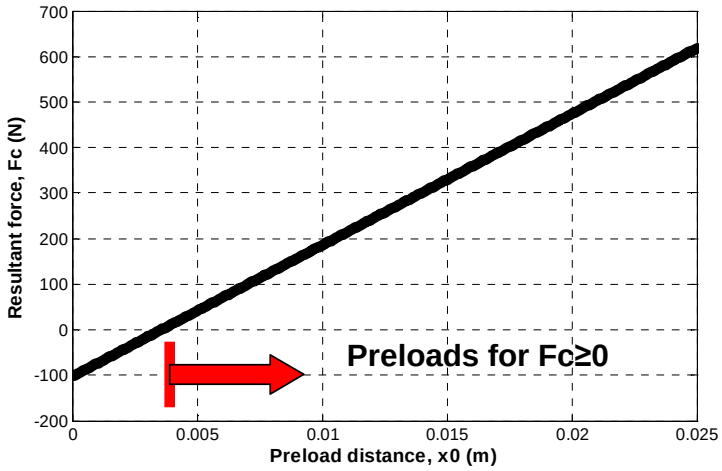

Figure 3-7 Resultant force as a function of preloads at the most negative acceleration point

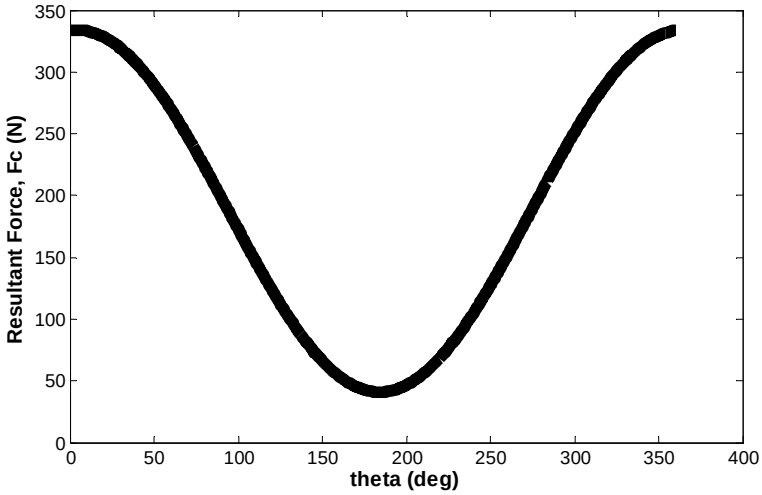

Figure 3-8 Resultant force as a function of angular orientation of the cam

If preload is chosen to be 5 mm, to see how much force is transmitted to the skin via the block, cam force is plotted with respect to the cam orientation for the selected preload in Figure 3-8. The maximum force transmitted is 333 N. This is a fairly large force. Also, the resultant torque on the cam would require a fairly big driving motor, which is not desirable.

The results presented thus far are for cam shaft rotational speed of 1256 rad/s, which corresponds to a frequency of 200 Hz, calculated based on non-dimensional frequency F^{+}=1.4 and assuming the actuator is close to the leading edge of a 14 inch chord model.

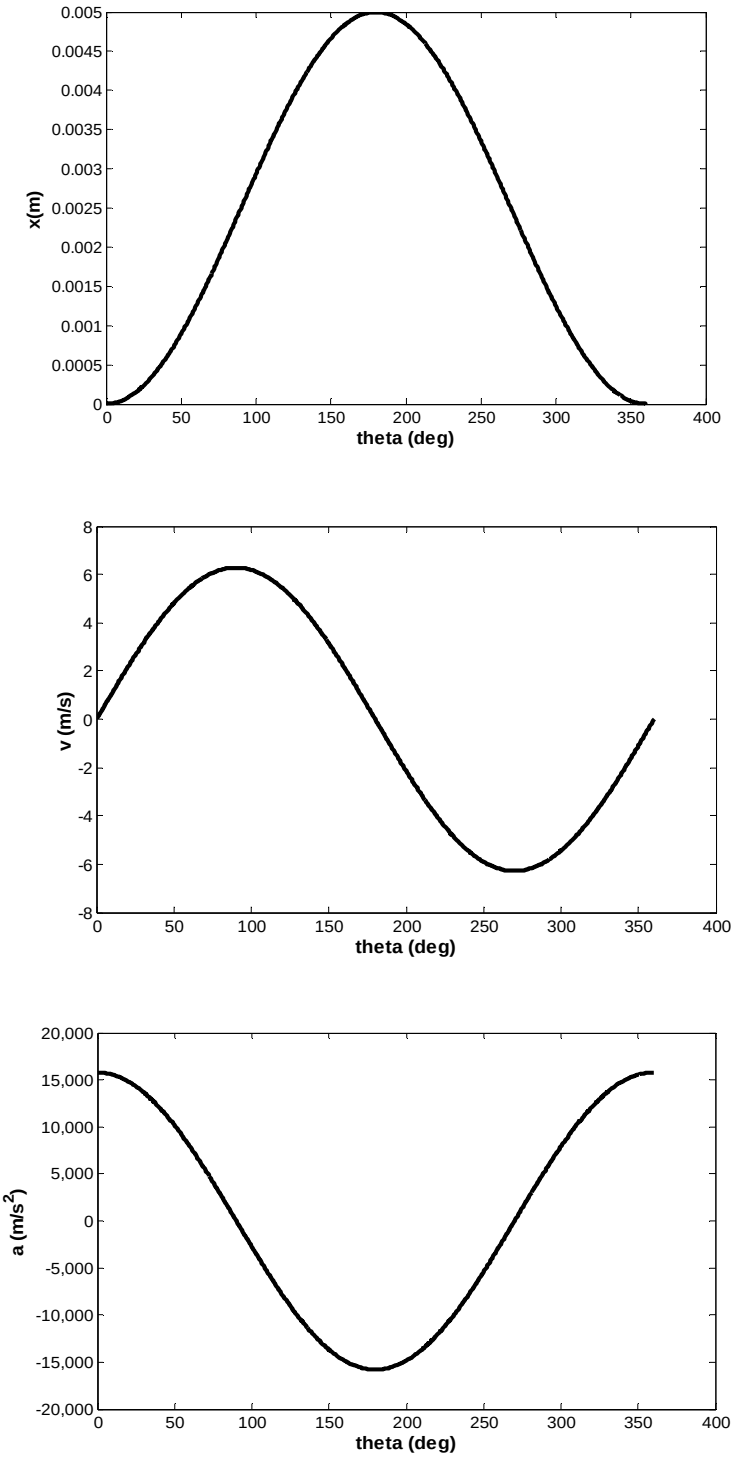

Figure 3-9 SVA diagram for Ω =2513.27 rad/s, h=0.005 m (Trailing edge actuator)

Similar non dimensional frequency condition applied to an actuator located close to the trailing edge requires frequency of about 400 Hz, which corresponds to 2513.27 rad/s at the same free stream velocity. The SVA diagram is shown in Figure 3-9.

The displacement, velocity and acceleration at the most-negative-acceleration point are:

s	0.005*m*
v	0 *m/s*
a	-15791m/s^2

In order to satisfy the condition that the cam and the block don't lose contact at any time of its rotational cycle, the preload should be at least 40mm for the selected mass of the block, spring constant and damping coefficient, as shown in Figure 3-10. This is way too bigger than can be accommodated in the airfoil model. Moreover, the resultant force on the block at this rotational frequency is extremely high.

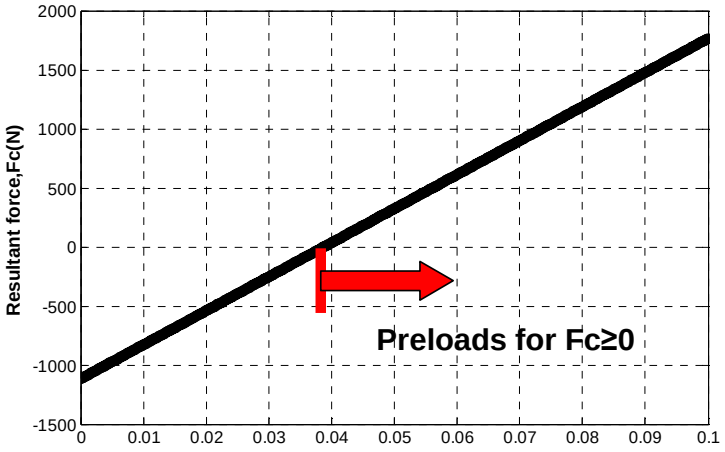

Figure 3-10 Force as a function of preload distance at the most negative acceleration point for Ω =2513.27 rad/s, h=0.005 m

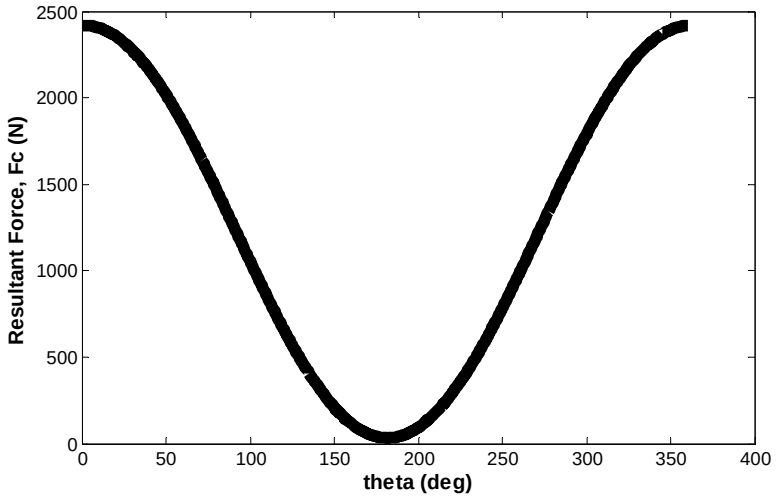

Figure 3-11 Resultant force as function of angular orientation of cam for Ω =2513.27 rad/s, h=0.005 m

The following conclusions are drawn from the dynamic analysis of the simplified actuator model:

1. For an actuator installed at the leading edge of the airfoil, large force and hence large resultant torque is involved.
2. For an actuator installed at the trailing edge of the airfoil, not only a very large force is involved but also the preload distance is larger than can be accommodated given the dimension of the selected spring and the space available in the airfoil model.
3. The proposed actuator mechanism was hence considered to be not practically feasible based on vibration and load considerations and an alternative design had to be conceived.

3.3 Alternative Dynamic Roughness Actuator Design

The performance of an actuator that involves a mechanical spring is limited due to vibration issues. A piezoelectric based actuator with a given boundary condition works only at one frequency, which is its resonance frequency. An alternative actuator design that meets the requirements laid down at the beginning of this chapter was needed. A rotating mechanical actuator was proposed. The concept is shown in Figure 3-12. The mechanism consists of series of cams with one or more bumps on them mounted on a shaft and separated by spacers. The shaft is coupled to an electric motor which rotates it. The airfoil surface has a number of slots for the bumps to protrude as they are rotated.

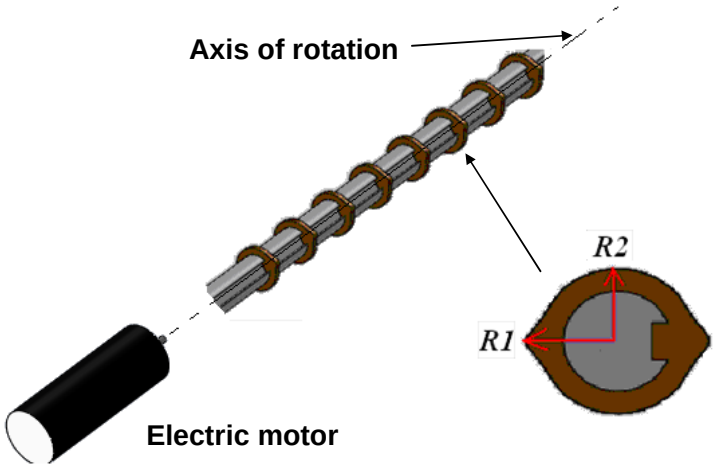

Figure 3-12 Rotating actuator mechanism

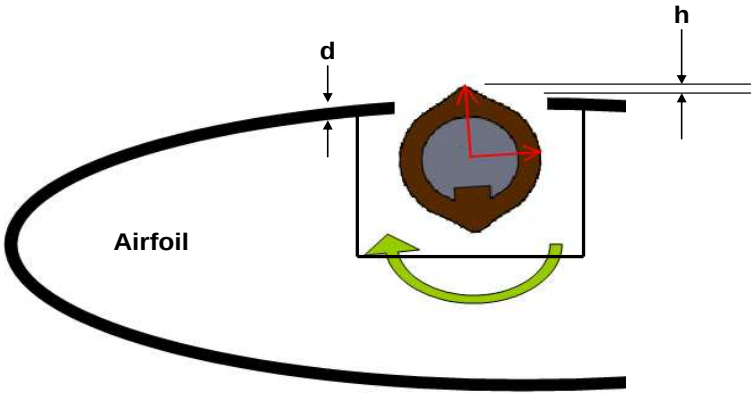

Figure 3-13 Actuator as it is installed in the airfoil

The most notable advantage with this system is that it requires no mechanical spring and hence does not suffer from the drawbacks associated with a reciprocating system involving mechanical springs. Using a motor with Hall sensors that allow for variable speed, the frequency of actuation can be increased or decreased continuously. Moreover, the frequency of actuation is multiplied for a given motor speed depending on the number of bumps on the cams, thus providing much wider frequency bandwidth. The amplitude of excitation is given by $h = (R1-R2)-d$. To change the amplitude of excitation cams of different sizes could be designed and simply replaced.

3.4 Ideal Dynamic Roughness Actuator: Morphing Skin

Dynamic roughness actuator concept discussed in section 3.3, if proven to be effective in improving the airfoil performance, may not be applied directly to the actual system due to existence of open clearances at the side of the rotating cams. An ideal dynamic roughness actuator would be some kind of dynamic morphing skin. The skin itself would be locally deformed in dynamic fashion to form dynamic roughness bumps. There would be no exposed holes or clearances. The power required to activate the dynamic roughness should be low by using small electro-mechanical devices to perturb the surface of the skin. The proposed actuator design in this work should be good to support fundamental research into the effects of dynamic roughness at this stage of the investigation, when we are no where close to thinking about practical implementation in real systems. Once the physics is understood and the benefits of dynamic roughness are established, state-of-the-art actuator design should proceed to come up with a robust actuator that can be applied to a real system.

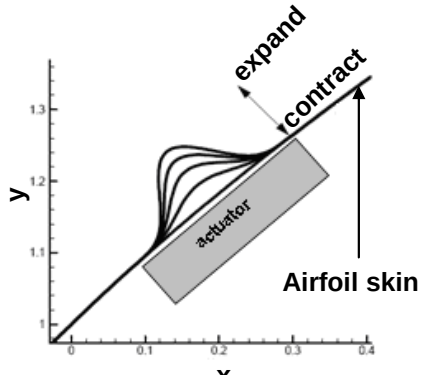

Figure 3-14 Dynamic roughness through flexible skin [39]

Chapter 4

WIND-TUNNEL TESTS OF DYNAMIC ROUGHNESS ON THREE AIRFOILS

In this chapter wind-tunnel tests of dynamic roughness implemented on three different airfoils will be discussed. Since the experiments were not conducted at the same facility, details of the experimental set up and instrumentation will be discussed for each of the experiment in their respective sections. Section 4.1 will discuss an investigation of dynamic roughness applied to an NACA 23012 airfoil. Section 4.2 will look at the tests conducted with dynamic roughness applied to the HTR 1555 airfoil. And lastly in section 4.3, details and observations of the wind-tunnel test on the SM 701 airfoil will be discussed.

4.1 The NACA 23012 Airfoil

In order to perform a parametric study of the effect of dynamic roughness on the boundary-layer, the NACA 23012 was chosen as the test airfoil. This airfoil was chosen because it is used in rotorcraft and the global aim of this project is to improve the aerodynamic performance of rotor airfoils. This section will discuss the airfoil model design and fabrication, actuator placement, experimental set up and results of the tests conducted on NACA23012.

4.1.1 NACA23012 Airfoil Model Design and Fabrication

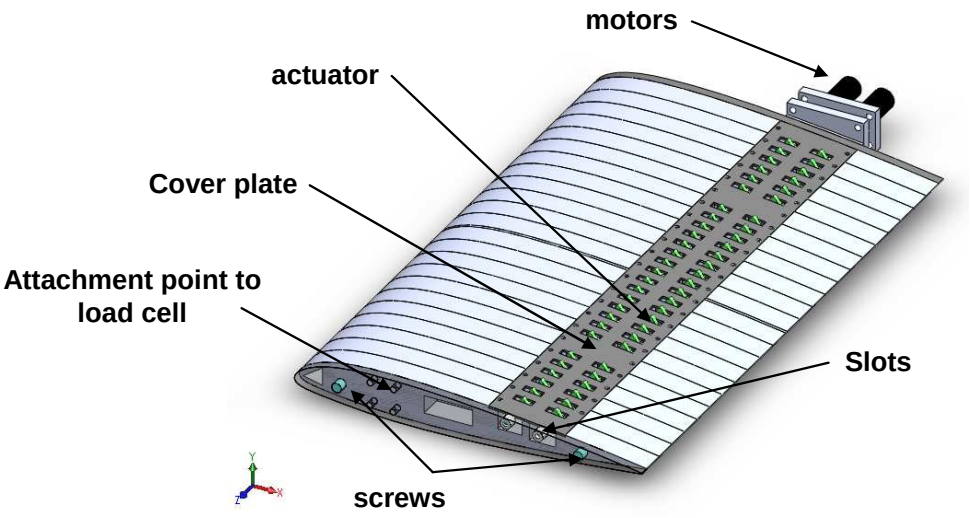

Figure 4-1 NACA23012 airfoil model with dynamic roughness actuator

The airfoil model was fabricated using aluminum. Due to the lack of resource, instead of building the entire model out of solid piece of aluminum, which ensures best finish, the model was built in a number of sections of 1 inch thickness each. These sections were then held together by two screws that span the total span of the model as shown in Figure 4-1. Care was taken to ensure smoothness of the surface once assembled. Slots were cut out to place the actuator.

4.1.2 Location of Excitation

The actuator should be placed as close as possible to separation point on the airfoil for dynamic roughness to be effective. If the goal of the investigation is to improve the maximum lift generated by the airfoil or to delay stall, a good location for the actuator would be little upstream of the separation point at stall for the Reynolds number range that would be tested. Experience with actuator placement on the SM701 airfoil, based on XFOIL predictions of the baseline flow, demonstrated the reliability of this approach. The separation point on NACA23012 airfoil at stall for R_C=1,000,000 was determined using XFOIL and shown in

Figure 4-2.

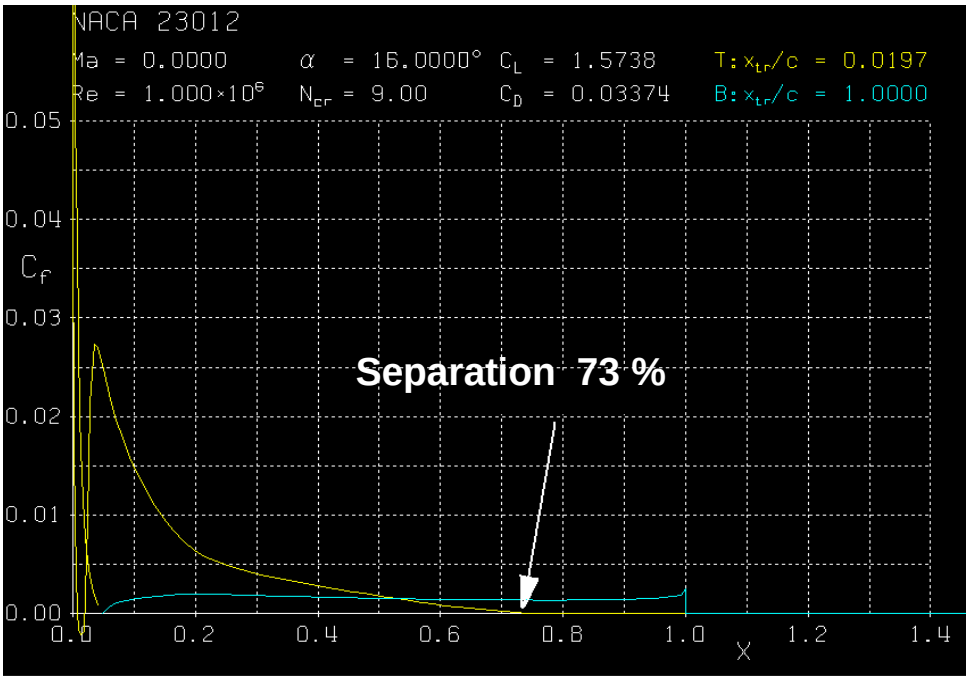

Figure 4-2 Skin friction coefficient plotted against chord wise distance on NACA23012 at stall and at R_C=1,000,000

In

Figure 4-2, the yellow curve is the skin friction coefficient on the upper surface and the blue curve is skin friction coefficient for the lower surface. Theoretically, zero or negative skin friction coefficient implies that the attached boundary layer has left the surface and hence indicates separation. Observation of

Figure 4-2 shows that for the specified Reynolds number at stall, the flow separates at 73 % chord from leading edge. Two rows of dynamic roughness actuators were placed slightly upstream of the expected separation at stall as shown in Figure 4-3.

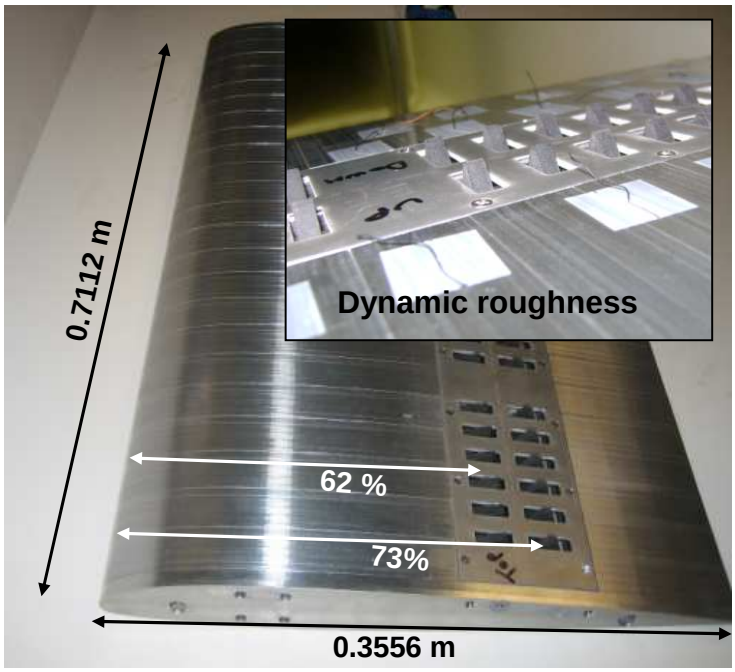

Figure 4-3 Dynamic roughness actuator installed in NACA23012 airfoil

4.1.3 Experimental Set up and Instrumentation

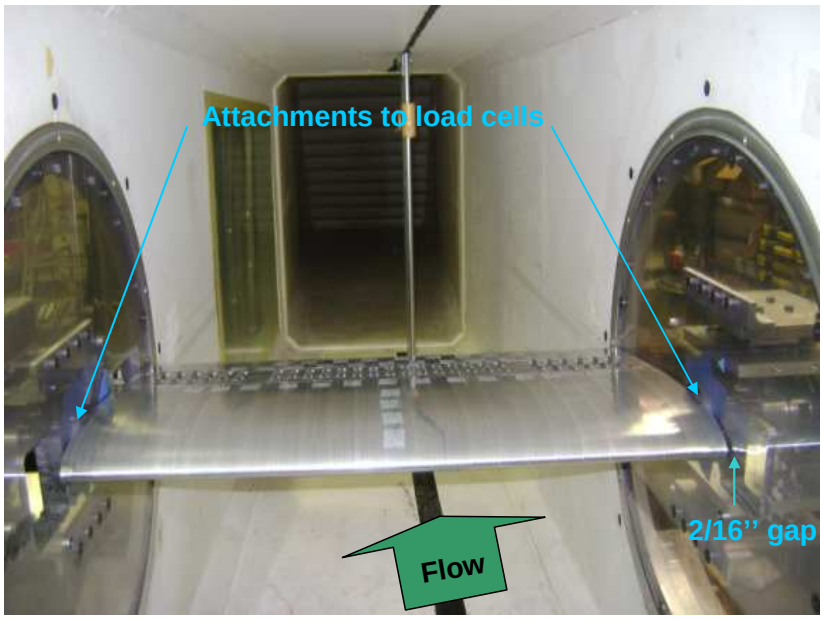

Figure 4-4 NACA23012 with dynamic roughness set up in the wind tunnel for testing

The newly designed force balance mechanism for the Hammond Low-Speed wind tunnel discussed in chapter 3 was used to measure the aerodynamic forces on NACA23012 with dynamic roughness.

4.1.4 Wind-Tunnel Tests

Wind-tunnel tests on NACA 23012 were conducted at three different Reynolds numbers, viz. 300,000, 500,000 and 700,000. First, baseline aerodynamic characteristics were measured. Against these baseline data, measurements with dynamic roughness would be compared to determine the effects of dynamic roughness actuation.

4.1.4.1 Baseline

The baseline lift, drag and pitching moment coefficients at Reynolds number of 300,000, 500,000 and 700,000 were measured and compared with XFOIL and plotted in Figure 4-5, Figure 4-6 and Figure 4-7.

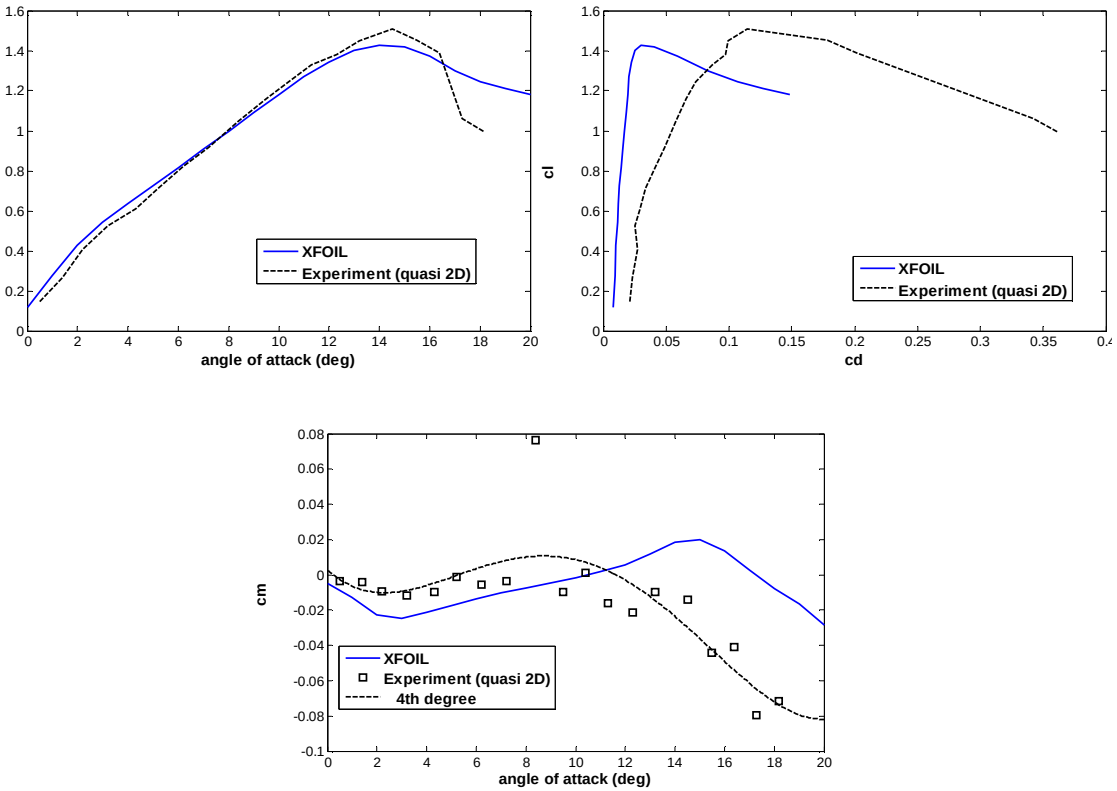

Figure 4-5 Comparison of experimental aerodynamic coefficients with XFOIL at R_C=300,000

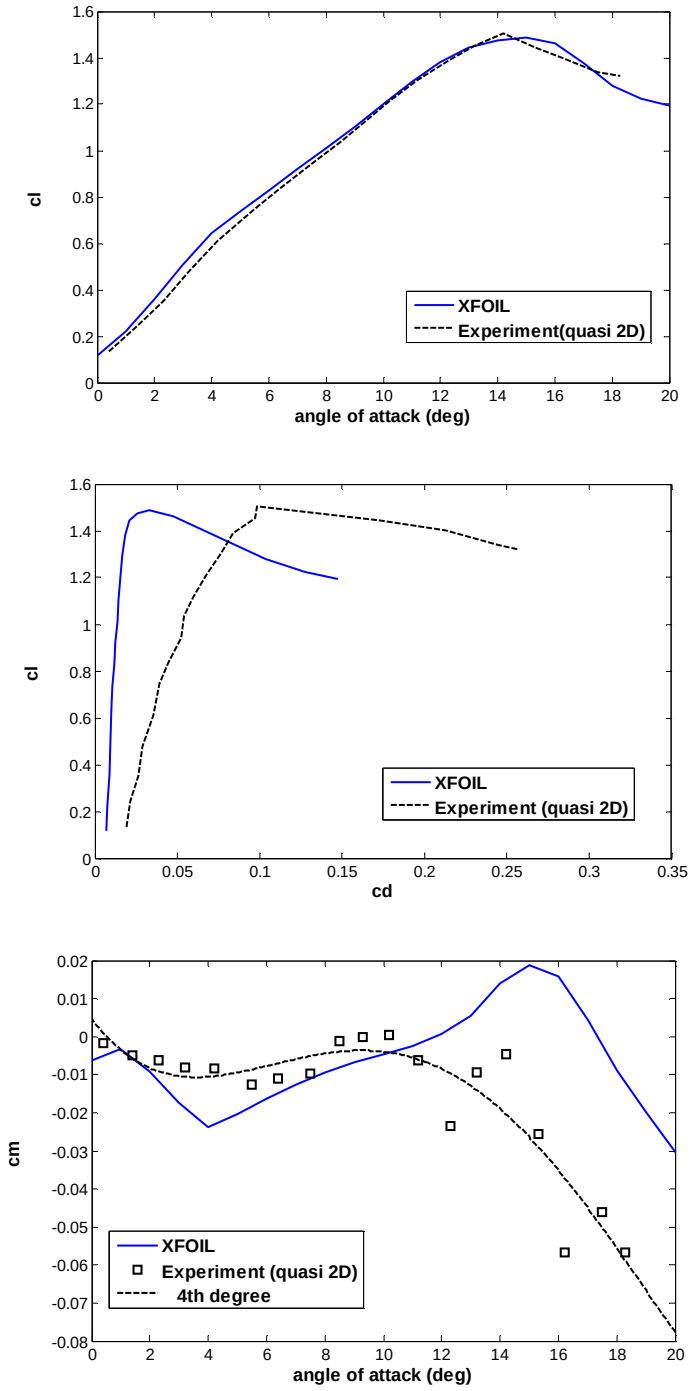

Figure 4-6 Comparison of experimental aerodynamic coefficients with XFOIL at R_C=500,000

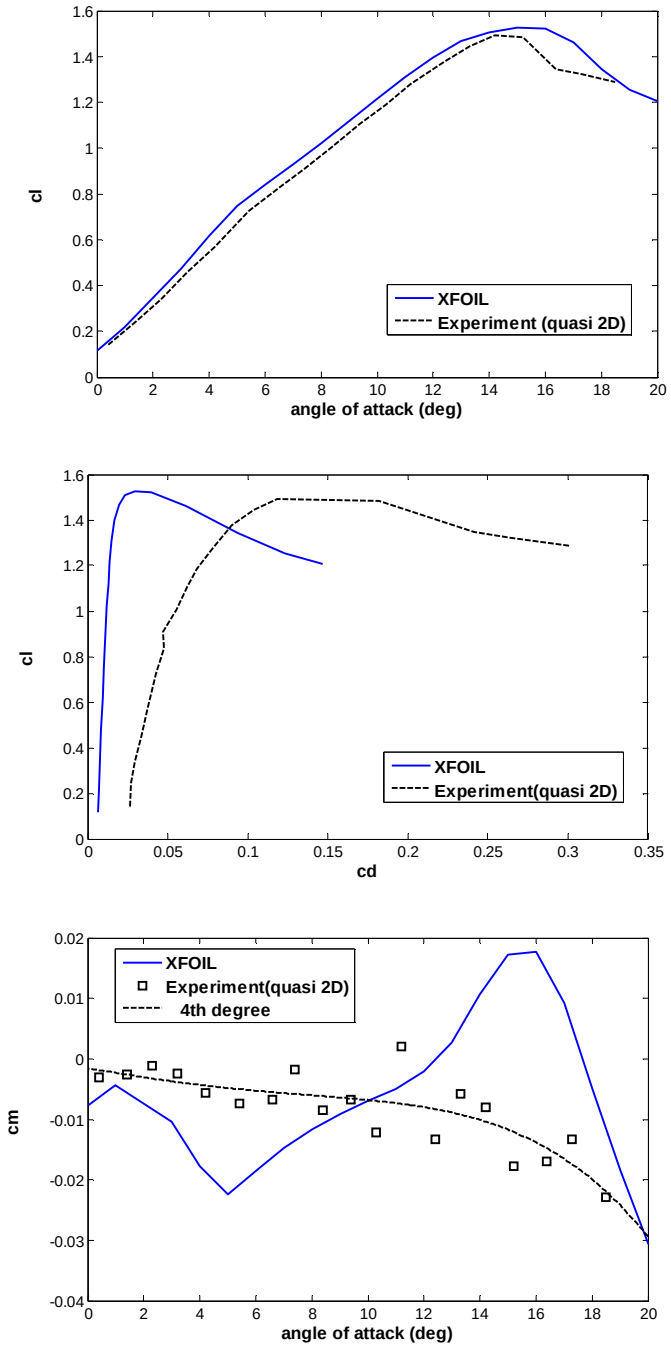

Figure 4-7 Comparison of experimental aerodynamic coefficients with XFOIL at R_C=700,000

Observe that for all three Reynolds numbers tested, experimental lift coefficients correlate well with XFOIL prediction. Also experimental pitching moment coefficients show similar trend to the ones predicted by XFOIL. The drag coefficients, however, are over measured in the wind tunnel. The measured drag coefficients are higher than one the ones predicted by XFOIL for two reasons. Firstly, XFOIL prediction is for a strictly two dimensional airfoil. The model used for this experiment is strictly speaking not two dimensional, but quasi-two dimensional because a small gap-in the present case 2/16 of an inch on both sides must be allowed between the airfoil and the walls of the test section so that the entire aerodynamic loads on the airfoil is transferred only to the load cells. Moreover, the wall boundary layer thickness at the model location is measured to be two inches, which introduces significant three-dimensional effect. The second reason for the higher drag in the experiments is due to the free-stream flow quality in the test section. The turbulence intensity of the wind tunnel at the maximum velocity is 0.45%, which is quite high. Higher the free stream turbulence, higher the skin-friction drag for the same chord Reynolds number. Still other factors, not identified, may be contributing to higher drag coefficients.

Even though the experimental baseline drag measurements do not agree with the XFOIL predictions, they can still be used to compare against any increment or decrement due to actuation of a flow control device. The relative increment or decrement of aerodynamic coefficients should still shed light on the effectiveness of a flow control device.

4.1.4.2 Effect of Dynamic Roughness Actuation on NACA 23012 Airfoil

Tufts attached on the upper surface of the airfoil provided a quick idea about the behavior of the boundary layer. Three different amplitudes of dynamic roughness, viz. 20%, 50% and 75% of the local boundary layer thickness, were tested. Frequency sweeps were performed with each of these amplitudes. However, no flow attachment, as indicated by the tufts, due to actuation was observed and hence no improvement in aerodynamic performance. Further observation of the baseline flow led to the hypothesis that it might be due to the stall characteristic specific to NACA23012.

The separation point at stall was found out through experiment, and confirmed with two dimensional XFOIL result. This point is located at approximately 75% of chord from the leading edge. The dynamic roughness actuator was installed so that excitation could be introduced slightly upstream of separation point corresponding to stall. It was observed that a 0.5 degrees increment in angle of attack above stall caused the separation to move very rapidly to about 18% chord from the leading edge, as shown in Figure 4-8, suggesting a very strong adverse pressure gradient. The separation point then moves gradually upstream with further increase in angle of attack. This rapid separation movement inhibits the dynamic roughness from affecting the separation behavior of the flow, as the separation point quickly moves upstream of the actuator location. This behavior of the rapid movement of separation point was observed to be similar for all three Reynolds number tested, although Figure 4-8 is only for R_C=500,000.

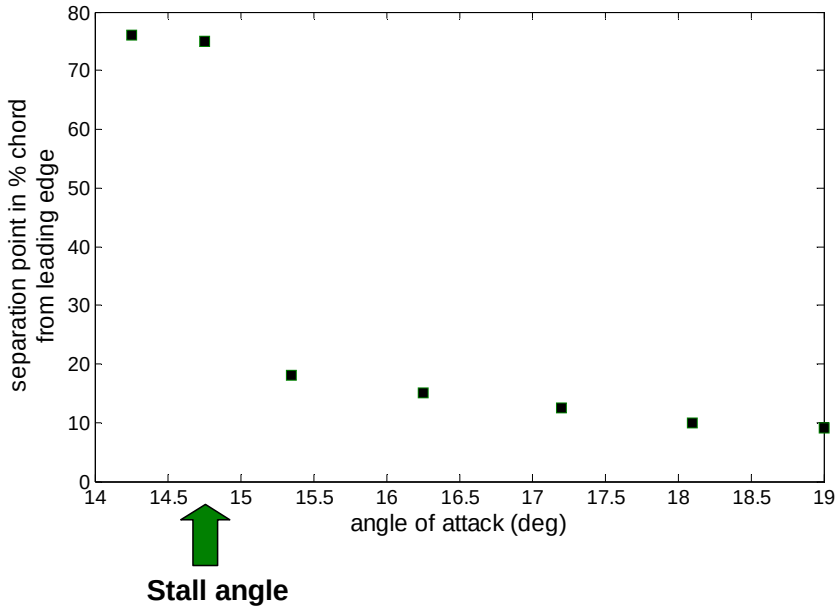

Figure 4-8 Movement of separation point with angle of attack at R_C=500,000

Oil flow visualization was performed to observe the behavior of the boundary layer in greater detail. The slots for the actuators were covered with an aluminum tape. Aviation engine oil was diluted with machine cutting fluid and applied on the upper surface of the airfoil. Ultraviolet light, in which the oil becomes luminescent, was used to observe the behavior of the oil. Observation of oil agreed with Figure 4-8, which was based on the observation of the tufts. Moreover, oil flow visualization provided very clear picture of the flow detail as shown in Figure 4-9, where one can see laminar separation bubble near the leading edge, followed by turbulent separation.

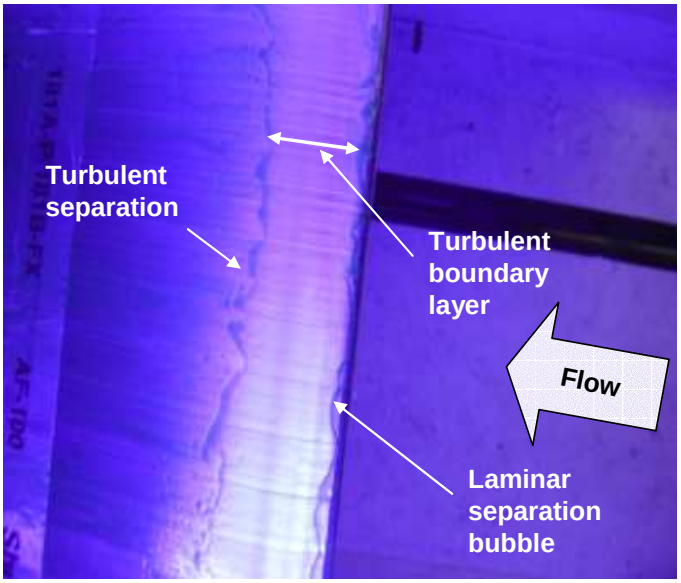

Figure 4-9 Oil flow visualization on NACA23012 at R_C=635,000 and α= 16 degrees

4.1.4.3 Corrective Experiment on NACA23012 Airfoil

Trailing-edge dynamic roughness failed to result in any positive improvement in performance on NACA23012. The reason for this was hypothesized to be due to the stalling characteristic of this airfoil, in which the separation point moves rapidly forward with increasing angles of attack as stall is approached. This is a consequence of the existence of a very strong adverse pressure gradient at stall. This behavior is documented, for example, in the work of Leishman [41]. For an increment of 0.5 degrees beyond the stall angle of attack, the separation point moves rapidly to about 18% chord. Thereafter, further increase in angle of attack caused only gradual movement of separation upstream. It was decide to move the actuator towards the leading edge where the separation

behavior was not as abrupt. The actuators were placed at 13% chord. As mentioned, the separation point moves gradually with increases in angle of attack once the separation point has already jumped from the mid chord region to near 18% chord. A second reason to select this location is based on the work by Kim et al. [31], where synthetic jet actuation was placed at 12% chord on this same airfoil. The author's results showed through CFD analysis that this dramatically decreased the extent of wake and improved post stall performance. The reconfigured airfoil-actuator model is shown in Figure 4-10.

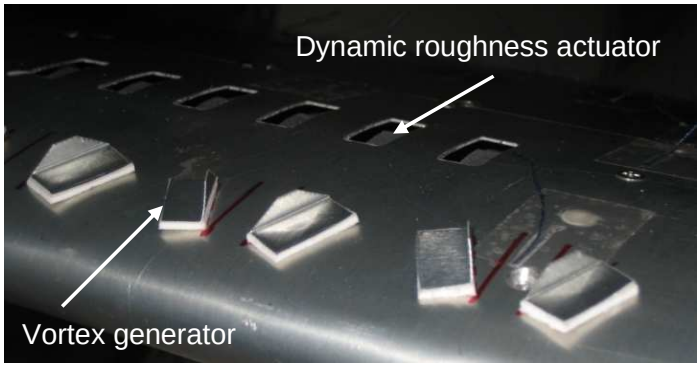

Figure 4-10 Static vortex generators and dynamic roughness actuators

Unexpectedly, tests on this reconfigured model showed that now instead of the separation point moving rapidly to 18% chord, it moved to 10% chord. This could be because the airfoil profile of the model varied slightly upon implementation of the dynamic roughness actuation. Even a small deviation in profile can change the pressure distribution over the airfoil.

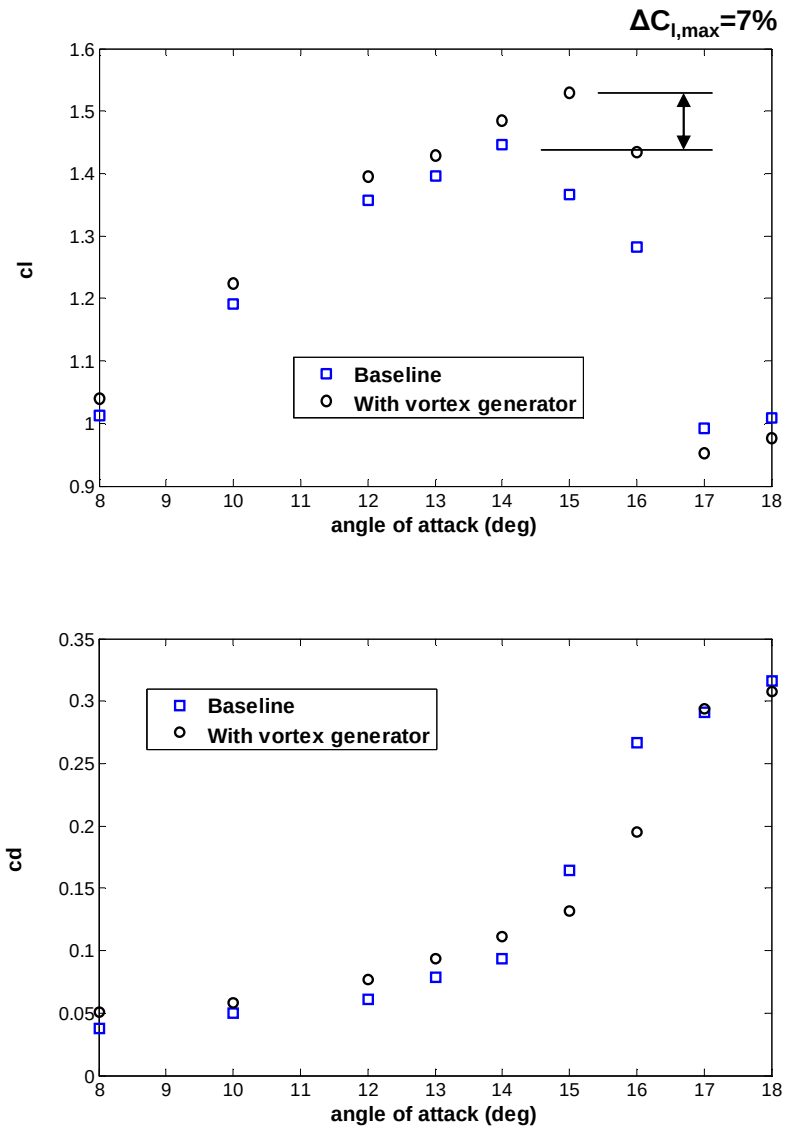

Figure 4-11 Lift and drag vs. angle of attack with vortex generators

To determine that the new location of the actuator was placed behind the separation point (and therefore not providing positive effects in the aerodynamic performance of the airfoil), static vortex generators were installed at the location of the dynamic roughness (18%) as well as at 8% chord, slightly upstream of where the

separation point was experimentally located. This is shown in Figure 4-10, where both the vortex generators and dynamic roughness are seen. The case where the static vortex generators are co-located with the dynamic roughness actuation did not result in any positive improvement in performance, which makes sense since they are now in the separated region. The case where the vortex generators are installed at 8% chord increased $c_{l,max}$ by 7%. It also increased drag at low angles of attack and decreased it at higher angles of attack, which expected given how static vortex generators work. It must be mentioned, however, that the vortex generators are not optimized to their best configuration. The measured aerodynamic characteristics are shown in Figure 4-11.

It was concluded that the airfoil being used, i.e. the NACA 23012, may not be ideal for the demonstration of dynamic roughness flow control and that an airfoil with a separation behavior such that the separation point moves gradually with angle of attack should be used. This was also motivated by the fact that the airfoil used for the preliminary experiments that motivated the current investigation (the SM701), had a stalling behavior where the separation point moved gradually upstream along the chord with increases in angle of attack. Moreover, based on some of the other past work done at Penn State involving Gurney flaps and other devices, it was found that a particular flow control technique may or may not work depending on the type of the airfoil.

4.2 The HTR 1555 Airfoil

The HTR1555 airfoil, originally designed for rotorcraft application [42], was found to be a good candidate for the testing of dynamic roughness. It satisfies the requirement of having a stalling behavior where separation point moves gradually upstream with angle of attack. In addition, a model of this airfoil with pressure taps was already available for immediate use. This allowed access to the Penn State Low-Speed, Low Turbulence Wind Tunnel, a facility having excellent flow quality and is well qualified for aerodynamic research.

4.2.1 The HTR 1555 Airfoil and its Modification

The HTR 1555 airfoil is 18.1% thick and was designed for rotorcraft applications. Its coordinates are available from the US Army etc. The reason to select this airfoil is that it has a stalling behavior where the separation point moves gradually with increasing angles of attack. The shape of this airfoil is shown in Figure 4-12.

The wind-tunnel model is fabricated from solid aluminum. The model has a chord of 21 inches, a span of 42 inches, and is pivoted at $x/c = 0.52$. It has sixty pressure orifices, thirty on the upper surface and thirty on the lower surface. The orifices are staggered when seen from the top to avoid interference from upstream orifices on those downstream.

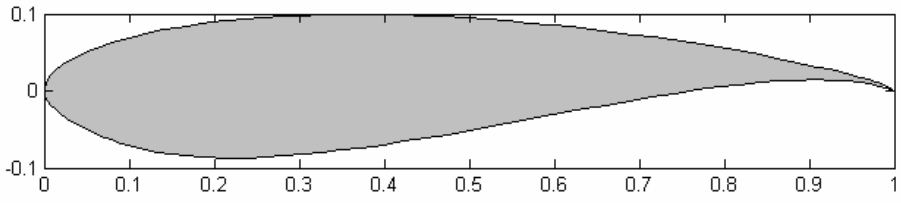

Figure 4-12 HTR 1555 airfoil profile

4.2.2 Location of Excitation

Based on baseline pressure distributions, shown in Appendix, for this airfoil around the stall region and availability of space in the airfoil, it was decided to install the dynamic roughness actuator at 55% chord from the leading edge as shown in Figure 4-13. This required cutting a slot in the airfoil for the installation of the actuator. There are channels in the airfoil for the tubes that connect to the surface pressure taps and absolute care to not damage these connections had to be taken. Before cutting the slots on the airfoil, a detailed map of the internal channels was needed, which was not available, since the pressure taps were done by hand by a third party and not documented. In order to see the channels the airfoil was taken to the radiology department at the university hospital and X-ray photographs of it taken, as shown in Figure 4-14.

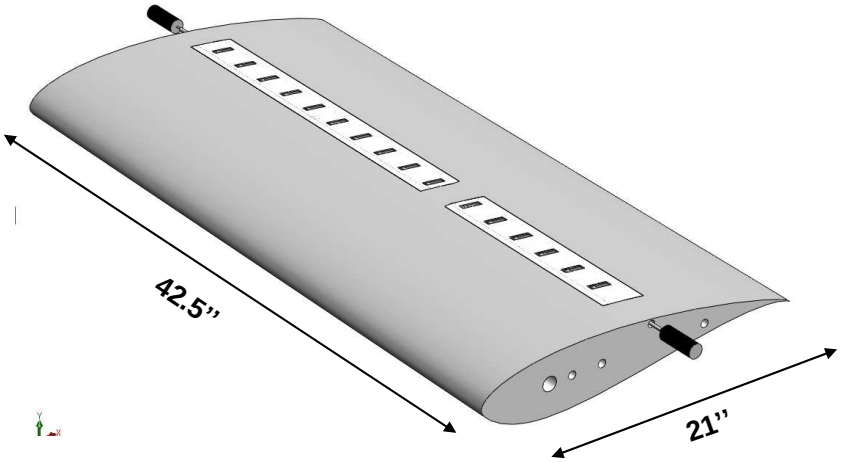

Figure 4-13 The HTR 1555 airfoil with the actuator

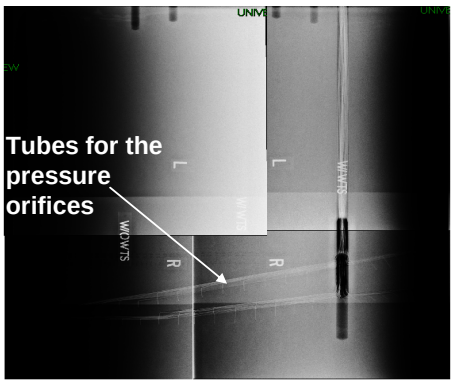

Figure 4-14 X-ray photograph of HTR1555 model to find out the internal channels

Based on the knowledge of the internal channels seen from the X-ray photograph of the model, slots were cut out for the actuator, making sure that the pressure taps were not damaged. Slots were cut out on both sides of the pressure taps. Figure 4-13 shows the

Solid Works model of the actuator-airfoil assembly and Figure 4-16 shows the actual finished model. The actuation is based on rotating cams that protrude on the top surface of the airfoil. The amplitude of the protrusion, the protrusion frequency and the shapes of the cams was varied to investigate best configurations to control the flow over the airfoil.

4.2.3 Experimental Set-Up and Instrumentation

The Penn State Low-Speed, Low-Turbulence wind tunnel was used for the tests on HTR1555 airfoil. This wind tunnel is a closed return type with the turbulence intensity of 0.045% at 220 ft/s. The test section is rectangular and is 58 inches wide and 40 inches high. This facility is considered to be one of the best low turbulence wind tunnels in the world. The detailed schematic of the tunnel is shown in Figure 4-15.

The forces and moment on the airfoil were calculated form the measurement of pressure distributions on the airfoil through the surface pressure taps and wake survey. The model is shown mounted in the tunnel in Figure 4-16. The wake probe which is a pitot-static tube, is located 13 inches, 62% chord distance behind the trailing edge of the airfoil

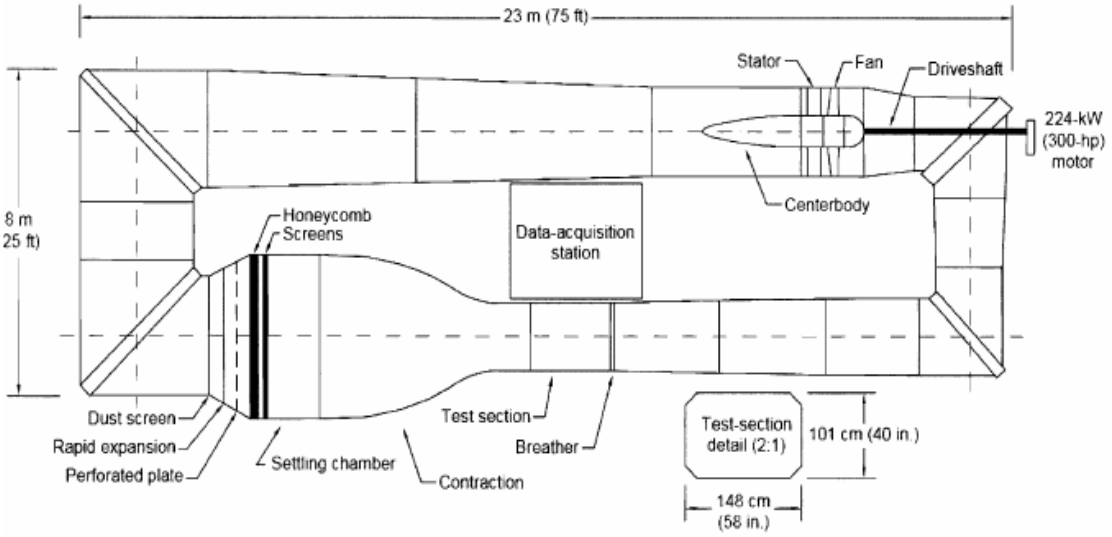

Figure 4-15 Subsonic low turbulence wind tunnel used for the HTR1555 dynamic roughness experiments

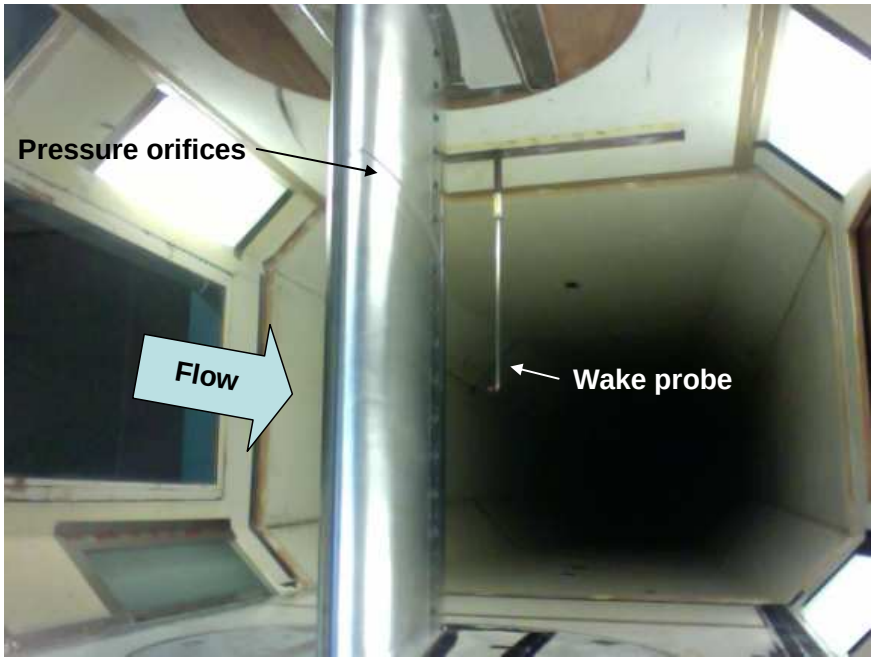

Figure 4-16 Surface pressure orifices and wake probe

4.2.4 Discussion of the Wind Tunnel Test Results

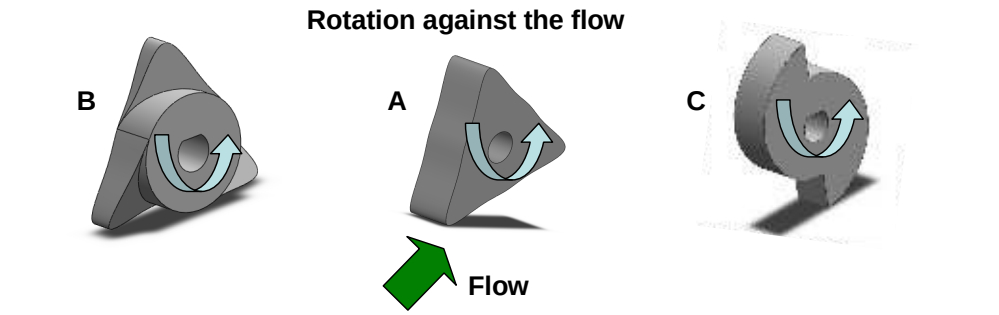

Figure 4-17 Three different dynamic roughness cam shapes tested

In this test, three different shapes of dynamic roughness cams were tested. Dynamic roughness may be thought of as a vortex generator, but perhaps a more efficient one compared to static vortex generators in the sense that it may require lower amplitude. Three cam shapes were designed as shown in Figure 4-17. The ideas behind the choice of cam shapes are explained below.

The cams can be rotated along or against the flow depending on how they are mounted on the shaft. Cam B, when rotated against the flow, acts like a side ways ramp and generates stream-wise vortices. Cam C is based on the work by Viet et al. [25] and is supposed to generate span wise vortices. Two different amplitudes were tested, viz. ~δ= 6 mm (local boundary layer thickness at the actuator) and δ/2. Reduced frequencies that were tested are F^{+}=0.5, 1, 1.5, 2 and 3.

Comparison of the directions of cam rotation showed that the rotation of the cam against the flow was more effective than the rotation along the flow. In all the experiments discussed here, the cams were rotated against the flow.

Baseline tests were performed with the slots for dynamic roughness protrusion covered and un-covered. Negligible differences in the aerodynamic coefficients were observed between the two cases. Hence, when the cams are flush with the surface of the airfoil, the airfoil with the slots uncovered was taken as the baseline for comparison with the dynamic roughness actuation.

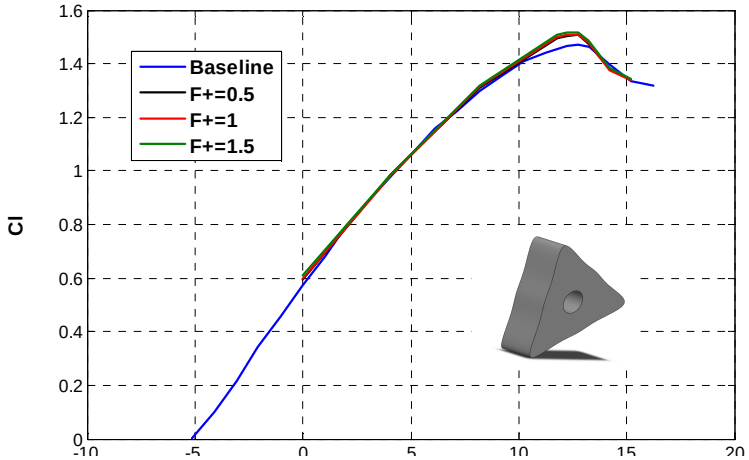

Figure 4-18 Comparison of baseline lift with Cam A for three different frequencies, R_C=1,000,000

Comparison of lift coefficients between the baseline and actuation of cam A is shown in Figure 4-18. No significant gain in lift was observed at the lower angles of attack while a slight increase in drag was observed. Actuation of dynamic roughness increased $c_{l,max}$, but the increase is not significant. It was also observed that increasing the frequency increased $\Delta c_{l,max.}$ F^+=1.5 resulted in the highest gain in lift. At this frequency $c_{l,max}$ increased by 3.4% over the baseline. From the curvature of the lift curve around the stall region it seems that actuation did hold separation for some time. The stall angle of attack was not increased at any of the reduced frequencies tested. c_d is higher at the lower c_l but is lower at higher angles of attack or closer to stall as shown in Figure 4-19.

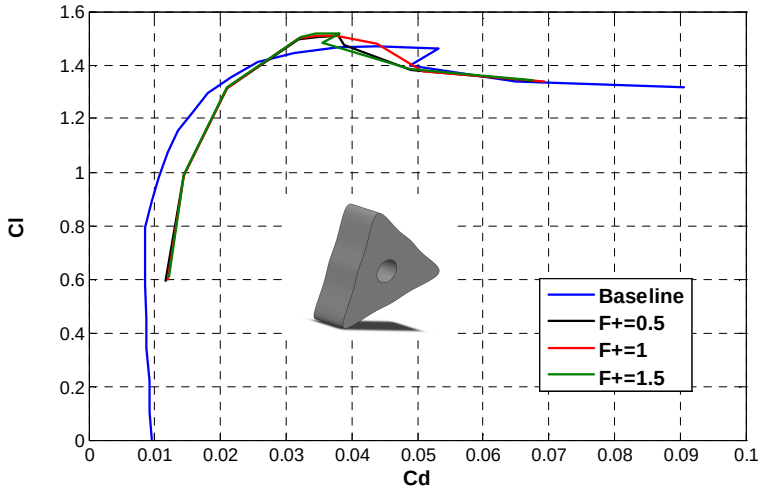

Figure 4-19 Comparison of baseline drag with Cam A with frequencies R_C=1,000,000

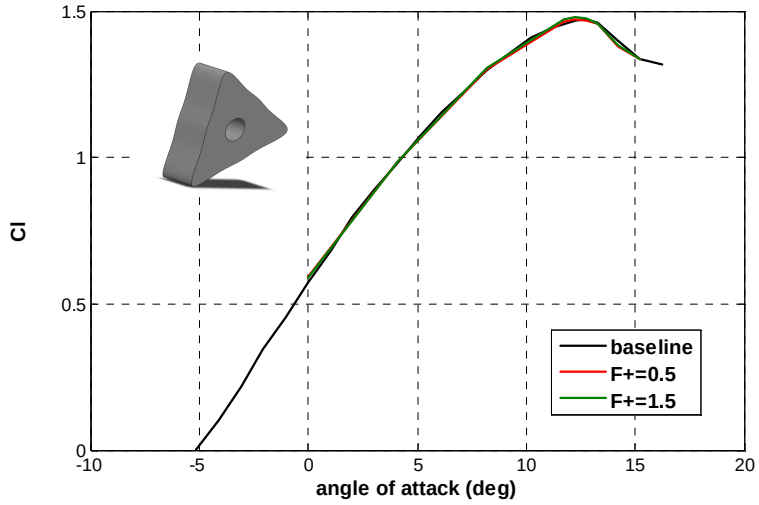

Figure 4-20 Comparison of baseline with cam A (lower amplitude) for different reduced frequencies tested, R_C=1,000,000

Figure 4-20 shows a similar plot for cam A with amplitude δ/2. This amplitude is half as much as the one shown in Figure 4-18. There was only a slight increase in $c_{l,max}$ compared with the higher amplitude cam of the same shape. This increase is so small as

to be barely noticeable in the plot. It was also observed that $c_{l,max}$ improved with increase in reduced frequency, although the increase is again negligible.

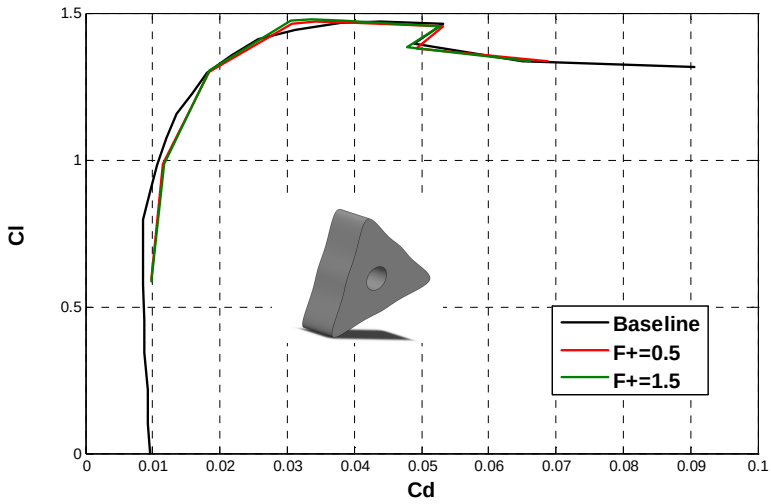

Figure 4-21 Comparison of baseline drag with cam shape A (lower amplitude), R_C =1,000,000

Drag followed more or less the same trend as for the higher amplitude cam but the reduction at higher angles of attack is relatively less. Based on the observations with regard to the amplitude of excitation with cam A, it was concluded that higher amplitude cams are more effective than the lower amplitude cams as far as enhancing $C_{l,max}$ is concerned.

The effect of amplitude and frequency in enhancing $c_{l,max}$ based on cam A is shown in Figure 4-22. $\Delta c_{l,max}$ improved with frequency of actuation for the frequencies that were tested irrespective of the amplitudes of excitation. Moreover, for the same frequency of excitation, higher amplitude cam resulted in higher gain in $c_{l,max.}$ This

reasoning facilitated the elimination of tests with the other two lower amplitude cam shapes B and C in order to reduce wind tunnel hours.

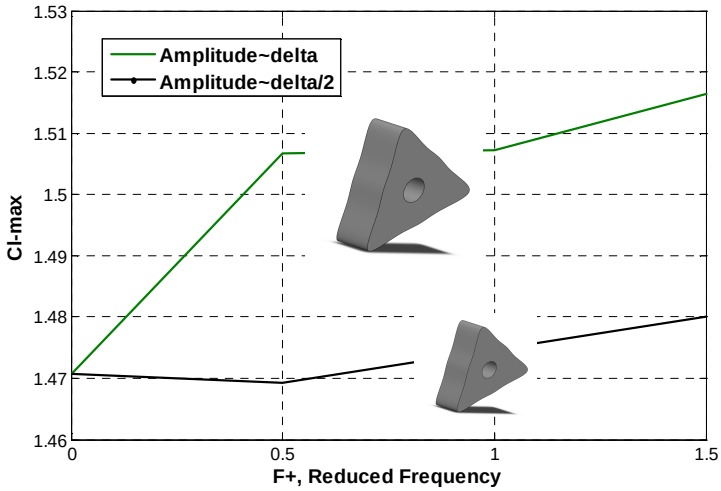

Figure 4-22 Effect of amplitudes based on cam shape A results, R_C =1,000,000

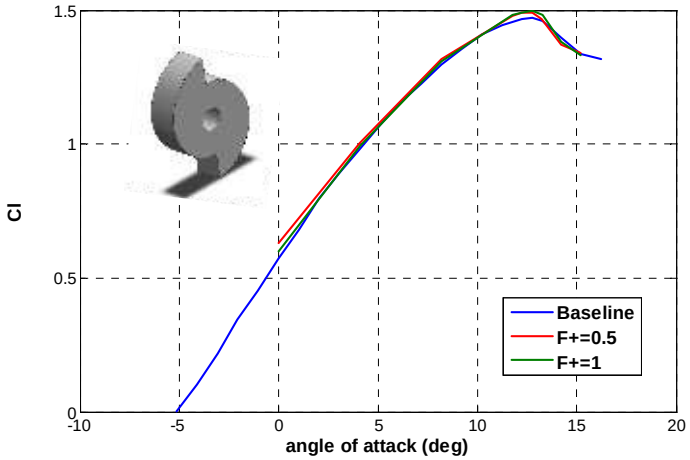

Figure 4-23 Comparison of baseline lift with cam shape C, R_C =1,000,000

To investigate the difference the shape of the dynamic roughness cams make in improving the aerodynamic performance, cam shape C and B with amplitudes δ were installed in the airfoil and tested. F^+=1.5 was not tested for cam C. This was because the frequency could be multiplied only by a factor of two for the same shaft rotational speed, which was limited due to the capability of the driving motor.

Cam shape C also increased $c_{l,max}$ by more or less the same amount as did cam shape A of the same amplitude at F^+=1, as shown in Figure 4-23,. However, the increase is smaller for F^+=0.5. Again drag trend is the same as for cam A which is to say that drag is higher at lower angles of attack but lower around stall as shown in Figure 4-24.

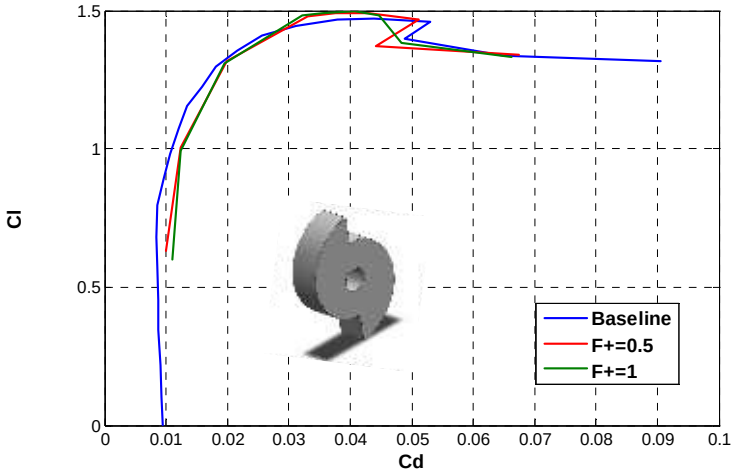

Figure 4-24 Comparison of baseline drag with cam shape C, R_C=1,000,000

Cam shape B, which was tested at F^+=1, did not do better than the other two cam shapes and hence the results are not discussed.

These results show that dynamic roughness does affect the flow characteristics but the gains are not very promising from the point of view of practical application. Tests performed on the SM701 airfoil by Yang et al. [38] relied on tufts to visualize stall delay. The testing looked very promising based on the observed flow attachment, and the increase in virtual stall angle of attack was estimated to be as much as 20%. Lack of resources did not permit detailed measurement of aerodynamic forces in that experiment. Since the investigation was performed at a low Reynolds number, i.e. R_C=120,000, it was thought possible that the gains might be higher if the current experiments were conducted at around a similar Reynolds number range. Due to the limitation imposed by the size of the model, the lowest Reynolds number that could be reasonably tested was 250,000. The following paragraphs discuss the results at low Reynolds number using cam C.

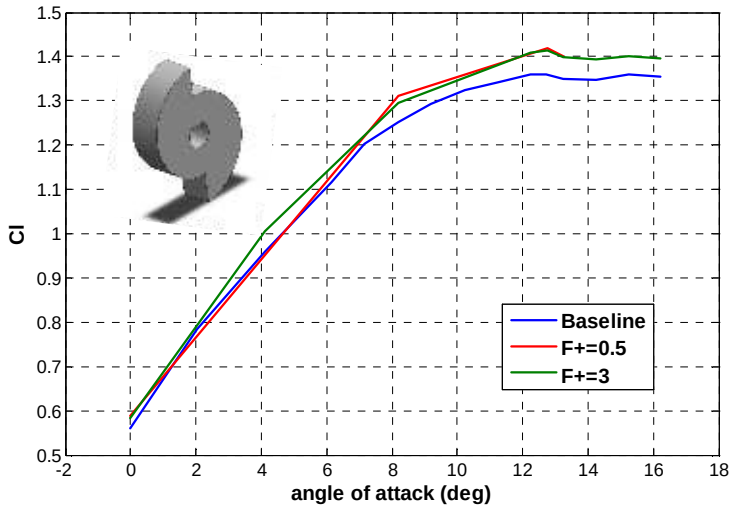

Figure 4-25 Comparison of baseline lift with cam shape C at R_C=250,000

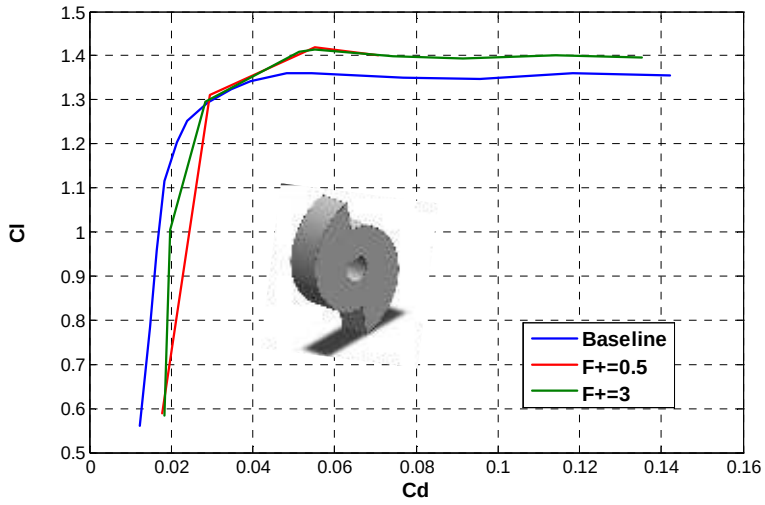

Figure 4-26 Comparison of baseline drag polar with cam shape C at R_C =250,000

$c_{l,max}$ at both F^+=3 and F^+=0.5 are about 4.5 % higher than the baseline. Interestingly, the gain in maximum lift seems to be independent of the frequency of excitation. Lift curves at stall are flattened out and do not drop until about 17 degrees. Drag increased at lower angles of attack and decreased at higher angles of attack around the stall region, as shown in Figure 4-26.

The experiments discussed thus far were conducted with free transition, which is to say that the laminar boundary layer was not artificially tripped but allowed to develop and transition naturally due to inherent instability of the laminar boundary layer. The tests with cam A were repeated with a transition strip placed at 5% chord, as shown in Figure 4-27. The test recorded baseline $c_{l,max}$=1.40, 4.28% less than the free transition case. Actuation at F^+=1.5, the best frequency of excitation among the three frequencies tested at high Reynolds number, did not increase $c_{l,max}$ more than it did in free transition case.

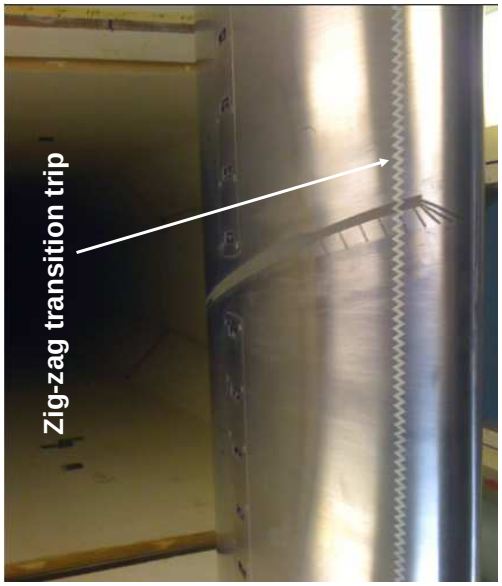

Figure 4-27 Forced transition test with cam A at R_C =1,000,000

4.2.5 Comparison of Dynamic Roughness with Static Vortex Generators

For the test performed here, dynamic roughness, based on the actuation mechanism involving rotating cams, does affect the characteristics of the boundary layer on the airfoil but provides net gains in c_l not significant for practical applications. Forcing leading edge transition did not result in positive improvement in performance due to dynamic roughness.

Observation of lift curves and drag polars with dynamic roughness actuation suggests that they seem to work like the traditional static vortex generators with superimposed dynamic motion. To determine how dynamic roughness compared with static vortex generators, counter-rotating static vortex generators, 5 mm tall, were

installed at 10% and 48% chord from the leading edge as shown in Figure 4-28. 48% corresponds to the chord wise location of the dynamic roughness. It was observed that the static vortex generators at 10 % chord increased $c_{l,max}$ by 35% and α_{stall} by 4 degrees at R_C =1,000,000 due to the resulting mixing and energization of the boundary layer. Drag was significantly reduced at stall due to the delay of boundary layer separation as shown in Figure 4-30. Nose up pitching moment is also reduced due to the vortex generators. The vortex generators at 48% chord increased $c_{l,max}$ by 14% but did not increase α_{stall}.

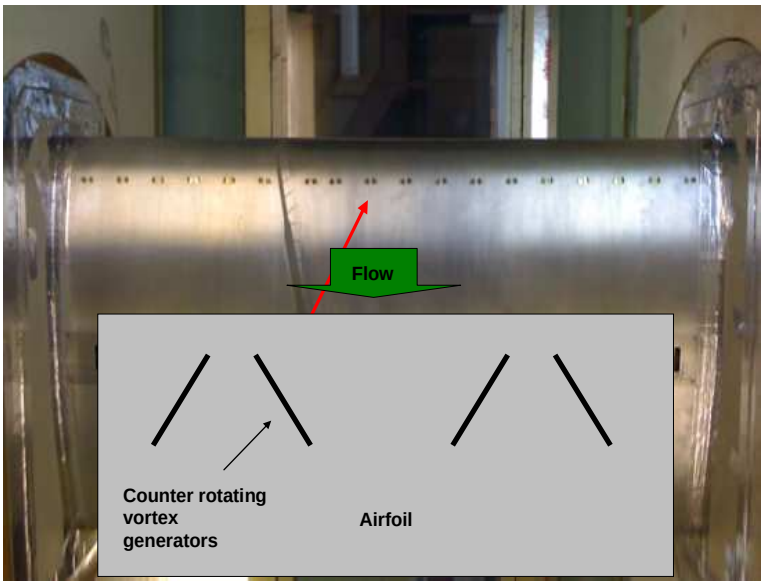

Figure 4-28 Vortex generators installed at 10% chord from leading edge

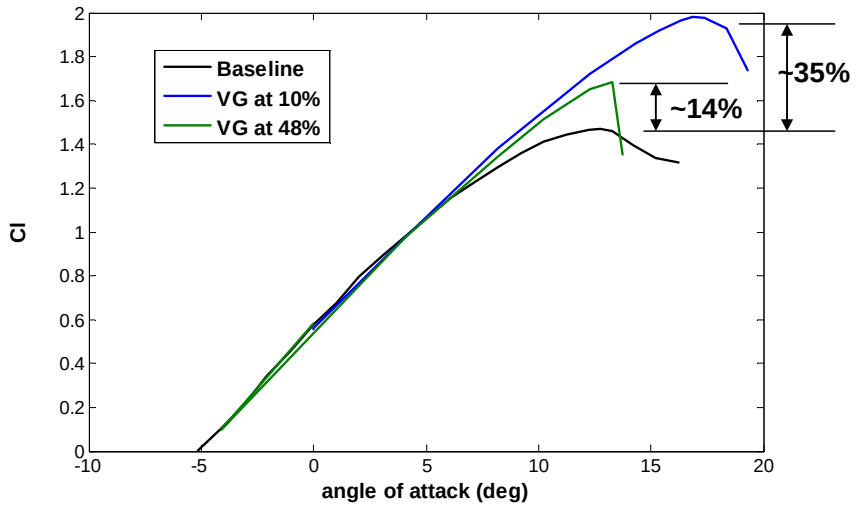

Figure 4-29 Effect of static vortex generators on baseline lift coefficients

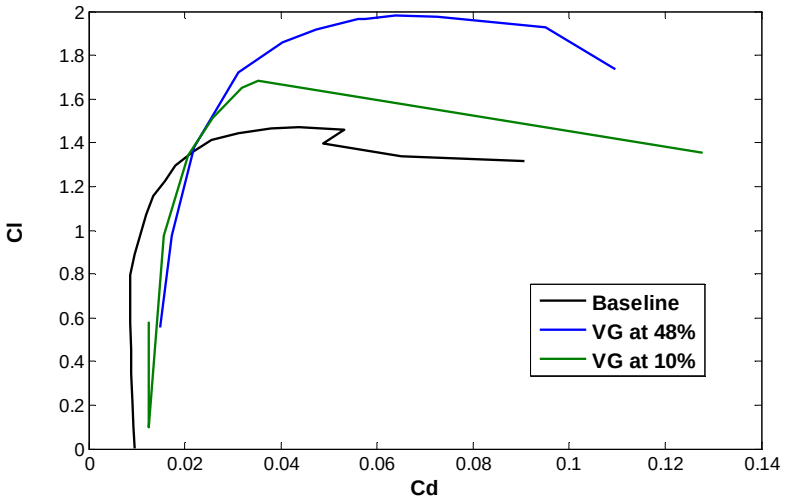

Figure 4-30 Effect of static vortex generators on baseline drag polars

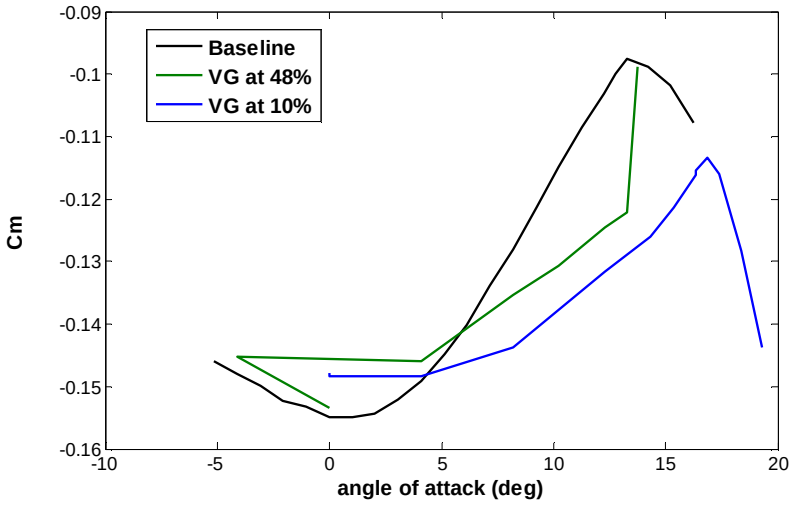

Figure 4-31 Effect of static vortex generators on baseline moment coefficients

A question was raised as to whether the observations made by Yang et al. [38] on The SM 701 airfoil with dynamic roughness actuation were reliable. The results from the HTR1555 tests pointed to the need to repeat the experiments on the SM701 airfoil. The indication of stall in that test was based only on the behavior of the tufts. Tufts were attached to the area around the actuators. When these tufts are behaved, the airfoil was considered to be un-stalled. In general, although the tufts are behaved at a particular angle of attack, actual force measurement may show that the airfoil is past $c_{l,max}$ point and hence in the post-stall regime. In order to verify that the observed effects on the SM701 airfoil were indeed due to flow modification caused by the physical dynamic roughness and that dynamic roughness can be a potentially effective flow control method, it was decided to go back and not only repeat the original three dimensional experiments on the SM701 airfoil but also modify it to investigate the two-dimensional flow characteristics

due to dynamic roughness excitation. Section 4.3 will discuss the observations from this experiment.

4.3 The SM 701 Airfoil

The investigation into the effectiveness of dynamic roughness as a flow control method, as reported in this thesis, was motivated by a numerical work performed by the Honsaker and Huebsch [40], and an experiment conducted by Yang et al. [38]. The work by the former focused on the flow modification in the leading edge of an airfoil shape but did not perform any detailed quantitative analysis on the aerodynamic performance of the airfoil as a whole. The motivation for this work derived largely from the latter, where a claim was made that dynamic roughness applied close to and upstream of the separation point corresponding to baseline stall of SM701 airfoil caused delay in virtual stall, as observed from the behavior of the surface tufts attached around the location of the actuators.

Since no promising results were observed from the testing of dynamic roughness applied on two different airfoils, the NACA 23012 and the HTR 1555 discussed earlier, the following hypotheses were proposed:

1. Since the character of motion of dynamic roughness in the experiments on the NACA23012 and the HTR1555 airfoils are different from that of the SM701 airfoil experiment conducted by Yang et al. [38], the inability of dynamic

roughness in enhancing aerodynamic performance on the former could be due to the difference in actuation mechanism;

2. The flow attachment observed in the experiment conducted by Yang et al. [38] could be due to the effect of something other than the physical dynamic roughness.

The following sections will discuss the observations from the experiments performed on the SM701 airfoil with the original peizo-bender actuators. All experiments were performed at R_C=125,000.

4.3.1 Three-Dimensional Experiment

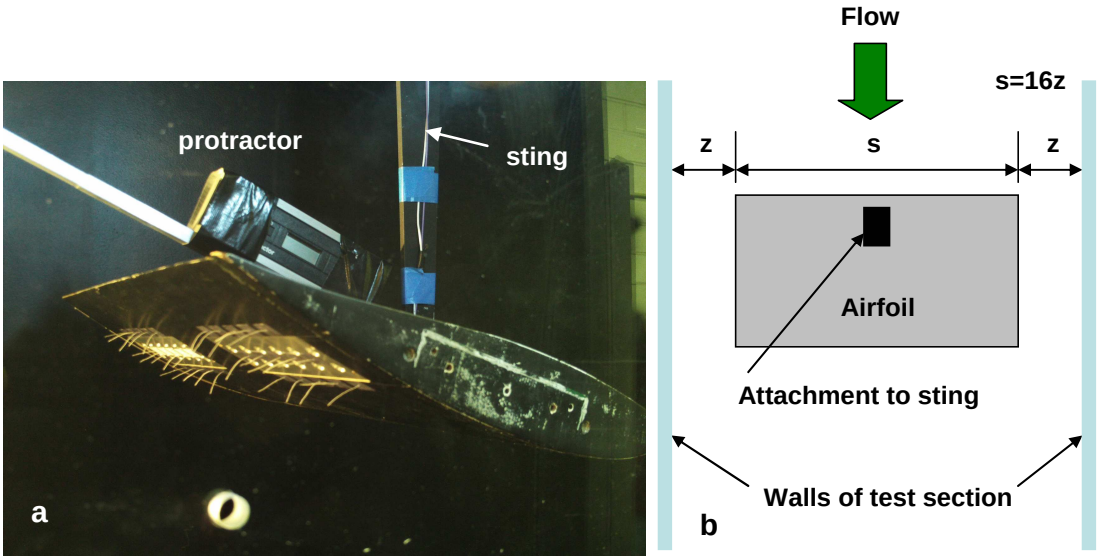

Figure 4-32 a) The original set up of three-dimensional model on sting, b) Top view of the experimental set-up

The experimental set up of Yang et al. [38], as shown in Figure 4-32(a), was replicated. The top view of the set up is shown in Figure 4-32(b). The gap z is 16% of the span, s, of the three-dimensional model. No aerodynamic measurements were made in this experiment. Only tufts were used to visualize the flow over the airfoil. Exact determination of stall in this configuration was hence not possible. The term "virtual stall", defined in section 1.2, was used as a qualitative measure of the effect of actuation for the purpose of comparison.

All angles of attack mentioned in this section are geometric angles of attack and measured from the chord line of the airfoil. In baseline configuration, the angle of attack was increased slowly with the dynamic roughness actuator turned off. The baseline virtual stall angle of attack was observed to be 17.7 degrees. When the actuator was turned on and excited at its resonance frequency, which ranged between 28Hz and 30 Hz due to the change in orientation as the airfoil was tilted, delay in virtual stall was observed only when a clearly audible noise was heard. The source of this noise was traced to be the dynamic roughness pins contacting the side of the pin holes in the cover plates as shown in Figure 4-33. When the frequency of actuation was adjusted so that this noise was eliminated, no delay in virtual stall was observed. The observations are summarized in Table 10. Re-attachment angles, defined as the angle at which the tufts reattach on decreasing the angle of attack from post stall, are also shown.

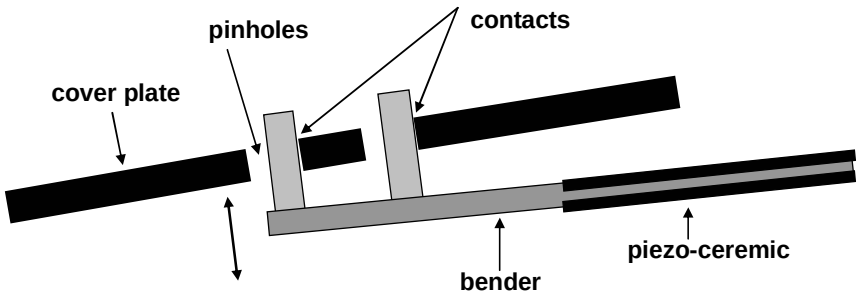

Figure 4-33 schematic showing the side view of the contact point

	Baseline	Actuator on (Noise)	Actuator on (No Noise)
	f=0Hz,h=0mm	f=28Hz, h=6mm	f=30Hz, h=5mm
Virtual stall angle	17.7	22.1	17.8
Reattachment angle	13	15.2	13

Table 10: Three dimensional observations at R_C=125,000

When the input voltage supply was set such that the actuator generated the noise, it increased the virtual stall angle of attack from 17.1 degrees at baseline to 22.1 degrees, a delay of 4.4 degrees. The reattachment angle also increased from 13 degrees at baseline to 15.2, an increase of 2.2 degrees. On eliminating the noise by adjusting the voltage supply, virtual stall angle was measured to be 17.8 degrees, unchanged from the baseline case. Moreover, reattachment angle remained unchanged with respect to baseline. In adjusting the frequency and voltage input to the actuator to create the noise, the actual amplitude of excitation of the pins from the airfoil surface was maintained within an error of ±1mm.

4.3.2 Two-Dimensional Experiment

In order to make sure that the phenomenon discussed in section 4.3.1 is somehow not due to the three dimensionality of the experiment and that it could still be observed in two-dimensional case, sections were attached to both sides of the three-dimensional model to make it span the width of the test section, as shown in Figure 4-34.

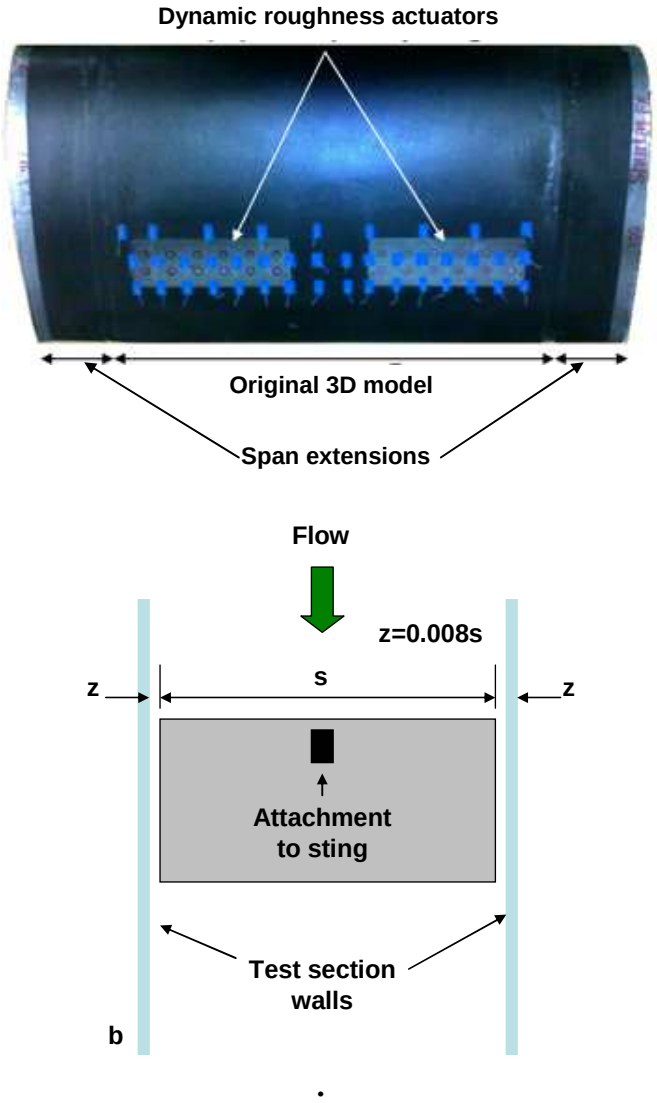

Figure 4-34 a) Modified airfoil for two dimensional test, b) Top view of the experimental set up

The same experimental procedure followed for the three-dimensional test was repeated for the two-dimensional testing of the modified airfoil. The observations are summarized in Table 11.

	Baseline	Actuator on (Noise)	Actuator on (No Noise)
	f=0Hz, h=0mm	f=28Hz, h=6mm	f=28Hz, h=5mm
Virtual stall angle	18.8	19.9	18.7
Reattachment angle	12.3	12.9	11.9

Table 11: Two-dimenisonal observations at R_C=125,000

Again, flow attachment was observed only when the noise was present. The baseline virtual stall angle increased from 17.7 to 18.8 degrees. The reattachment angle decreased slightly. The acoustic noise delayed the virtual stall angle by 1 degree, three degrees less than in 3D case. Reattachment angle was increased by only 0.6 degrees. When the noise was eliminated, virtual stall and reattachment angles remained essentially unchanged.

This experiment showed that two dimensionality of the model did not essentially change the phenomenon observed in the three-dimensional case, although the baseline virtual stall and reattachment angles changed. This further reinforced the acoustic excitation hypothesis proposed in section 4.3.1. Section 4.3.3 will discuss an experiment that reinforces this hypothesis.

Before discussing that, the two-dimensional airfoil model was mounted on the force balance and the lift coefficients were measured to not only identify the exact stall of

baseline airfoil, but also to see if the observed flow attachment, observed in the Yang et al. [38] experiment and replicated in this work, actually delayed stall or increased the maximum lift of the airfoil. The experimental set up is shown in Figure 4-35.

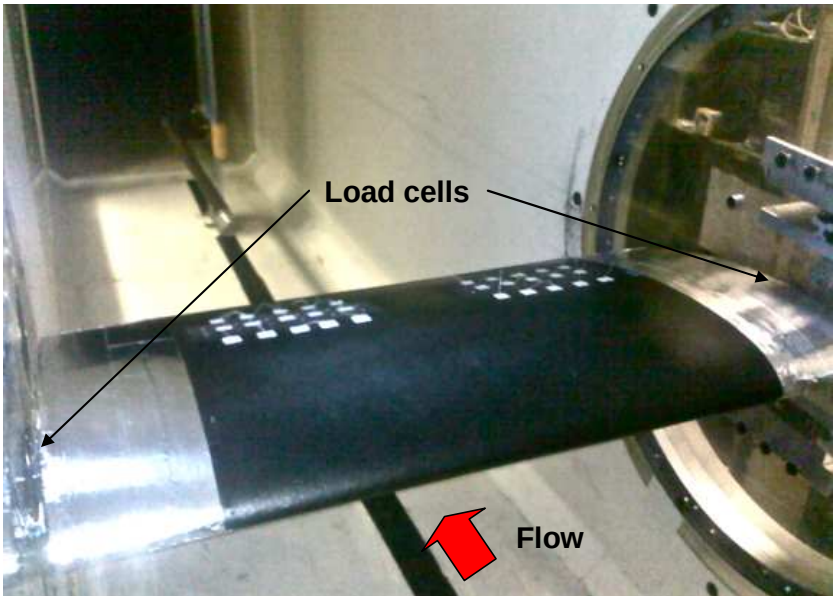

Figure 4-35 Set-up for SM701 two-dimensional Experiment

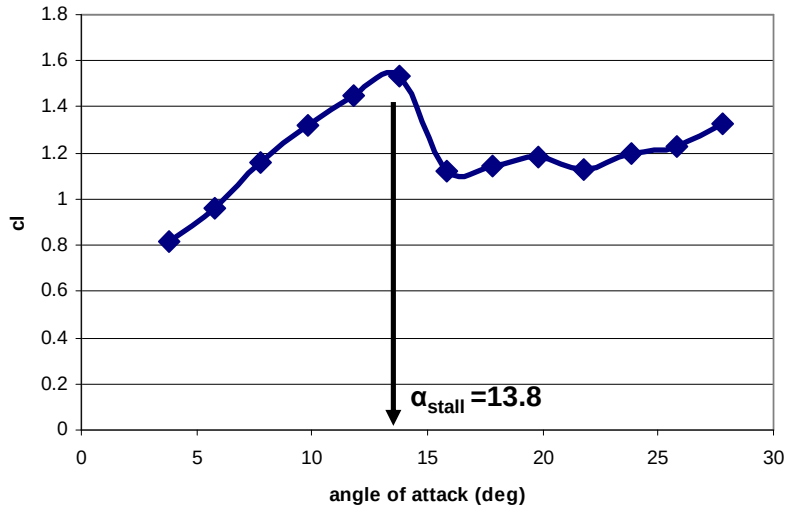

Figure 4-36 Baseline lift curve at R_C=125,000

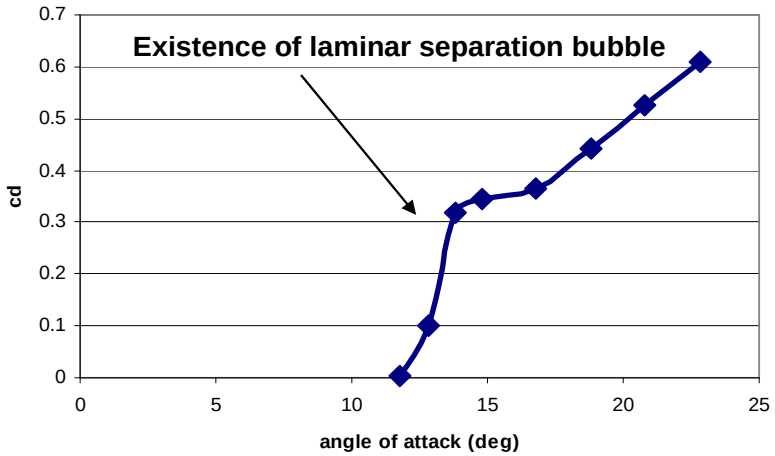

Figure 4-37 Baseline drag polar at R_C=125,000

It can be observe in Figure 4-36 that baseline stall occurs at 13.8 degrees. This is the actual stall angle, as opposed to virtual stall which was defined in section 1.2 and used as a measure of the effect of actuation when only tufts were used for observation. This tells us the following about the experiments performed on the SM701 airfoil with dynamic roughness:

1. The baseline virtual stall angle of attack shown in Table 11 is actually a post stall angle of attack.
2. Actuation did not increase the maximum lift, but merely affected certain post stall behavior.
3. Since maximum lift is unchanged, this has little use for practical airfoil performance improvement.

4.3.3 Verification of Hypothesis

Based on the observations discussed in the last few sections the hypothesis that the flow attachment, as indicated by the tufts, was caused by the acoustic noise generated when the pins of the dynamic roughness hit the side of the holes in the cover plate. If this noise was responsible for the observed phenomenon, then it should in principle be possible to replicate a similar the tuft behavior, without the peizo-actuation, when the same noise is recorded and re broadcasted on to the airfoil through a speaker. The set-up for recording the noise is shown in Figure 4-38. A microphone, connected to a computer, was held close to the actuator. With the wind off, the actuator was set in the noise-mode when the acoustic noise could be heard. This noise was recorded in the computer. This recorded noise was then played through a speaker placed close to the airfoil and its effect on the behavior of the tufts was observed carefully. The speaker was placed in two different positions, as shown in Figure 4-39

Figure 4-38 Set-up for recording the acoustic noise

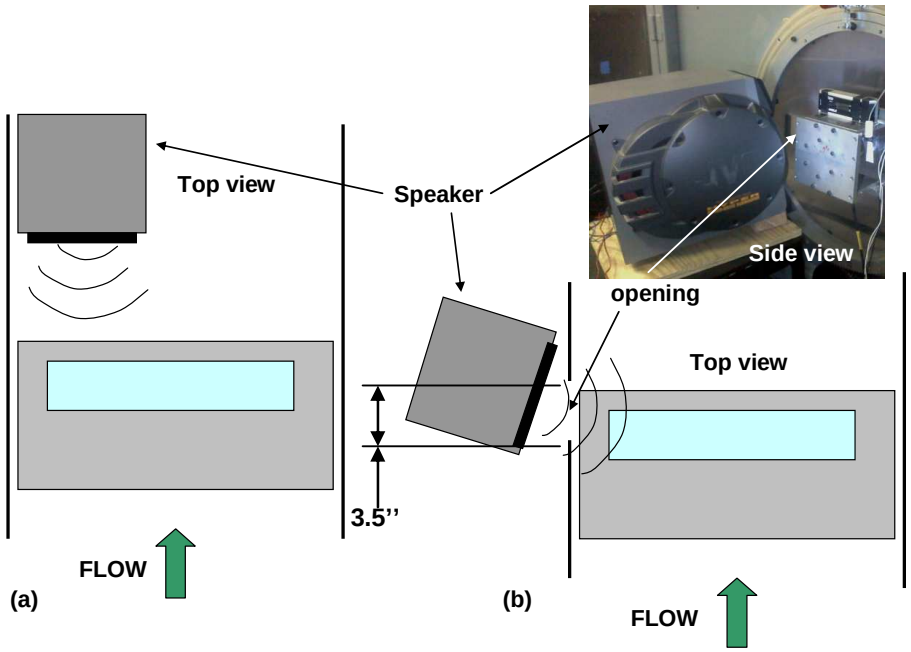

Figure 4-39 Two configurations of acoustic excitation

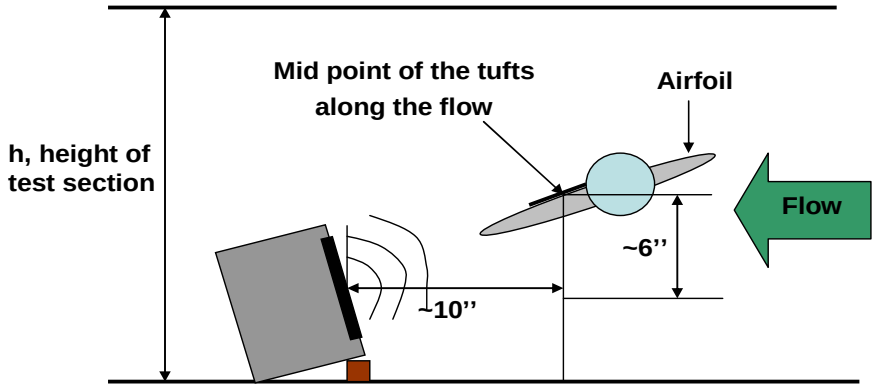

Figure 4-40: Side view of configuration (a) with distances of speaker with respect to the airfoil

The baseline virtual stall angles of attack have changed in these configurations due to the presence of the speaker box at the back of the airfoil shown in Figure 4-39(a) and the presence of a 3.5 inches by 2 inches opening close to the trailing edge of the airfoil shown in Figure 4-39(b), which is for the sound to reach the airfoil. The effect of acoustic excitation could still be compared with the changed baseline. Table 12 and Table 13 summarize the observations from these two tests. The baseline virtual stall angles are different from the ones reported in Yang et al. [38] because the airfoil does not span the test section in their experiments.

	Virtual stall angles			
	1	2	3	4
Baseline	12.2	12.3	12.5	12.3
Acoustics	13.6	13.6	13.6	13.6

Table 12: Observations for configuration (a)

	Virtual stall angles			
	1	2	3	4
Baseline	14.3	13.9	14	14
Acoustic excitation	14.9	14.5	14.9	14.9

Table 13: Observations for configuration (b)

The measurements were repeated four times in each configuration to rule out potential uncertainties. Observe that in configuration (a), the noise from the speaker

delayed virtual stall by about 1.5 degrees and in configuration (b), it was delayed by about 1 degree. Note that the actuators were not turned on. Only the sound from the speaker resulted in the observed behavior of the tufts. Hence, it seems that the flow attachment observed in the work of Yang et al. [38] was not due to the dynamic roughness, but due to the resulting acoustic noise.

The recorded noise was analyzed through a spectrum analyzer for the frequency and amplitude contents and plotted in Figure 4-41. Noise recorded in configuration A had a frequency of 160 Hz and amplitude of 78.54 dB. Configuration B recorded 160Hz and 79.92 dB.

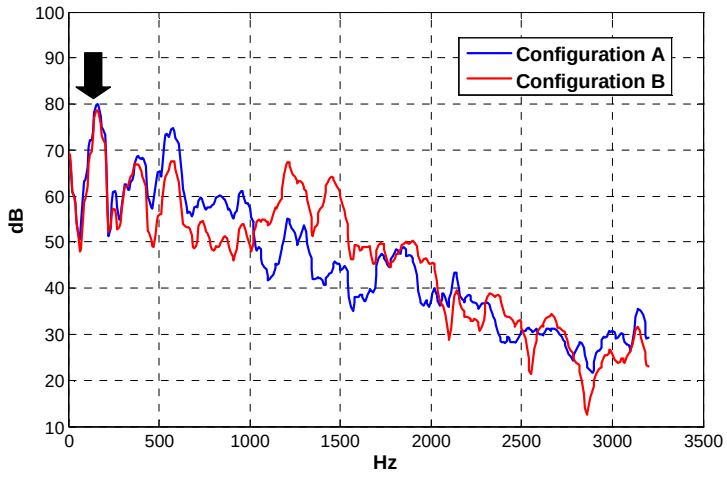

Figure 4-41: Frequencies and amplitudes of the recorded acoustic noise

Further evidence that substantiates this hypothesis is this. One of the actuators in the experiments by Yang et al. [38] was not working when the reported observations was made. Nevertheless, excitation of the remaining actuator caused the tufts attached around

both the actuators to behave. Acoustic noise which propagates in all directions can cause this seemingly transition forcing mechanism resulting in the observed behavior of the tufts. Localized actuation can be expected to mostly affect only flow around its vicinity and downstream.

The observations, as discussed in this section, call into question the argument in favor of dynamic roughness as a potentially effective flow control method, as the work by Yang et al. [38] was the motivation of the current investigation. Nevertheless, dynamic roughness in the form of rotating cam mechanism as applied to the HTR1555 airfoil, did affect the boundary layer characteristics, albeit with the gain in aerodynamic performance not promising for practical airfoil application.

Vibration of the Airfoil

The vibration levels of the airfoil model with and without noise were measured by an accelerometer and plotted in Figure 4-42. It should be observed that the vibration level of the airfoil with the noise is about 3 to 4 times as much as the one without the noise. Could this also have contributed to the observed flow attachment in the experiment by Yang et al. [38]? At this point, it is yet to be verified. It is known, however, that acoustic excitation at the right frequency and amplitude can cause flow attachment as discussed in the literature review.

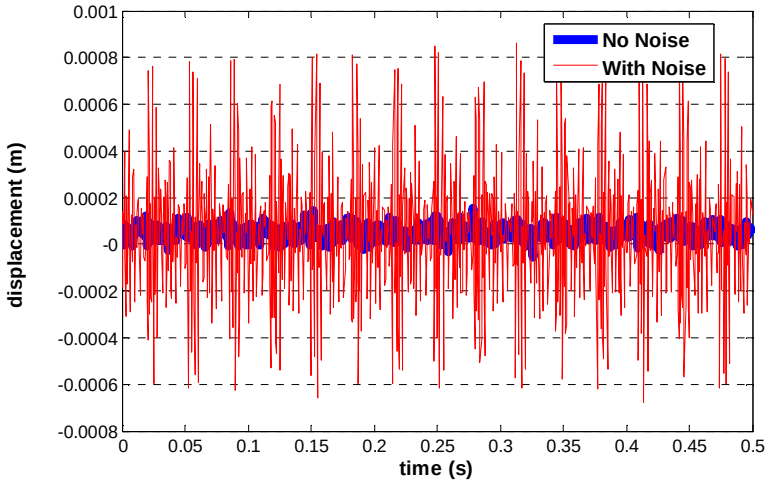

Figure 4-42: Vibration levels between "with noise" and "no noise" cases as measure by accelerometer

Chapter 5

CONCLUSIONS

The goal of this research was to experimentally investigate dynamic roughness as a potential aerodynamic flow control method. The objectives included design of a dynamic roughness actuator that met the actuation requirements at higher Reynolds numbers, implementation of the designed actuator on airfoils in order to measure the aerodynamic effects of dynamic roughness. Also, a force balance mechanism for a two dimensional airfoil testing was required to be designed for Hammond Low-Speed wind tunnel at Penn State which was proposed to be used for this research.

As proposed, a force balance mechanism was designed for the subsonic wind tunnel which now has two capabilities. One, it can measure the aerodynamic forces and moments on an airfoil or any model that can fit in the test section. Two, it allows for automatic adjustment of angle of attack of the model from a computer.

A mechanism involving mechanical spring was proposed for dynamic roughness actuation. Kinematic and dynamic analyses performed on a simplified model of the mechanism led to the conclusion that the proposed actuation mechanism could not function properly at the frequencies of excitation that were required at higher Reynolds numbers. A rotating cam mechanism that involves no mechanical springs was designed as an alternative actuation mechanism.

Application of dynamic roughness close to the separation point at stall on the NACA23012 airfoil failed to provide any aerodynamic gain. This was hypothesized to be due to the stalling characteristics specific to the NACA23012. As a result, the HTR1555, a rotorcraft airfoil, was used for the testing of dynamic roughness. Detailed wind-tunnel testing of this airfoil with dynamic roughness resulted in the following conclusions:

1. There is no straightforward rule that can be followed as far as choosing the right location of actuation on an airfoil is concerned. The ideal location of excitation changes from airfoil to airfoil.
2. In the HTR1555 experiment, maximum gain in $c_{l,max}$ due to the actuation of dynamic roughness with the amplitude of excitation on the order of local boundary layer thickness at R_C=1,000,000 was 3.5%
3. The higher the amplitude of excitation, the larger the gain in $c_{l,max}$.
4. The higher the frequency of actuation, for the non-dimensional F^+s tested in this work, the higher is the gain in maximum lift generated by the airfoil.
5. The shapes of the dynamic roughness tested in this work had little effect on the outcome in terms of aerodynamic performance enhancement.
6. The gain in $c_{l,max}$ is higher at lower Reynolds number.
7. A similar documented experiment to dynamic roughness is the work by Park, Lee, Lee, Srungkie [32]. Comparison with that experiment shows that, like in this work, the gain in $c_{l,max}$ is minimal, although the stall angle was delayed by one about degree.

8. It seems that those flow control methods which harness the higher momentum in the outer edge of the boundary layer, including oscillatory blowing and traditional static vortex generators, are more effective than a physical perturbation with an amplitude that is less than or on the order of the local boundary layer thickness, especially in the turbulent boundary layer, as was the case all of the experiments conducted in this work.

Such a minimal gain in aerodynamic performance seemed to contradict the observed behavior of the tufts on the SM701 airfoil with dynamic roughness in the experiments by Yang et al. [38] The SM701 experiments were repeated carefully to confirm the reported observations. Force measurements indicated that the tuft attachments observed in Yang et al.'s [38] experiment were in fact in the post stall flow regime. Further investigation revealed that the flow attachment was not due to the dynamic roughness itself but due most probably to the acoustic noise generated by the dynamic roughness pins contacting the side of the pin holes on the cover plates as it vibrated.

With regard to the field of active flow control, Seifert and Tilmann [45] remarks: …in many studies the expected results were not obtained…however, the practitioners in the field could learn a great deal from such expertly conducted studies that did not result in the hoped for outcome. With this in mind, the results from this work are compared with similar experiments conducted by past researchers and tabulated below for comparison and for future reference. The author believes that the work discussed in this thesis is a small contribution to the field of active flow control.

Investigator (s)	Airfoil	R_C (x 10^6)	F^+	Amplitude (mm)	Location, x/c (%)	$\Delta C_{l,max}$ (%)
Viets et al. [25]	An airfoil Shape with rounded trailing edge	0.1	0.4, 0.5	2.66 (rotating mechanical actuator)	19.5	Not measured
Park, Lee, Lee et al. [32]	NACA0012	0.2	1.94	1.3 (buzzing rod)	11	3.5
Tenzin et al.	HTR1555	1.0	1.5	6 (dynamic roughness rotating cams)	55	3.5
Tenzin et al.	HTR1555	0.25	3, 0.5	6 (dynamic roughness rotating cams)	55	4.5
Seifert et al. [28]	IAI P255	0.20	2	1 (Flaperon)	8	8.4

Table 14: Comparison of dynamic roughness with similar experiments

Chapter 6

RECOMMENDATIONS

It has been explained in this thesis that dynamic roughness does affect the flow as observed in the experiment on the HTR1555 airfoil with the actuation at the mid chord location. But its effect on the enhancement of maximum lift is minimal at higher Reynolds number. It seems that those flow control methods that harness the momentum from the outer boundary layer, such as oscillatory blowing and traditional static vortex generators, work better than those methods, including dynamic roughness, that employ physical perturbation with an amplitude that is less than or on the order of the local boundary layer thickness.

Implementation of vortex generators is not always desirable due to associated drag increment when it is not needed. This can be taken care of if the vortex generators are made deployable. Deployable vortex generators, for example, can be tuned to be actuated 1/rev and can provide higher lift on the re-treating blade on a helicopter, thereby enhancing rotor performance.

Schematics of the conceptual deployable vortex generators are shown in Figure 6-1 and Figure 6-2.

Using static vortex generators is an effective method in delaying stall in static airfoil aerodynamics. If its effectiveness in dynamic stall encountered in rotorcrafts is established, the problem then will be the optimization for timely deployment on in a rotor environment.

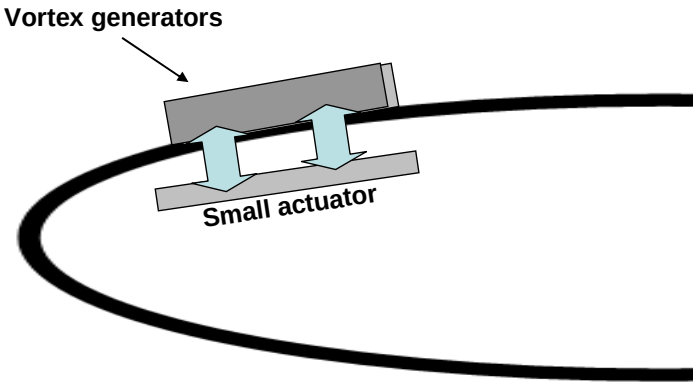

Figure 6-1 Proposed deployable vortex generators

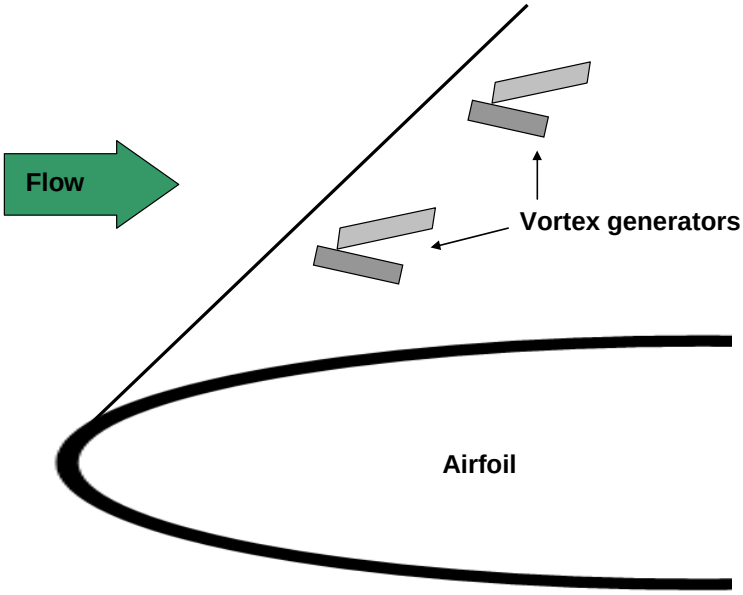

Figure 6-2 Three-dimensional view of the proposed deployable vortex generators

APPENDIX

Source: [42]

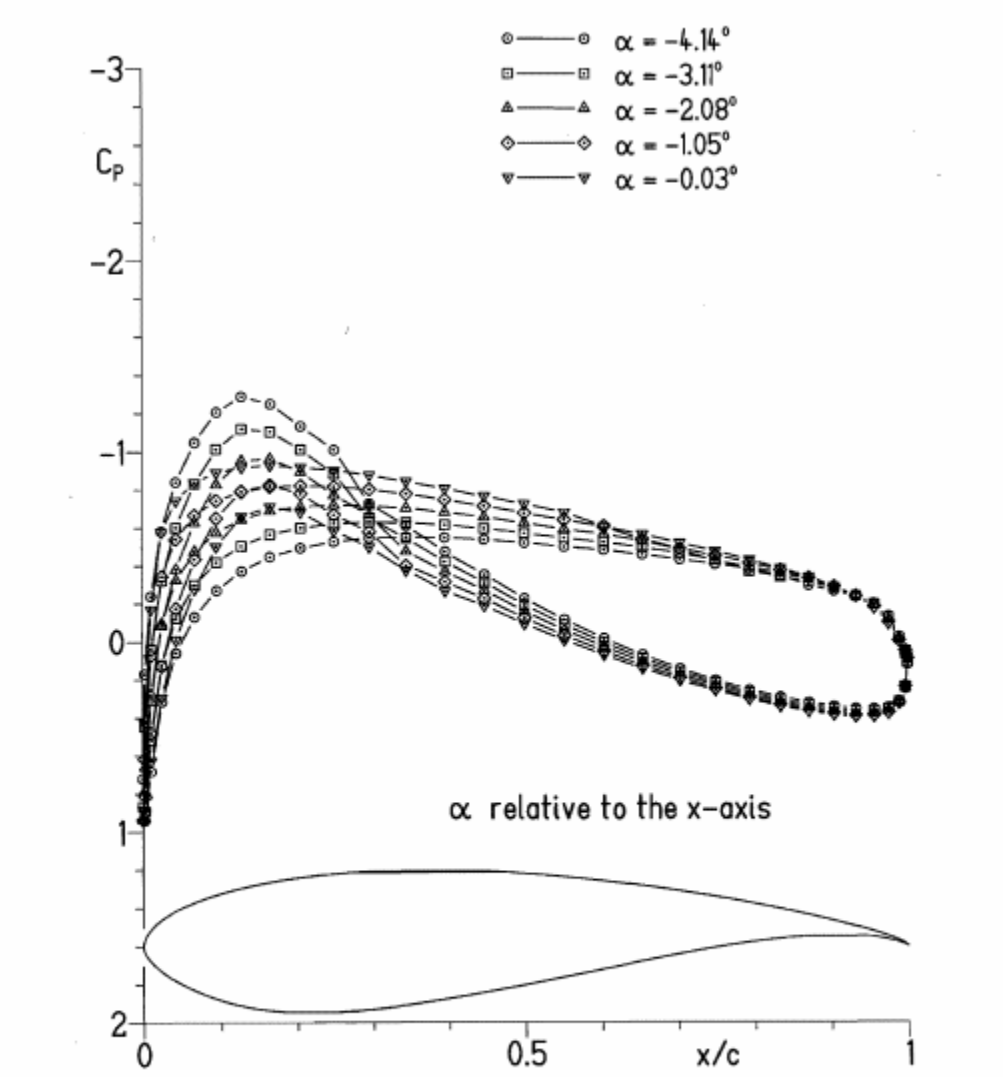

(b) α = −4.14°, −3.11°, −2.08°, −1.05°, and −0.03°.

Figure 5.- Continued.

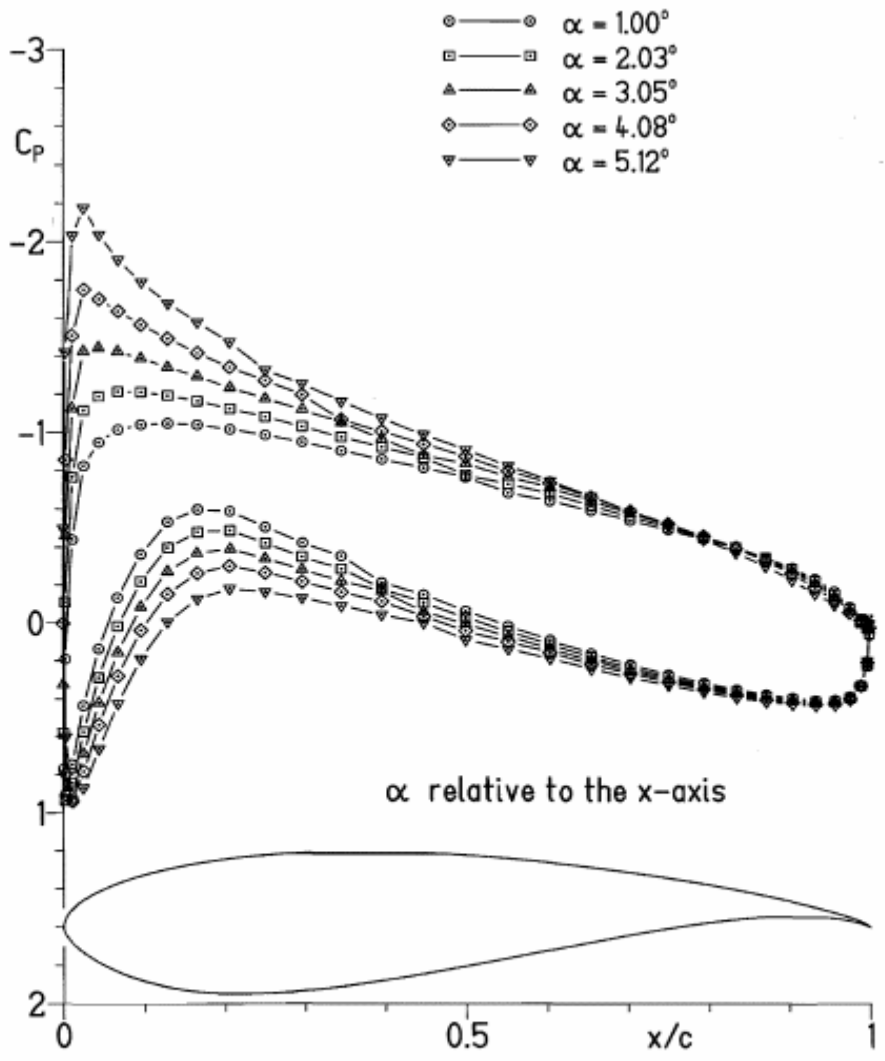

(c) $\alpha = 1.00°$, 2.03°, 3.05°, 4.08°, and 5.12°.

Figure 5.- Continued.

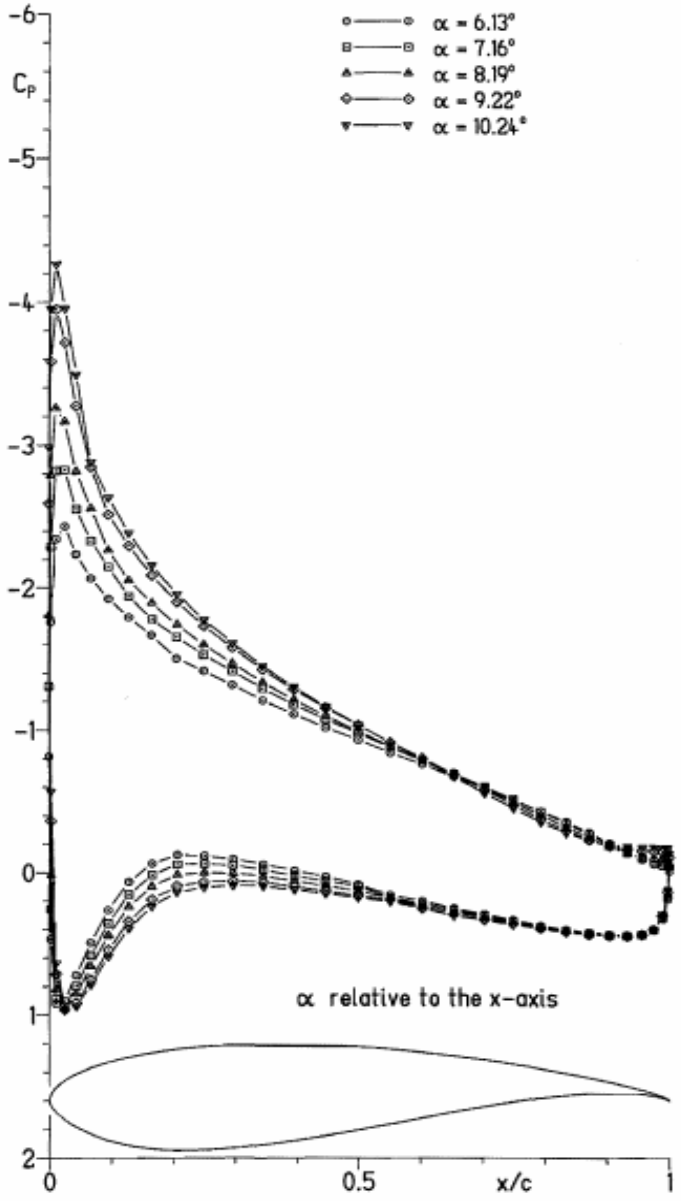

(d) $\alpha = 6.13°$, 7.16°, 8.19°, 9.22°, and 10.24°.

Figure 5.- Continued.

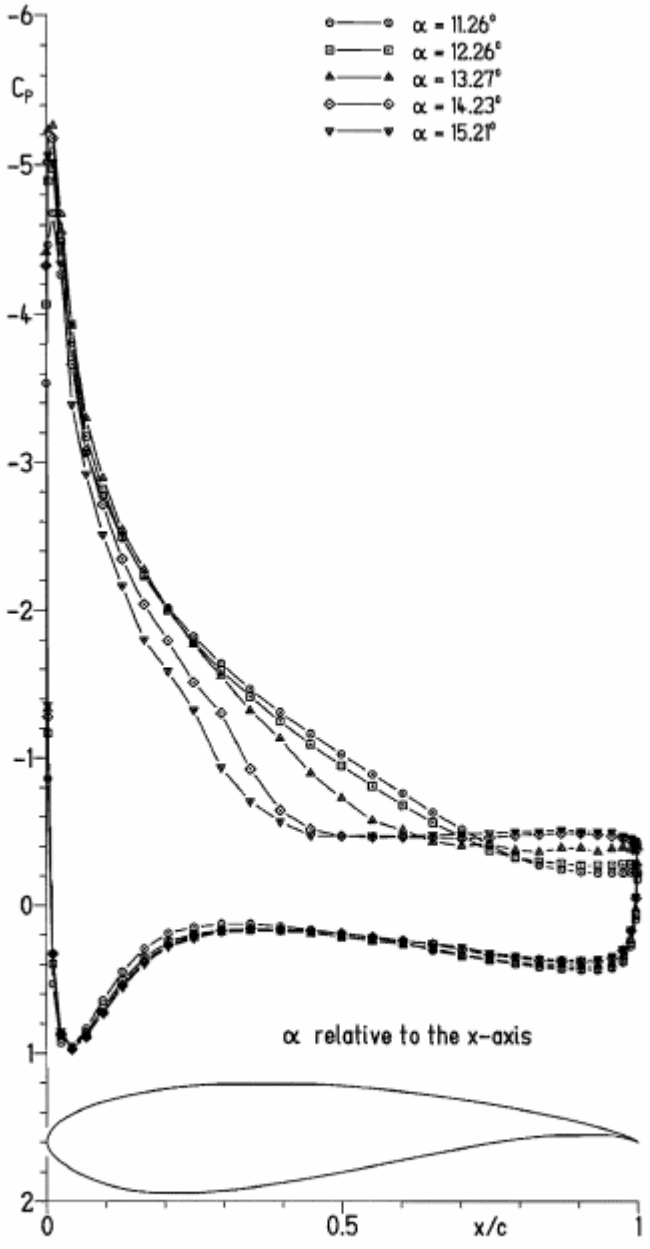

(e) $\alpha = 11.26°$, $12.26°$, $13.27°$, $14.23°$, and $15.21°$.

Figure 5.- Concluded.

REFERENCES

[1] Maskell E.C. Flow Separation in three dimensions. *RAE Report Aero* 2565, 1955

[2] Mohamed Gad-el-Hak. The art of flow control. Low speed airfoil aerodynamics, *Notes in Fluid Mechanics*, Springer.

[3] Hermann Schlichting, Klaus Gersten, Boundary layer Theory, Springer-Verlag Berlin Heidelberg, 2000.

[4] Schrenk, O. "Grenzcschichtabsaugung," *Luftwissen*, Vol. 7, p. 209, 1940

[5] Donald, D. The complete encyclopedia of world aircraft, Barnes and Noble, New York, 1997

[6] Liebeck, R.H. On the design of subsonic airfoils for high lift, *AIAA paper* 2006-3690

[7] Gad-el-Hak, M, Bushnell, D.M. Separation control: review. *Journal of Fluid Engineering* 1991;113:5-30

[8] Tietjens, O. "Beitrage zur enststehung der Turbulenz", Dissertation, Gottingen, Germany, 1922

[9] Tollmien, W. "Uber die Entstehung der Turbulenz, 1. Mitteilung", *Nachr. Acad. Wiss., Gottingen, Math. Phys*.,pp. 21-44

[10] Schubauer, G.B, Skramstad, H.K. Laminar boundary layer oscillations and transition on a flat plate. *NACA Report* 909,1048

[11] Mangiarotty RA. Control of Laminar flow in fluids by means of acoustic energy. *US Patent* -4,802,642, 1989.

[12] Kim, H.T., Kline, S.J., and Reynolds, W.C. The production of turbulence near a smooth wall in a turbulent boundary layer", *Journal of Fluid Mechanics*, vol. 50, pp. 133-166

[13] Brown, G.L, Roschko, A. On density effects and large structure in turbulent mixing layer. *Journal of Fluid Mechanics*, 1974; 64: 775-816

[14] Winant, C.D, Brownand, F.K. Vortex pairing: the mechanism of turbulent mixing layer growth at moderate Reynolds number. Journal of Fluid Mechanics, Part 2 1974; 63:237-56

[15] Ho, C.M, Huang, L.S. Subharmonics and vortex merging in mixing layes, *Journal of Fluid Mechanics* 1982; 119:119-42

[16] Ronald, D. J., Daniel, N.M (ed.). Fundamentals and applications of modern flow control, *Progress in Aeronautics and Astronautics*, Vol. 231, *AIAA publication*, 2009.

[17] Greenblatt, D., Wygnansky, I.J., The control of flow separation by periodic excitation, *Progress in Aerospace Sciences*, Vol. 36, No. 7, pp 487-545

[18] Ahuja, K.K, Whipkey, R.R., Jones, G.S., Control of turbulent boundary layer flow by sound, *AIAA Paper* 83-0726, 1983.

[19] Zaman, K.B.M.Q, Bar-Sever, A, Mangalam, S.M., Effect of acoustic excitation on the flow over a low-Re airfoil. *Journal of Fluid Mechanics*, 1987; 182:127-48

[20] Zaman, K.B.M.Q, McKinzie, D.J, Rumsey, C.L. A natural low-frequency oscillation of flow over an airfoil near stalling conditions. *Journal of Fluid Mechanics*, 1989; 202; 403-42

[21] Collins, F.G., Zelenevitz, J. Influence of sound upon separated flow over wings, *AIAA journal*, 1975; 13(3):408-10

[22] Zaman, K.B.M.Q. Effect of acoustic excitation on stalled flows over an airfoil. *AIAA Journal*, 1992;30(6)

[23] Nishri, B. On the dominant mechanisms governing active control of separation. *PhD thesis*, Tel Aviv University, 1985.

[24] (81) Nishri, B., Wygnansky, I.J., Effects of periodic excitation on turbulent separation from a flap. *AIAA Journal*, 1998; 36(4)"547-56.

[25] Hermann Viets, Michael Piatt and Mont Ball, Unsteady wing boundary layer energization, *AIAA paper* 79-1631, 1979

[26] Neuberger D, Wygnansky I., The use of vibrating ribbon to delay separation on two-dimensional airfoils: some preliminary observations. *Workshop on Unsteady Separated Flow*, Air Force Academy, July 1987.

[27] Bar-Sever A., Separation control on an airfoil by periodic forcing. *AIAA Journal* 1989; 27 (6):820-1.

[28] Seifert A, Bachar T, Koss T, Shepshelovich M, Wygnansky I., Oscillatory blowing, a tool to delay boundary layer separation. *AIAA Journal* 1993;31(11)

[29] Seifert A, Darabi A, Wygnansky I., Delay of airfoil stall by periodic excitation. *AIAA Journal of Aircraft* 1996;33(4)

[30] Seifert A, Eliahu S, Greenblatt D, Wygnansky I., Use of peizo-electric actuators for airfoil separation control. *AIAA Journal* 1998;36(8)

[31] Sang Hoon Kim and Chongam Kim, Separation Control on NACA23012 using synthetic jet, AIAA 2006-2853, 3rd *AIAA Flow Control Conference*, 5-8 June 2006, San Francisco, California.

[32] Youngwhe Park, Soogab Lee, Dongho Lee, Byongho Ahn, Seungkie Hong., Stall control by local surface movement on an airfoil, AIAA 2001-0254, *39th Aerospace Science Meeting and Exhibit, Jan 2001*, Reno, Nevada

[33] Smith B.L., Glezer A., Vectoring of High aspect ration air jet using zero-net-mass-flux control jet, *Bulletin of the American Physical Society*, 39:1994

[34] A.C. Miller, Flow control via synthetic jet actuation, *MS thesis*, Texas A & M University, 2004

[35] Brett James Warta, Characterization of high momentum flux Combustion powered fluidic actuators for high speed flow control, *MS thesis*, Georgia Institute of Technology, 2007.

[36] James W. Gregory, C.Lon Enloe, Gabriel I. Font, Thomas E. McLaughlin, Force production mechanism of a dielectric-barrier discharge plasma actuator, *45th AIAA Aerospace Sciences Meeting and Exhibit*, 8-11 January 2007, Reno, Nevada.

[37] Nagib, Kiedaish, Wygnansky, Stalker, Wood, McVeigh, First-in-flight full-scale application of active flow control: The XV-15 tiltrotor download reduction, *RTO-MP-AVT-111*

[38] Timothy P. Yang, Jose Palacios, Boundary layer separation control via dynamic roughness elements, *Next generation vertical lift technologies-Active technology*, Dallas, Texas, October 15 2008.

[39] Wade. W. Huebsch, Dynamic surface roughness for aerodynamic flow control, *42nd AIAA Aerospace Sciences Meeting and Exhibit*, 5-8 January, 2004, reno, Nevada.

[40] R. Honsaker, Wade W. Huebsch, Parametric study of dynamic surface roughness as a mechanism for flow control, *23rd Applied Aerodynamics Conference*, 6-9 June 2005, Toronto, Ontario, Canada.

[41] J.G. Leishman, Dynamic stall experiments on the NACA23012 airfoil, *Experiments in fluids* 9, 49-58 (1990).

[42] Martin, P., Rhee, M., Maughmer, M., and Somers, D., Airfoil Design and Testing for High-Lift Rotorcraft Applications, *AHS Specialists Conference on Aeromechanics*, San Francisco, CA, Jan. 23-25, 2008.

[43] Jacot D, Mabe J. Boeing active flow control system. *AIAA paper* 2000-2473, *Fluids* 2000, Denver CO, June 19-22, 2000

[44] Jewel B. Barlow, William H. Rae, Jr., Alan Pope, Low-speed wind tunnel testing (third edition), John Wiley & Sons, 1999.

[45] Seifert, A., Tillmann, C.P., Fixed wing airfoil applications, Fundamentals and applications of modern flow control, 2008, *Progress in Astronautics and Aeronautics,* Vol. 231, AIAA publication.